

# REPORT DOCUMENTATION PAGE

Form Approved  
OMB No. 0704-0188

The public reporting burden for this collection of information is estimated to average 1 hour per response, including the time for reviewing instructions, searching existing data sources, gathering and maintaining the data needed, and completing and reviewing the collection of information. Send comments regarding this burden estimate or any other aspect of this collection of information, including suggestions for reducing the burden, to Department of Defense, Washington Headquarters Services, Directorate for Information Operations and Reports (0704-0188), 1215 Jefferson Davis Highway, Suite 1204, Arlington, VA 22202-4302. Respondents should be aware that notwithstanding any other provision of law, no person shall be subject to any penalty for failing to comply with a collection of information if it does not display a currently valid OMB control number.

**PLEASE DO NOT RETURN YOUR FORM TO THE ABOVE ADDRESS.**

1. REPORT DATE (DD-MM-YYYY)	2. REPORT TYPE	3. DATES COVERED (From - To)
05/03/2012	Final Performance Report	10/01/08-09/30/11
4. TITLE AND SUBTITLE		5a. CONTRACT NUMBER
Advanced Chemical Modeling for Turbulent Combustion Simulations		N/A
		5b. GRANT NUMBER
		FA9550-09-1-0069
		5c. PROGRAM ELEMENT NUMBER
		N/A
6. AUTHOR(S)		5d. PROJECT NUMBER
Heinz Pitsch		N/A
		5e. TASK NUMBER
		N/A
		5f. WORK UNIT NUMBER
		N/A
7. PERFORMING ORGANIZATION NAME(S) AND ADDRESS(ES)		
Leland Stanford Junior University, The Stanford University 340 Panama St Stanford, CA 94305-7209		
8. PERFORMING ORGANIZATION REPORT NUMBER		
N/A		
9. SPONSORING/MONITORING AGENCY NAME(S) AND ADDRESS(ES)		
USAF, AFRL DUMS 143574726 AF Office of Scientific Research, 875 N. Randolph St. Room 3112 Arlington, VA 22203 Chiping Li		
10. SPONSOR/MONITOR'S ACRONYM(S)		
AFOSR		
11. SPONSOR/MONITOR'S REPORT NUMBER(S)		
AFRL-OSR-VA-TR-2012-0990		
12. DISTRIBUTION/AVAILABILITY STATEMENT		
Unlimited		
Distribution A: Approved for Public Release		
13. SUPPLEMENTARY NOTES		
14. ABSTRACT		
The goals of this project were the development of new sub-filter models for large eddy simulation of turbulent combustion and of chemical mechanisms for jet fuel surrogates. The sub-filter modeling work focuses on the development of a framework for describing multiple combustion regimes using the flamelet approach, on describing the scalar dissipation rate in turbulent non-premixed combustion, and on modeling strain effects in turbulent premixed combustion. The chemistry work proposes a method for defining jet fuel surrogates, describes how different sub-mechanisms can be incorporated into the definition, and finally creates and validates a mechanism that serves as an accurate surrogate for jet fuel behavior.		
15. SUBJECT TERMS		
Combustion modeling, surrogate fuels, large-eddy simulation, partially premixed combustion, scalar dissipation rate		
16. SECURITY CLASSIFICATION OF:		
a. REPORT      b. ABSTRACT      c. THIS PAGE		
UU      UU      UU		
17. LIMITATION OF ABSTRACT		
UU		
18. NUMBER OF PAGES		
101		
19a. NAME OF RESPONSIBLE PERSON		
Chiping Li		
19b. TELEPHONE NUMBER (Include area code)		
(571) 481-6930		

# **Advanced Chemical Modeling For Turbulent Combustion Simulations**

*Final Report submitted by:*

Heinz Pitsch (PI)  
Stanford University  
Mechanical Engineering  
Flow Physics and Computation Group  
Stanford, CA 94305-3030

*Submitted to:*

Air Force Office of Scientific Research  
4015 Wilson Boulevard  
Room 713  
Arlington, VA 22203-1954

*for the period:*

October 1, 2008 through September 30, 2011

# Advanced Chemical Modeling For Turbulent Combustion Simulations

Aerospace, Chemical and Material Science Directorate  
Combustion and Diagnostics Program  
Dr. Chiping Li

## Abstract

This document serves as a final report to the Air Force Office of Scientific Research regarding activities performed under Grant # FA9550-09-1-0069, “Advanced Chemical Modeling For Turbulent Combustion Simulations.” The project had two goals. The first was the development of new sub-filter models for large eddy simulation of turbulent combustion, and the second was the development of chemical mechanisms for jet fuel surrogates. This report presents and discusses the models and the results that were produced within each project component. The sub-filter modeling work particularly focuses on the development of a framework for describing multiple combustion regimes using the flamelet approach, on describing the scalar dissipation rate in turbulent non-premixed combustion, and on modeling strain effects in turbulent premixed combustion. The chemical mechanism work proposes a method for defining jet fuel surrogates, describes how sub-mechanisms for a variety of alkanes and aromatics can be incorporated into the definition, and finally creates and validates a mechanism that serves as an accurate surrogate for jet fuel behavior.

## Contents

<b>1</b>	<b>Introduction</b>	<b>4</b>
<b>2</b>	<b>Advanced Sub-Filter Models For Large Eddy Simulation Of Turbulent Combustion</b>	<b>7</b>
2.1	Review Of Objectives . . . . .	7
2.2	Regime Independent Sub-Filter Combustion Modeling . . . . .	8
2.2.1	Single Regime Flamelet Models . . . . .	8
2.2.2	Multi-Regime Flamelet Model . . . . .	12
2.2.3	Extending The Regime Indicator To LES . . . . .	18
2.3	Validation Of The Multi-Regime Flamelet Model . . . . .	19
2.3.1	Triple Flame Description . . . . .	19
2.3.2	Triple Flame Results . . . . .	19
2.3.3	Summary . . . . .	27
2.4	Modeling Sub-Filter Scalar Dissipation In Turbulent Non-Premixed Flames	29
2.4.1	Motivation . . . . .	29
2.4.2	Modeling Background . . . . .	30
2.4.3	Auto-Igniting Jet . . . . .	32
2.4.4	Algebraic Model Performance . . . . .	34
2.4.5	An Adapted Dynamic LES Closure For The Dissipation Equation . . . . .	36
2.4.6	Transport Equation Model Performance . . . . .	42
2.4.7	Summary . . . . .	44
2.5	Modeling Sub-Filter Strain Effects In Turbulent Premixed Flames . . . . .	44
2.5.1	Motivation . . . . .	44
2.5.2	Case Description: Premixed Jet DNS . . . . .	45
2.5.3	Strained Premixed Flamelet Model . . . . .	45
2.5.4	LES Approach . . . . .	50
2.5.5	Results And Discussion . . . . .	51
2.5.6	Summary . . . . .	53
<b>3</b>	<b>Chemical Mechanisms For Jet Fuel Surrogates</b>	<b>54</b>
3.1	Review Of Objectives . . . . .	54
3.2	Definition Of Surrogates For Jet Fuels . . . . .	54
3.2.1	Choice Of Individual Components . . . . .	54
3.2.2	Composition Of Individual Components . . . . .	55
3.3	A Single Chemical Mechanism Describing A Jet Fuel Surrogate . . . . .	56
3.3.1	Extension To Substituted Aromatics . . . . .	56
3.3.2	Extension To <i>n</i> -Dodecane . . . . .	68
3.3.3	Extension To Methylcyclohexane . . . . .	78
3.4	Performance Of The Model Jet Fuel Surrogate . . . . .	89
<b>4</b>	<b>Conclusions</b>	<b>91</b>

# 1 Introduction

The application of computational models to multi-physics flow problems is becoming increasingly routine. The proliferation of computational resources, flow physics software, and data processing capabilities has provided modelers with the ability to analyze realistic engineering systems that are characterized by complex geometry, multiphase flow, and non-linear chemical interaction. In spite of their availability, computational flow physics models produce results that remain subject to large uncertainties. These uncertainties negatively impact the extent to which the model results can be relied upon for engineering development and analysis. A variety of research efforts are directed toward reducing this uncertainty and improving the usefulness of flow physics modeling frameworks. Efforts to develop more physically accurate models of reactive flow processes are among the most important of these efforts. Without the development of increasingly accurate physical models, the confidence bounds associated with multi-physics engineering analyses cannot be decreased.

In this project two categories of physical models are targeted. The first category consists of descriptions of turbulence and chemistry sub-filter interactions in Large Eddy Simulation (LES). The second category consists of descriptions of the evolution of the chemical kinetics of jet fuel. While both of these modeling topics have been widely studied [1, 2, 3], they represent two of the greatest modeling challenges within the wider landscape of physical flow modeling. For example, making assumptions about the combustion regimes that are found on sub-filter LES scales may result in dramatic mis-predictions of CO [4], while uncertainties in the prescription of kinetics rates can lead to vastly different NO predictions [5]. Advancing and further developing these models requires the application of fundamental theory, physical insight, and detailed comparisons with numerical and experimental validation cases. Each of these approaches will be relied upon in the sections that follow.

Activities related to the first project topic, which is the development and validation of a series of sub-filter models for reactive LES, are discussed in section 2. This section addresses modeling challenges from across the entire spectrum of combustion physics that are encountered in reacting flows. The greatest of these challenges is the treatment of the assumptions that are inherent in the flamelet approach. This approach is used for combustion modeling because it has historically offered the most accurate means of describing unresolved turbulence and chemistry interactions in LES. Flamelets, however, make detailed assumptions about the physics that govern combustion. These assumptions must change when the local flow conditions change and give rise to different types of combustion processes. Each combustion process can be characterized as belonging to a particular combustion regime, and here a model is developed that uses local transport information from a flow solver to predict which combustion regime will be present at any point in a simulation domain. Once this regime is known, appropriate flamelet assumptions can be applied in the flow solver. Application of these assumptions, however, requires information about the local flow field. In the non-premixed combustion regime, the most critical parameter describing the local flow field is the scalar dissipation rate. While widely studied, it is demonstrated in sec-

tion 2 that this quantity continues to be poorly predicted by current models. In response, a new model that adopts traditional LES dynamic machinery in a novel fashion is developed for the dissipation rate. Finally, the limit of premixed combustion, which represents a second distinct regime, is considered. A variety of models describing turbulent premixed flame propagation are available in literature. The most widely used models, however, are characterized by an inability to describe flame physics when turbulence becomes so intense that it perturbs the flame's structure. These scenarios (high Karlovitz number flames) are encountered just before a premixed flame is extinguished by turbulence. Describing the underlying physics correctly is therefore a requirement of any model that seeks to predict next generation, low pollutant premixed engine designs. Here, this challenge is addressed by formulating a new method of describing flame structure perturbations in LES.

The objective of the second project topic is to develop a capability to reliably predict the combustion characteristics of fuel oxidation and pollutant emissions from engines. The relevant fuel chemistry must be accurately modeled if this goal is to be achieved. Jet fuel, however, is made up of hundreds of hydrocarbons in proportions that can vary significantly between fuel samples. Consequently, only average fuel properties are known under the best of circumstances. A simplified fuel representation is required to circumvent this problem. Typically, jet fuels are modeled using a representative surrogate mixture, which is simply a well-defined mixture comprised of a few components. This surrogate's composition is chosen so that it mimics the physical and chemical properties of the real fuel under consideration. Guidelines have been developed by surrogate working groups [6, 7, 8] to determine the individual components that could make up such surrogate mixtures for a variety of specific fuels. Given knowledge of the target properties of the real fuel, and given a particular choice of individual components that will be used in the surrogate mixture, a constrained optimization approach can be applied to determine the exact composition of the surrogate mixture. An optimization tool that performs this task was developed under an earlier AFOSR grant, and is used in this project to determine a surrogate mixture composition that best matches the targeted fuel properties.

Once this optimization procedure was developed, the critical modeling need shifted toward the design of compact and reliable kinetic models that accurately describe the behavior of the components used in defining the surrogate. This issue is addressed in section 3. The kinetic models that are needed must be comprehensively validated for the individual components of the surrogate fuel, and then again validated after they are combined to form a final surrogate mixture. Though detailed mechanisms for many fuel components are available in literature, these existing mechanisms typically consist of several thousand species and reactions. Even single component mechanisms can reach this level of complexity, which precludes the coupling of the mechanism with a tractable flow modeling approach. Moreover, component mechanisms from different sources typically describe reaction pathways using different methodologies. These disparate descriptions are attributable to the uncertainties that exist in kinetic rate data. Multiply defined pathways render the process of combining detailed component mechanisms nearly impossible. In response to these challenges, a framework has been developed that consists of first reducing individual component mecha-

nisms, then combining them into a mixture characterizing a jet fuel surrogate, and finally further reducing and validating the combined surrogate definition. During this process, consistency is enforced amongst the formulations of each component mechanism, so that the kinetic rates of each reaction class do not suffer from duplication or conflicts in the final mechanism.

## 2 Advanced Sub-Filter Models For Large Eddy Simulation Of Turbulent Combustion

### 2.1 Review Of Objectives

Part one of this project sought to develop advanced sub-filter models for Large Eddy Simulation (LES) of turbulent combustion. Four specific goals were identified. The first was the development of a flamelet based chemical source term description that could accurately predict both premixed and non-premixed combustion regimes. The second goal was the creation of an LES description of premixed flame structure that, when used in multi-regime combustion environments, could seamlessly integrate with typical non-premixed combustion models. Increasing the fidelity of flamelet based LES predictions of pollutants such as  $\text{NO}_x$  and CO was a third goal. Finally, the fourth goal was the development of improved descriptions of turbulent premixed flame propagation speeds.

Here, the modeling and theory that was developed to accomplish these goals is highlighted in detail. First, a multi-regime combustion model that provides for the specification of chemical source terms in different regimes is discussed. This model builds upon the group's prior regime identification work to provide a model implementation characterized by improved tractability. The model is reviewed in section 2.2. Next, this multi-regime model is validated using a canonical flame case: a partially premixed triple flame. These cases are described and analyzed in section 2.3. They demonstrate that the multi-regime approach is capable of predicting flame behavior in both premixed and non-premixed regimes without the need for a user to make *a priori* assumptions about mixing dynamics. Additionally, the validation work in section 2.3 demonstrates the sensitivity that pollutant predictions have to burning regime. This sensitivity implies that the goal of increasing pollutant prediction accuracy is being implicitly accomplished through the multi-regime model.

Most combustion modeling approaches require accurate predictions of the sub-filter scalar dissipation rate. This quantity directly affects the evolution of pollutants, flame stability, and heat release. In section 2.4, large eddy simulations of a high fidelity direct numerical simulation (DNS) flame database demonstrate that the most traditional LES dissipation rate model can lead to dramatic underpredictions of sub-filter scalar dissipation. These underpredictions are addressed by considering a new transport equation closure of the dissipation rate. Specifically, an additional DNS describing scalar mixing in homogeneous turbulence is used to analyze closure models for the relevant transport equation. This analysis leads to the development of a new adapted dynamic procedure. As shown at the end of section 2.4, the use of the new transport equation closure in LES is shown to significantly improve dissipation rate predictions relative to the traditional modeling approach. As a result, the lift-off height and pollutant statistics of the high fidelity flame DNS are reproduced in LES with much greater accuracy.

Finally, the fourth goal of turbulent flame speed modeling is addressed in section 2.5. A focus is placed on described premixed flame propagation in high Karlovitz number regimes,

where turbulence can penetrate the inner layer of a flame and affect its structure. This physical process has been historically difficult to describe in LES because it occurs entirely on unresolved scales. Traditional flamelet models that assume a steady premixed flame structure fail to predict flame propagation under these circumstances. This challenge is addressed by introducing a new tabulation coordinate in the flamelet formalism to describe the sub-filter effects that turbulence has on the flame front. This new coordinate is shown to map out a wide range of premixed flame structures. The resulting flamelet model is tested by performing LES of an additional high fidelity premixed DNS case. The new model is able to reproduce the statistics and structure of the DNS flame where the traditional premixed flamelet approach could not.

## 2.2 Regime Independent Sub-Filter Combustion Modeling

Flamelet combustion models for LES are most often formulated for single regimes. Advancing the predictive capabilities of these models requires the development of formulations that can determine which mode of combustion occurs at a local point within a flow solver. This information can then be used to map in flamelet solutions whose assumptions are consistent with the local combustion regime. In this section, a tractable implementation of such a multi-regime flamelet model is developed. Such a discussion must begin with a review of single regime flamelet implementations.

### 2.2.1 Single Regime Flamelet Models

Burning in the purely non-premixed regime can be described using a standard non-premixed flamelet model [1, 9, 10, 11]. This approach relies on solutions of the steady non-premixed flamelet equations, which can be written [12]

$$-\rho \frac{\chi_Z}{2} \frac{\phi_k}{\bar{W}} \frac{\partial^2 \bar{W}}{\partial Z^2} + \rho \frac{\chi_Z}{2} \sum_m \left( \phi_k \frac{\partial^2 \phi_m}{\partial Z^2} + \frac{\phi_k \phi_m}{\bar{W}} \frac{\partial^2 \bar{W}}{\partial Z^2} \right) - \rho \frac{\chi_Z}{2} \frac{\partial^2 \phi_k}{\partial Z^2} = \rho \dot{\omega}_k, \quad (1)$$

$$-\rho \frac{\chi_Z}{2} \frac{1}{\bar{c}_p} \frac{\partial \bar{c}_p}{\partial Z} \frac{\partial T}{\partial Z} + \rho \frac{\chi_Z}{2} \sum_m \left( \frac{\partial \phi_m}{\partial Z} + \frac{\phi_m}{\bar{W}} \frac{\partial \bar{W}}{\partial Z} \right) \left( 1 - \frac{c_{p,m}}{\bar{c}_p} \right) \frac{\partial T}{\partial Z} - \rho \frac{\chi_Z}{2} \frac{\partial^2 T}{\partial Z^2} = \rho \frac{\dot{Q}}{\bar{c}_p}. \quad (2)$$

The scalar dissipation rate in Eq. (2),  $\chi_Z = 2\mathcal{D}_Z(\nabla Z \cdot \nabla Z)$ , is an external parameter in the equation and is modeled as a prescribed function of  $Z$  [1, 12],

$$\chi_Z = \chi_{Z,\text{st}} \cdot \frac{\exp\left(-2 [\text{erfc}^{-1}(2Z)]^2\right)}{\exp\left(-2 [\text{erfc}^{-1}(2Z_{\text{st}})]^2\right)}, \quad (3)$$

where the reference dissipation rate at the stoichiometric mixture fraction is  $\chi_{Z,\text{st}}$ . The flamelet space boundary conditions that are relevant for the laminar flames being considered below are  $T = 300$  K at both  $Z=0$  and  $Z=1$ .

The non-premixed flamelet solutions can be tabulated in a database as a function of  $Z$  and  $C$  [10]. Representative non-premixed flamelets that are used for modeling the validation

cases in section 2.3, and their associated S-shaped curve [1], are plotted in Fig. 1. The plot of the S-shaped curve shows that several flamelets from the so-called lower branch are included in the flamelet solution set. The lower branch is defined with respect to the turning point, or the maximum reference scalar dissipation rate that can be observed in a flamelet before quenching occurs. Flamelets that have maximum temperatures and dissipation rates that are smaller than the temperature and dissipation rate of the flamelet at the turning point are said to exist on the lower branch of the S-shaped curve. These solutions are unstable in the sense that they will respond to small perturbations by moving either toward the stable upper branch or toward a stable quenched solution. Because of this response, the usefulness of lower branch solutions in non-premixed flamelet modeling remains ambiguous.

Compounding this ambiguity, it is known [13] that the treatment of flamelet space below the turning point can influence flame behavior. For example, when the flamelet solution at the turning point is taken to be the first available burning solution above the mixing line (the completely quenched state), then all flamelet information between the mixing line and this first available flamelet would be determined using interpolation. These interpolated values are expected to be different than the values associated with flamelet solutions from the lower branch of the S-shaped curve. In comparison with a purely non-premixed flamelet model, one advantage of a multi-regime modeling approach is that it tends to access the premixed regime in these regions of  $Z$  and  $C$  space where the progress variable is not near its maximum value. A multi-regime approach therefore negates some of the ambiguity associated with the lower branch solutions. Note that when the limit of purely non-premixed combustion is considered, the lower branch flamelets will be used without modification. The fully quenched mixing line will also be included in flamelet space, and regions between the lower branch and the mixing line will be accessed using interpolation. Once non-premixed flamelet databases are formed, the purely non-premixed model can be applied to laminar flames by solving transport equations for the mixture fraction  $Z$  and the progress variable  $C$ .

A purely premixed flamelet model can be similarly developed. The premixed model is based on a coupled level set and progress variable approach [14] that is extended through the use of a technique from the Flamelet Generated Manifold (FGM) methodology [15]. Flamelet solutions are created for this purely premixed approach by using the FlameMaster program [16] to solve the steady unstrained premixed flamelet equations,

$$\rho_u s_{L,u} \frac{d}{dx}(\phi_k) = \frac{d}{dx} \left( \rho \phi_k V_{k,j}^{diff} \right) + \rho \dot{\omega}_k, \quad (4)$$

$$\rho_u s_{L,u} \frac{d}{dx}(T) = \frac{1}{\bar{c}_p} \left[ \frac{d}{dx} \left( \rho \mathcal{D}_T \bar{c}_p \frac{dT}{dx} \right) + \rho \dot{Q} \right] + \frac{1}{\bar{c}_p} \left[ \sum_k \left( \rho c_{p,k} \frac{dT}{dx} \phi_k V_{k,j}^{diff} \right) \right], \quad (5)$$

where  $s_{L,u}$  is the eigenvalue of the problem that represents the laminar flame speed,  $\rho_u$  is the density on the unburned side of the flame, and  $x$  is a physical space coordinate. The diffusion velocity  $V_{k,j}^{diff}$  is usually modeled by assuming Fickian diffusion. Representative premixed flamelet solutions that are used for validation in section 2.3 are plotted in Fig. 2. The lean and rich flammability limits associated with premixed burning appear in this

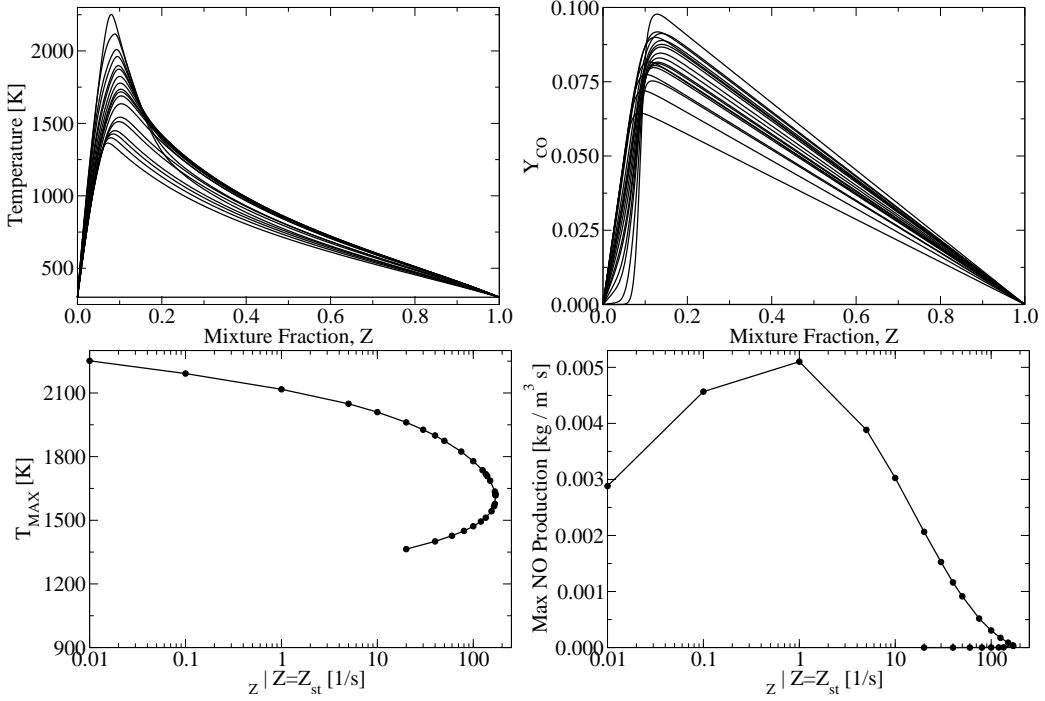


Figure 1: Representative on-premixed flamelets. First plot: flamelet temperature profiles; Second plot: flamelet CO mass fraction profiles; Third plot: maximum flamelet temperature vs.  $\chi_{Z,st}$ ; Fourth plot: maximum NO production vs.  $\chi_{Z,st}$ . The  $\chi_{Z,st}$  values in the lower row plots are taken from the flamelets in the upper row.

figure at mixture fractions of approximately  $Z_{LFL} = 0.03$  and  $Z_{RFL} = 0.26$ , respectively. A comparison of Figs. 1 and 2 reveals the effect of a change of the combustion regime. For example, CO mass fractions in the premixed regime reach values approximately twice as large as the CO mass fractions in the non-premixed regime. Similarly, the maximum observed temperature in the two regimes at  $Z=0.2$  differs by approximately 150 K.

Just as in the non-premixed model, the flamelets are tabulated as a function of  $Z$  and  $C$ . Any scalar quantity  $\phi_k$  can then be accessed as  $\phi_k = \phi_k(Z, C)$ . Because of the premixed flammability limits, however, mixture fraction values outside of  $Z_{LFL}$  and  $Z_{RFL}$  are not available in the premixed solution space. A special extension procedure is therefore needed to describe very lean or very rich mixture fractions. Here, a technique based on the flamelet generated manifolds (FGM) model [15] will be used to perform the extension. In this technique, scalar information at a  $Z$  value sitting between a flammability limit and a  $Z$  boundary value is determined by interpolating between the premixed solution at the

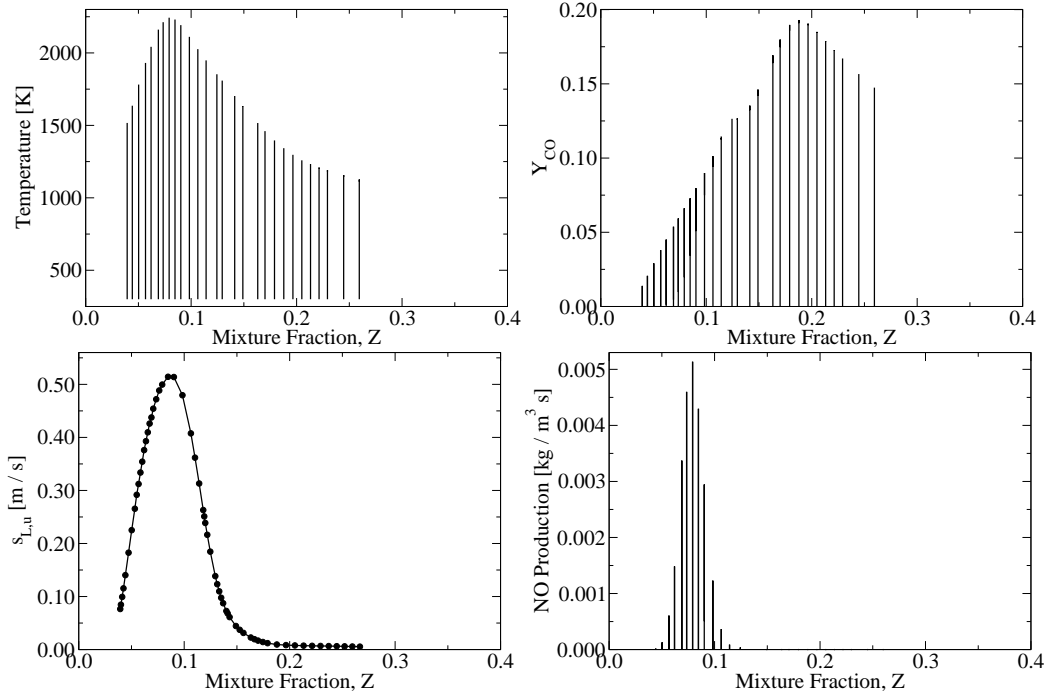


Figure 2: Representative premixed flamelets. First plot: flamelet temperature profiles; Second plot: flamelet CO mass fraction profiles; Third plot: burning velocity as a function of  $Z$ ; Fourth plot: flamelet NO production profiles.

flammability limit and the unburned solution at the  $Z$  boundary,

$$\begin{aligned} \phi_k(Z, C) &= \phi_k(Z_{RFL}, C) \cdot \left( \frac{1 - Z}{1 - Z_{RFL}} \right) \\ &+ \phi_k(Z = 1, C = 0) \cdot \left( \frac{Z - Z_{RFL}}{1 - Z_{RFL}} \right) \quad \forall \ Z > Z_{RFL}, \end{aligned} \quad (6)$$

$$\begin{aligned} \phi_k(Z, C) &= \phi_k(Z_{LFL}, C) \cdot \left( \frac{Z - 0}{Z_{LFL} - 0} \right) \\ &+ \phi_k(Z = 0, C = 0) \cdot \left( \frac{Z_{LFL} - Z}{Z_{LFL} - 0} \right) \quad \forall \ Z < Z_{LFL}. \end{aligned} \quad (7)$$

Note that a multi-regime model will again help to remove the ambiguity associated with this extrapolation because it tends to access non-premixed flamelet space at mixture fraction values outside of the flammability limits. In multi-regime approaches, the particular interpolation technique that is used for premixed flamelet extension takes on a reduced importance.

In fully resolved simulations such as the laminar flames considered here, a progress variable equation can be solved without the use of any special numerical techniques. For

example, a progress variable is solved for directly in the counter flow flame simulation presented in section ???. In this approach a progress variable source term from a flamelet solution is directly introduced in the  $C$  transport equation. In standard implicitly filtered LES simulations, however, progress variable profiles tend to be underresolved around flame fronts, and special numerical techniques are needed to address the resulting problems [14, 17, 18]. Therefore, in an effort to consider flamelet combustion models that are applicable to LES, the triple flame simulation will couple the solution of a level set to the progress variable field. Although it is not needed in a fully resolved simulation, this coupling would ensure that the progress variable's description of the flame front would propagate at the correct speed even if the progress variable field were to transition from unburned to burned over a single mesh cell. A level set will be defined using a field variable labeled as  $G$ , and the particular level set of this variable that denotes the flame front is set as  $G = G_0$ . This level set is governed by the equation [1, 14, 17],

$$\begin{aligned} \frac{\partial}{\partial t}(G) + u_j \frac{\partial}{\partial x_j}(G) &= \frac{\rho_u}{\rho} (\mathcal{D}_u \kappa + s_{L,u}) |\nabla G| \quad \forall \quad G = G_0, \\ |\nabla G| &= 1 \quad \forall \quad G, \end{aligned} \quad (8)$$

where  $\kappa$  is the curvature of the flame front, where  $\mathcal{D}$  is the progress variable diffusivity at the flame front, and where the  $u$  subscript represents conditioning on the unburnt side of the front. When solving Eq. (8), the flame speed  $s_{L,u}$  is determined by accessing the tabulated premixed flamelet solutions. The computed burning velocities shown in Fig. 2 are therefore directly incorporated in the premixed model framework through the level set equation.

In the premixed flamelet model, the transport equation for the level set is solved in addition to the  $Z$  and  $C$  expressions shown in Eqs. (??) – (??). The progress variable equation is coupled to the level set by formulating the progress variable source term,  $\dot{\omega}_C$ , as a function of both the level set and the tabulated premixed solution. This coupling ensures that the iso-contour of the progress variable that is associated with the flame front is always consistent with the position of the level set. The details of the coupling are described elsewhere [14].

### 2.2.2 Multi-Regime Flamelet Model

The two single regime models that have been presented can be combined to form a multi-regime flamelet model. This multi-regime model must accomplish two tasks. It must first provide a means of distinguishing which regime is present at a particular mesh cell and particular point in time, and it must additionally provide a means of transitioning between solutions from the individual regimes. The multi-regime approach that is used here is based on a flamelet transformation in which the statistical dependence of mixture fraction and progress variable are accounted for [19]. This approach will now be described.

In the asymptotic limit of purely non-premixed combustion, reactive source terms are balanced by diffusive transport that occurs in the direction of mixture fraction gradients.

The non-premixed flamelet equations that are shown in Eqs. (1) – (2) are derived by performing a coordinate transformation that explicitly captures this balance. Conversely, in the limit of purely premixed combustion reactive source terms are balanced by diffusive transport that occurs along vectors where the mixture fraction is constant. The premixed flamelet equations shown in Eq. (5) explicitly capture this second type of reaction and diffusion balance. If a multi-regime model is to determine which of these asymptotic regimes is most descriptive of the combustion at a given flow location, the balance between reaction and diffusion processes must be examined. If reaction is primarily balanced by transport of the mixture fraction, then the local regime can be said to be non-premixed. Conversely, if reaction is balanced by transport along vectors of constant mixture fraction, then the local regime can be said to be premixed.

Traditional mixture fraction and progress variable based flamelet methods present a challenge to the examination of these transport processes. This challenge arises because  $Z$  and  $C$  are not statistically independent. In the limit of non-premixed combustion, for example, a change in the mixture fraction field will be accompanied by a change in the progress variable field. Consequently, observations of diffusive progress variable transport do not conclusively indicate the presence of a particular combustion regime. If diffusive transport is to be definitively associated with the premixed or the non-premixed regime, the statistical dependence of  $C$  and  $Z$  must be properly accounted for. In reference [19], this dependence is treated by defining a variable,  $\Lambda$ , that is analogous to the traditional progress variable. The  $\Lambda$  variable has been previously considered [10, 11], and can be most easily described as a modified reactive coordinate whose value is constant over a single non-premixed flamelet. Mathematically, the  $\Lambda$  value that is associated with a single flamelet might be defined as the value of the progress variable  $C$  that occurs at the flamelet's stoichiometric mixture fraction [19]. Because non-premixed flamelet solutions each have slightly different progress variable profiles, the  $\Lambda$  value associated with each non-premixed flamelet will be unique. Additionally, because  $\Lambda$  is constant over an entire non-premixed flamelet, it provides a measure of reaction progress that is statistically independent of the mixture fraction.  $\Lambda$  is therefore useful to an examination of the nature of local transport processes. The purely premixed limit will be indicated by significant transport of the  $\Lambda$  variable and no transport of the  $Z$  variable. Conversely, the purely non-premixed limit will be indicated by significant transport of the  $Z$  variable and, since  $\Lambda$  is constant along a non-premixed flamelet, no transport of the  $\Lambda$  variable.

Figure 3 shows a series of non-premixed flamelet solutions in a way that emphasizes the physical meaning of the  $\Lambda$  variable. The same steady, non-premixed flamelet solutions that were shown in Fig. 1 are plotted in Fig. 3 in  $(Z, \Lambda)$  space. The height of the plotted surface indicates the local value of the progress variable  $C$  in this space, while the color contours indicate the corresponding value of temperature. As described above, the  $\Lambda$  variable is constant in value throughout a single non-premixed flamelet solution. Consequently, a single flamelet solution can be recovered from Fig. 3 by extracting data along a constant value of the  $\Lambda$  coordinate. Additionally, Fig. 3 demonstrates that it is possible to move within a flamelet solution where  $\Lambda$  is constant and still allow both  $Z$  and  $C$  to change.

This coordinate independence is what enables the rigorous separation of non-premixed and premixed transport processes. One final aspect of Fig. 3 that is relevant to the proposed multi-regime modeling approach is the sharp change in topology that occurs along the line where  $\Lambda = 0.15$ . This topological change appears as a discontinuity in the slope of the progress variable surface, and it identifies the last steady, burning flamelet solution that is solved for. The only flamelet solution with a lower maximum temperature is the non-burning mixing solution that exists at  $\Lambda = 0.0$ . Fig. 3 demonstrates how linear interpolation is used to populate this unstable region of flamelet space.

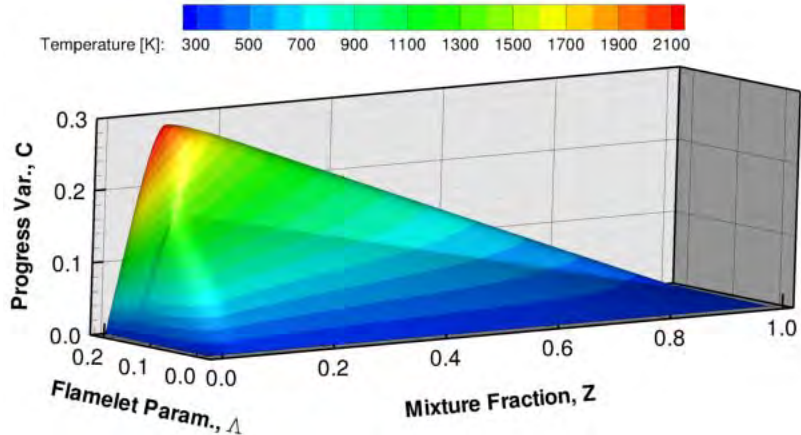


Figure 3: The steady non-premixed flamelet solutions from Fig. 1, plotted in  $(Z, \Lambda)$  space. The height of the contour surface shows the value of the progress variable in the flamelet solutions, while the color contours show the value of temperature.

Once  $Z$  and  $\Lambda$  are selected as independent coordinates, the magnitude of their associated fluxes can be isolated in a scalar transport equation by applying flamelet-type coordinate transformation rules such as [1],

$$\frac{\partial(\cdot)}{\partial x_j} \rightarrow \frac{\partial Z}{\partial x_j} \frac{\partial(\cdot)}{\partial Z} + \frac{\partial \Lambda}{\partial x_j} \frac{\partial(\cdot)}{\partial \Lambda} + \frac{\partial e}{\partial x_j} \frac{\partial(\cdot)}{\partial e}. \quad (9)$$

This particular rule is valid for the scalar gradient operator. If changes along the third coordinate  $e$  are assumed to be small, then a 2-D flamelet equation in  $Z$  and  $\Lambda$  space can be produced using this transformation [19]. After the neglect of unsteady terms and the use of asymptotic arguments, the transformed equation for the progress variable may be written,

$$\frac{\partial C}{\partial \Lambda} [\rho_u s_{L,u} |\nabla \Lambda| - \nabla \cdot (\rho \mathcal{D} \nabla \Lambda)] - \rho \frac{\chi_Z}{2} \frac{\partial^2 C}{\partial Z^2} = \rho \dot{\omega}_C. \quad (10)$$

The first set of terms on the left hand side of this equation can be recognized as sharing the form of the transport terms in the premixed flamelet equations (Eq. (5)), while the second term on the left hand side is simply the diffusion term from the non-premixed

flamelet equations (Eq. (2)). The right hand side represents the chemical source term, demonstrating again that the local combustion regime can be determined by examining which mixing process acts as the sink for the chemical source.

A model for determining the combustion regime at a given temporal and spatial location directly follows from this transformation. The terms on the left hand side of Eq. (10) can be grouped according to the regime they describe, locally calculated in the flow solver, and then compared to one another to determine each regime's contribution to the chemical source term budget. More explicitly, the terms are grouped to form the regime specific quantities  $\Theta_{pre}$  and  $\Theta_{non}$ ,

$$\Theta_{pre} = \frac{\partial C}{\partial \Lambda} [\rho_u s_{L,u} |\nabla \Lambda| - \nabla \cdot (\rho \mathcal{D} \nabla \Lambda)], \quad (11)$$

$$\Theta_{non} = -\rho \frac{\chi_Z}{2} \frac{\partial^2 C}{\partial Z^2}, \quad (12)$$

where  $\Theta_{pre}$  describes how the source term is balanced in the premixed limit and  $\Theta_{non}$  describes how the source term is balanced in the non-premixed limit. Note that outside of the premixed flammability limits, the laminar burning velocity  $s_{L,u}$  effectively becomes zero. The premixed and non-premixed terms can be very simply compared to determine their relative importance,

$$\Theta = \frac{\Theta_{pre}}{\Theta_{non}}. \quad (13)$$

When  $\Theta \ll 1$ , the regime is definitively non-premixed. Conversely, the regime is definitively premixed when  $\Theta \gg 1$ .

The  $\Theta$  variable serves to characterize the local combustion regime in an asymptotic sense, but it does not describe how solutions from different regimes should be combined when their relative contributions to the chemical source term are similar in magnitude. Such a regime combination algorithm is the second task required of a multi-regime model. Here, a simple weighting procedure is used to determine the local contribution of each regime. Flamelet solutions from the non-premixed regime will be labeled as  $\phi_{k,non}(Z, C)$ , while flamelet solutions from the premixed regime will be labeled  $\phi_{k,pre}(Z, C)$ . These solutions will be combined at any temporal and spatial location according to the rule

$$\phi_k(\xi, Z, C) = \phi_{k,non}(Z, C) \cdot (1 - \xi) + \phi_{k,pre}(Z, C) \cdot \xi, \quad (14)$$

where the weighting coefficient  $\xi$  is

$$\xi = \frac{\int_V \Theta_{pre} dV}{\max(\int_V \Theta_{pre} dV + \int_V \Theta_{non} dV, \epsilon)}, \quad (15)$$

and where  $\epsilon$  is a small, positive number and  $V$  is the volume of a domain comprised of the neighboring computational cell in each direction. The  $\epsilon$  term is employed to ensure that the regime is always well defined, while the integration is employed to ensure that transitions between regimes are smooth. The limiting cases of fully premixed and fully non-premixed

combustion are captured by this weighting procedure, since  $\xi \rightarrow 1$  when  $\Theta_{pre} \gg \Theta_{non}$ , and conversely  $\xi \rightarrow 0$  when  $\Theta_{non} \gg \Theta_{pre}$ .

It is important to note that the quantities  $\Lambda$ ,  $\partial C / \partial \Lambda$ , and  $\partial^2 C / \partial Z^2$ , are not immediately available from transport equations. These quantities can either be solved for in flamelet space and accessed from the tabulated flamelet solutions as needed, or they could be calculated by considering the conditional dependence of  $C$  on  $Z$  and  $\Lambda$  within a region surrounding the spatial location of interest. In the flames considered here, the  $\partial^2 C / \partial Z^2$  term is calculated directly from the non-premixed flamelet solutions, and stored with these solutions so that it can be accessed using the  $Z$  and  $C$  scalars. Similarly,  $\Lambda$  and  $\partial C / \partial \Lambda$  could be calculated from non-premixed flamelets by assigning each flamelet an appropriate value of the  $\Lambda$  variable and then differentiating.

When quantities such as  $\partial^2 C / \partial Z^2$  are evaluated using non-premixed flamelets, a modeling assumption is being invoked. These flamelet-based evaluations assume that non-premixed transport can be effectively measured by treating local flame structure as non-premixed. If this non-premixed treatment is valid, then it is of course valid to take  $\partial^2 C / \partial Z^2$  from a non-premixed flamelet. If the local flame structure is premixed, however, then  $\partial^2 C / \partial Z^2$  might no longer be accurately described by a non-premixed flamelet. Nonetheless, it would be expected that in a premixed combustion regime the  $\chi_Z$  term that is evaluated from the flow solver would be small. This small value of  $\chi_Z$  would tend to drive the non-premixed transport term  $\Theta_{non}$  toward zero, and minimize the influence of  $\partial^2 C / \partial Z^2$ . Additionally, the presence of significant premixed transport would drive up the magnitude of the premixed term  $\Theta_{pre}$ . The regime indicator would accordingly predict premixed combustion. It is therefore expected that  $\partial^2 C / \partial Z^2$  can be safely evaluated from non-premixed flamelets in both limiting regimes. The laminar flame simulations that are presented below confirm this expectation.

Although the  $\Lambda$  variable successfully accounts for the statistical dependence of  $Z$  and  $C$ , it is recognized to be a challenging quantity from both a physical and computational standpoint. Furthermore, its definition allows for some uncertainty. For example,  $\Lambda$  is defined in the context of non-premixed flamelets, but Figs. 1 – 2 hint that a possibility exists of finding a higher value of  $C$  in premixed flamelet space than in non-premixed flamelet space. If this difference of maximum progress variable values were to occur, an arbitrary means of extrapolating a value of  $\Lambda$  to a higher value of progress variable would have to be introduced in premixed regions of a flow field. In an effort to minimize these practical challenges, an alternative method of accounting for the dependence of  $Z$  and  $C$  is proposed.

This method retains the use of a flamelet transformation based on the  $\Lambda$  variable, but once the  $\Theta_{pre}$  term has been defined transformation rules such as those in Eq. (9) are again applied to  $\Theta_{pre}$ . These transformation rules are used to change the dependencies on  $\Lambda$  to

dependencies on  $C$  and  $Z$ . After manipulation, the form of the  $\Theta_{pre}$  term becomes

$$\begin{aligned}\Theta_{pre} = & \rho_u s_{L,u} \left[ |\nabla C| - \frac{\partial C}{\partial Z} |\nabla Z| \right] \\ & - \left[ \nabla \cdot (\rho \mathcal{D} \nabla C) - \frac{\partial C}{\partial Z} (\nabla \cdot (\rho \mathcal{D} \nabla Z)) - \rho \frac{\chi_Z}{2} \frac{\partial^2 C}{\partial Z^2} \right].\end{aligned}\quad (16)$$

It can be seen that this method subtracts out the progress variable's dependence on mixture fraction in an explicit fashion, rather than through a specially defined variable. Note that the  $\Theta_{non}$  term remains unchanged relative to Eq. (12) in this modified formulation. In the simulations that follow the regime indicator  $\xi$  will be defined according to Eq. (21) using  $\Theta_{pre}$  from Eq. (16) and  $\Theta_{non}$  from Eq. (12). Note that the flame simulations shown below in sections 2.3.2 and ?? indicate that a regime formulation based on  $\Lambda$  yields results that are very similar to the results of the modified formulation. Because of the challenges associated with  $\Lambda$ , the results of the more tractable modified formulation shown in Eq. (16) are presented throughout the remaining sections.

Regardless of how  $\Theta_{pre}$  is calculated, it can be seen that both sides of the flamelet transformation in Eq. (10) approach zero in non-reactive areas of the flow field [19]. The regime indicator  $\xi$  then ceases to provide information. This does not cause difficulties in unburned gas, since premixed and non-premixed flamelets have identical chemical states at a given mixture fraction and zero progress variable. At fully burned conditions, however, this issue needs to be considered because the production of pollutants or soot may be sensitive to the composition of the burned gas. Similarly, regime dependencies need to be considered in the preheat regions of premixed flames, where diffusion leads to a temperature increase but where reaction is not yet significant [19]. In these preheat regions, diffusive and convective premixed transport processes cancel with one another, and the premixed transport term  $\Theta_{pre}$  would diminish to zero even though the regime is definitively premixed.

These issues will be accounted for in the multi-regime model by forcing the premixed term  $\Theta_{pre}$  to be at least as large as the premixed convective flux term,

$$\Theta_{pre} = \max \left( \Theta_{pre}, \rho_u s_{L,u} \left[ |\nabla C| - \frac{\partial C}{\partial Z} |\nabla Z| \right] \right). \quad (17)$$

This bounding operation ensures that premixed transport will be appropriately captured even in regions where premixed diffusive transport and premixed convective transport oppose one another. Consequently, premixed transport will be observed even in preheat regions of premixed flame fronts, where chemical source terms are small. Note that this bounding operation should never activate in reactive gas, because in the presence of significant reaction the diffusive term is expected to be negative, and to therefore provide a net positive addition to  $\Theta_{pre}$ .

A similar kind of ambiguity exists in the non-premixed flamelet equations. At mixture fraction values away from stoichiometric burning conditions, the second derivative term in Eq. (12) tends toward zero. Consequently, the measured non-premixed transport term  $\Theta_{non}$  tends toward zero. It is therefore possible to find flow regions that are non-premixed

in nature, but that are subject to only very weak transport in mixture fraction space. In an effort to ensure that these flow regions are treated correctly, the second derivative in the non-premixed term  $\Theta_{non}$  will be bounded by the model parameter  $\gamma$ ,

$$\Theta_{non} = -\rho \frac{\chi_Z}{2} \cdot \min \left( \frac{\partial^2 C}{\partial Z^2}, \gamma \right). \quad (18)$$

Note that the second derivative in this equation is taken from flamelet space, while the dissipation rate is taken from the flow solver. Bounding the second derivative by  $\gamma$  ensures that the regime indicator treats marginally reacting regions where there is a high mixture fraction dissipation rate and almost no premixed transport as non-premixed.  $\gamma$  should be much smaller than the value of the second derivative at the most reactive mixture fraction, so that it does not influence the regime model in reacting flow regions. For example, in the remaining sections the  $\gamma$  parameter is set equal to  $\gamma = -1$ , which is less than 1% of the peak magnitude of the second derivatives found in the non-premixed flamelets shown in section 2.2.1.

Taken together, these premixed and non-premixed bounding operations serve to ensure that the local regime tends toward premixed in non-reactive areas where  $\chi_Z$  asymptotes to zero, and towards non-premixed in non-reactive areas where  $\chi_Z$  is significant.

### 2.2.3 Extending The Regime Indicator To LES

The regime indicator can be extended to LES by considering filtered transport terms. For example, after LES filtering the mixing terms that result from the coordinate transformation can be written,

$$\overline{\Theta}_{pr} = \rho_u s_{T,u} \left( |\nabla \widetilde{C}| - \frac{\widetilde{\partial C}}{\partial Z} |\nabla \widetilde{Z}| \right) - \nabla \cdot \left( \overline{\rho} \widetilde{D} \nabla \widetilde{C} \right) \quad (19)$$

$$+ \frac{\widetilde{\partial C}}{\partial Z} \left( \nabla \cdot \left( \overline{\rho} \widetilde{D} \nabla \widetilde{Z} \right) \right) + \rho \frac{\widetilde{\chi}_Z}{2} \frac{\widetilde{\partial^2 C}}{\partial Z^2} + \overline{\Theta}_{pr,sfs},$$

$$\overline{\Theta}_{np} = -\overline{\rho} \frac{\widetilde{\chi}_Z}{2} \frac{\widetilde{\partial^2 C}}{\partial Z^2} + \overline{\Theta}_{np,sfs}. \quad (20)$$

A filtered regime indicator may then be formed by comparing the magnitudes of these mixing terms,

$$\overline{\xi} = \frac{\int_V \overline{\Theta}_{pr} dV}{\max(\int_V \overline{\Theta}_{pr} dV + \int_V \overline{\Theta}_{np} dV, \epsilon)}. \quad (21)$$

Once the regime indicator  $\overline{\xi}$  is known, the premixed flamelet solutions  $\widetilde{\phi}_{k,pr}$  and the non-premixed flamelet solutions  $\widetilde{\phi}_{k,np}$  will be combined for use in a flow solver according to the construct

$$\widetilde{\phi}_k(\overline{\xi}, \widetilde{Z}, \widetilde{Z''^2}, \widetilde{C}, \widetilde{C''^2}) = \widetilde{\phi}_{k,np}(\widetilde{Z}, \widetilde{Z''^2}, \widetilde{C}) \cdot [1 - \overline{\xi}] + \widetilde{\phi}_{k,pr}(\widetilde{Z}, \widetilde{C}, \widetilde{C''^2}) \cdot [\overline{\xi}]. \quad (22)$$

## 2.3 Validation Of The Multi-Regime Flamelet Model

In this section a laminar flame will be simulated for the purpose of validating the multi-regime flamelet model. The flame that is chosen is a canonical partially premixed triple flame. This flame will be described using four distinct descriptions of chemistry: 1) finite rate chemistry; 2) the multi-regime flamelet model; 3) a purely non-premixed flamelet model; and 4) a purely premixed flamelet model.

### 2.3.1 Triple Flame Description

A laminar triple flame similar to the flames studied by Favier and Vervisch [20] and Knudsen and Pitsch [19, 21] is selected as a validation case. A schematic of this case is shown in Fig. 4, where the progress variable and mixture fraction in the flame is plotted at initialization and then again at a time when the flame is nearing steady state. In addition to the progress variable, Fig. 4 denotes the simulation's inlet and outlet, as well as the mixture fraction stratification imposed at the inlet. All of the triple flame simulations are initialized by placing two counterrotating vortices in the middle of a 9 mm  $\times$  6 mm 2-D domain. These vortices are introduced in order to force the flame front to experience a variety of transient mixing conditions. Behind the vortices, a progress variable profile in the form of a hyperbolic tangent along the downstream direction is introduced. The mixture fraction in the downstream region is set to have a constant stoichiometric value. Tabulated premixed flamelet solutions are then accessed using the  $Z$  and  $C$  profiles to set the initial values of the individual chemical species and temperature in the domain. The inlet of the simulation, which encompasses the entire left edge of the domain, is set to have a constant bulk value of downstream velocity ( $U=0.72$  m/s) and zero cross-stream velocity. The species and temperature profiles along this inlet are set to fully unburnt values, but a mixture fraction gradient is created in the cross-stream direction along the inlet so that the effects of both premixed and non-premixed combustion can be considered. The mixture fraction at the top edge of the inlet is set as  $Z=0.0$ , while the mixture fraction at the bottom edge of the inlet is set as  $Z=0.5$ . At the time of initialization, this cross-stream gradient of mixture fraction extends downstream to the vortices. The outlet boundary conditions, which are active on the right edge of the domain, are solved using a convective equation. The boundaries at the top and bottom of the domain are set as slip walls. The simulation is run until the influence of the vortices has disappeared and a steady, propagating triple flame has formed.

### 2.3.2 Triple Flame Results

#### *Progress Variable Comparison*

Progress variable fields from the finite rate triple flame solution and from each of the flamelet model solutions are shown in Fig. 5. The plots represent information from three distinct points in time, with time increasing from left to right. The finite rate solution is shown in the top row of the figure, while the flamelet model solutions are shown in the lower rows.

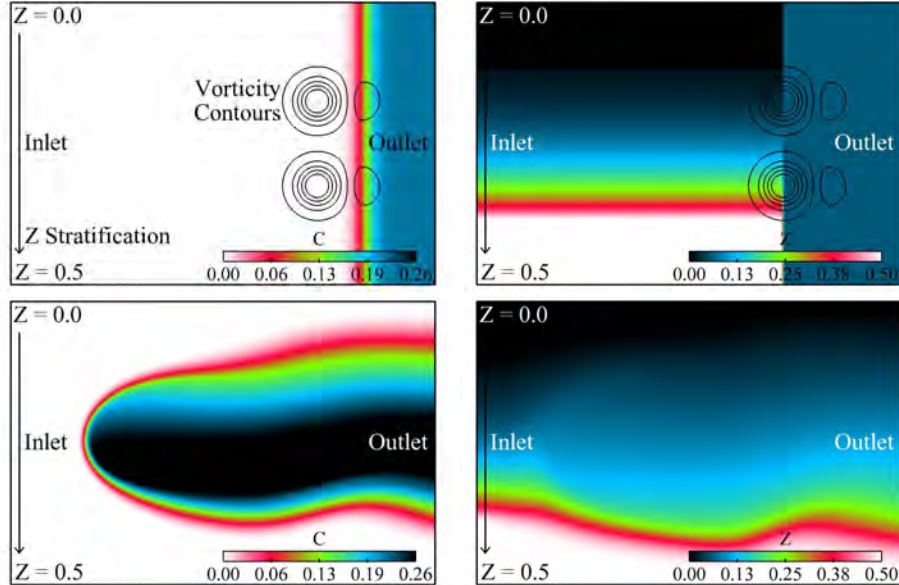


Figure 4: Schematic of the triple flame simulation. The first two plots show the progress variable  $C$  and mixture fraction  $Z$  at initialization. The second two plots show these quantities once the propagating triple flame has formed.

The flamelet models capture the general flow features of the ‘true’ finite rate solution reasonably well. In the first and third columns of Fig. 5, for example, the flamelet models reproduce all of the global structures that are observed in the finite rate case. Although these global structures are accurately described, the modeled solutions do have difficulty capturing several details of the finite rate solution. Especially at the intermediate time shown in the figure’s second column, the flamelet models alter the evolution of flame-vortex interactions relative to the finite rate solution. Additionally, the figure’s third column shows that the propagation speed of the leading triple flame edge depends on the modeling approach. These differences in the progress variable field hint at the more significant differences that appear when details of the flame structure are considered.

#### Regime Predictions

The regime indicator  $\xi$  from Eq. (21) is plotted in the multi-regime model simulations in Fig. 6. In this plot, black coloring ( $\xi = 1$ ) indicates that the local combustion regime is premixed, while white coloring ( $\xi = 0$ ) indicates the local regime is non-premixed. The indicator predicts that the leading edge of the flame front is definitively premixed, while the trailing region of the flame tends to be largely non-premixed. These results are consistent with the sharp progress variable gradients that occur at the flame front, and with the weak mixture fraction diffusion that occurs across the middle of the burnt gas behind the flame front.

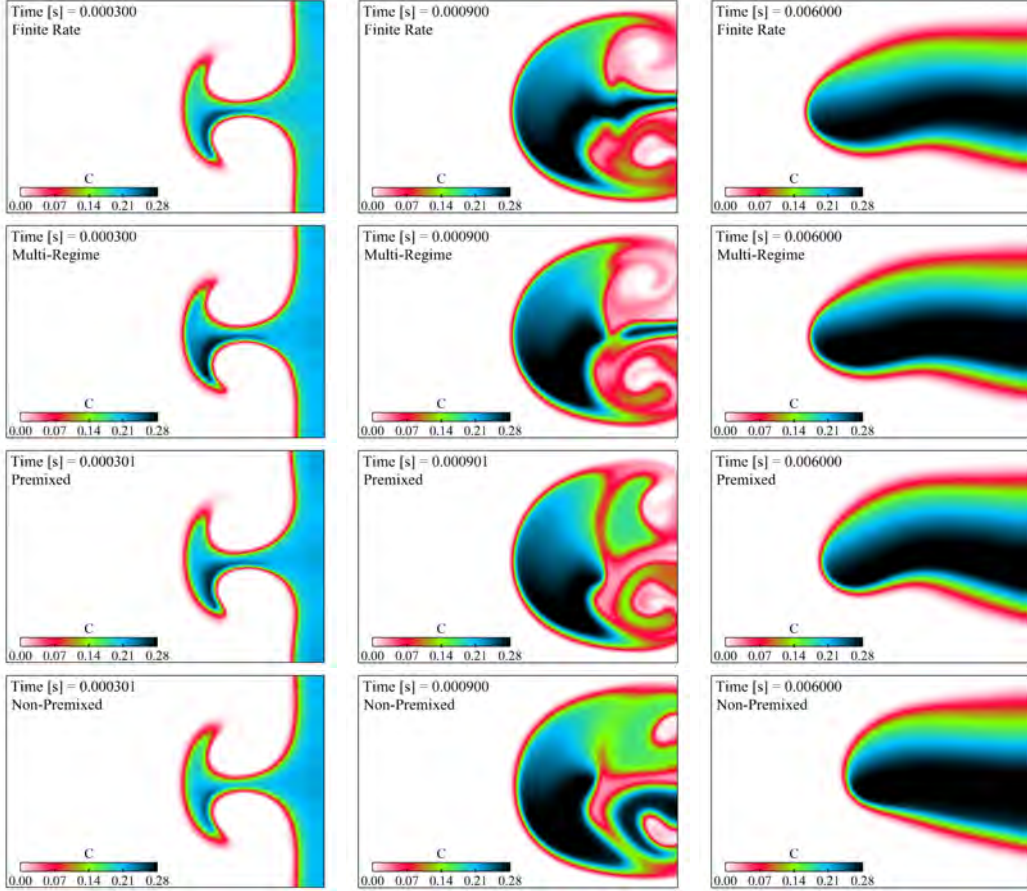


Figure 5: Progress variable fields in the triple flame, computed from the finite rate approach and from the multi-regime, the purely premixed, and the purely non-premixed flamelet models.

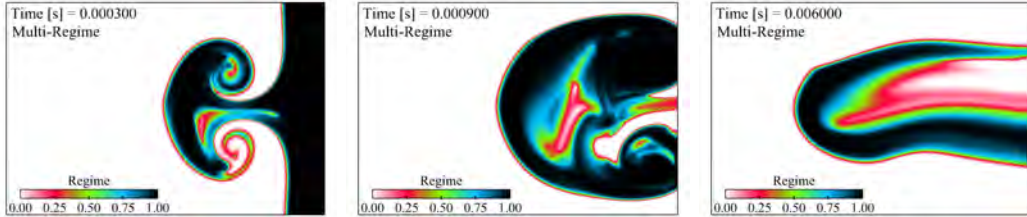


Figure 6: Regime indicator  $\xi$  from Eq. (21) in the multi-regime triple flame simulation.  $\xi = 1$  (black) denotes that premixed flamelet solutions are accessed, while  $\xi = 0$  (white) denotes that non-premixed flamelet solutions are accessed.

### Edge Speed Comparison

The influence of the combustion regime can be analyzed in more detail by considering the

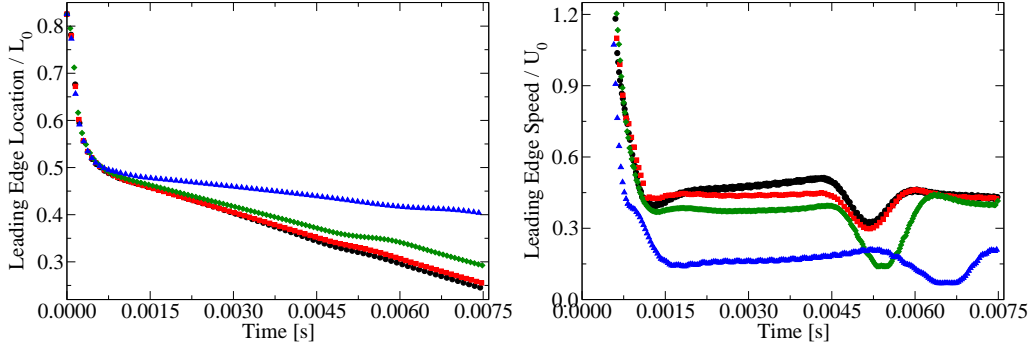


Figure 7: Position and speed of the leading flame edge in the triple flame from: finite rate chemistry (black  $\bullet$ ); multi-regime model (red  $\blacksquare$ ); premixed model only (green  $\blacklozenge$ ); non-premixed model only (blue  $\blacktriangle$ ). The position of the leading flame edge is normalized by the length of the computational domain,  $L_0$ .

position and the speed of the leading flame edge. These quantities are plotted in Fig. 7 for each of the triple flame cases. The leading flame edge location is defined as the horizontal coordinate in the computational domain where the progress variable field first reaches a value of  $C=0.08$ . This leading edge is largely premixed in nature, as described by both the multi-regime model and the flame index. Consequently, the multi-regime and premixed models describe the evolution of the leading edge more accurately than the non-premixed model. The non-premixed model's tendency is to under-predict the true flame speed.

Figure 8 shows a sampling of the conditional source term values that are responsible for the flame propagation speeds in Fig. 7. Note that the premixed and multi-regime source terms are taken from stored premixed flamelets, but are dependent on the level set as described in [14]. The non-premixed model's under-prediction of the flame edge speed is due to the under-predicted source terms shown in Fig. 8. The largest source terms in the flame are found around a mixture fraction of  $Z=0.075$ , and the non-premixed sources under-predict the finite rate sources at this mixture fraction. The linear region of the non-premixed source term profile, located between  $C=0.0$  and  $C=0.16$  in the top two plots of Fig. 8, describes the interpolated non-premixed flamelet space that sits between the unburned mixing line and the burning flamelet with the lowest maximum temperature.

At a much richer mixture fraction of  $Z=0.14$ , Fig. 8 demonstrates that the non-premixed model alters its relative behavior and over-predicts the finite rate source term. Because sources at rich  $Z$  values are relatively small, however, this over-prediction does not significantly influence flame propagation in the non-premixed model. Just as at the leaner mixture fractions, source terms along the  $Z=0.14$  surface are most accurately described by the multi-regime and premixed models.

A final noteworthy feature of the edge speed plot in Fig. 7 is the slight difference that exists between the premixed and the multi-regime predictions. This difference is not due to the progress variable source term that is used for modeling, since Fig. 8 demonstrates that the premixed and multi-regime sources are virtually identical. The difference is instead a product of how premixed flamelet solutions are extrapolated beyond their flammability

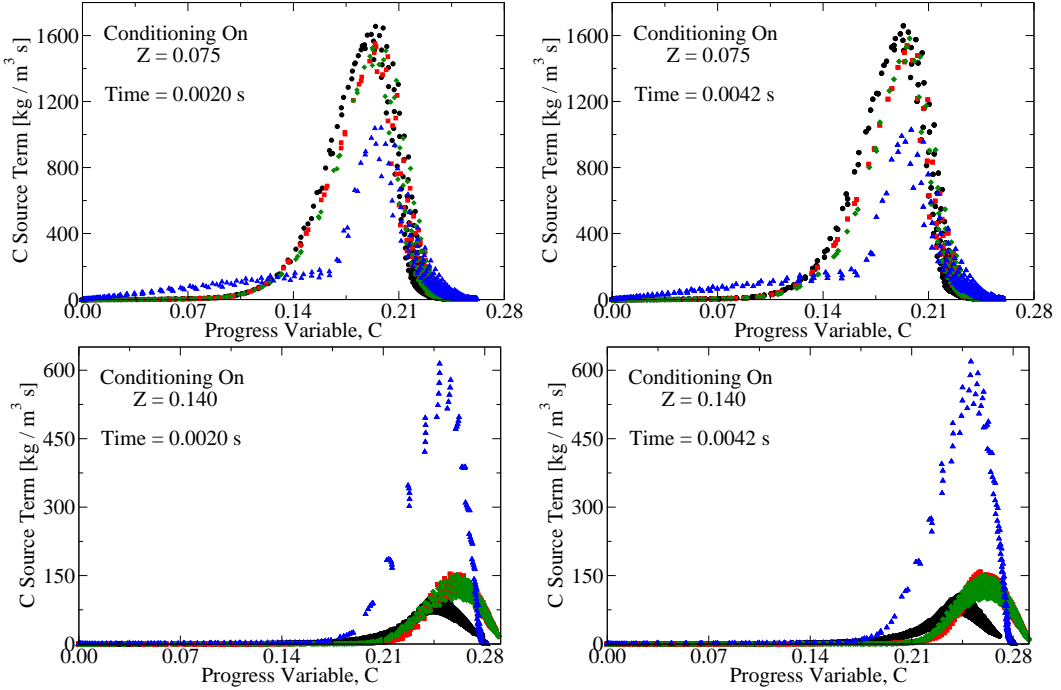


Figure 8: Conditional progress variable source terms in the triple flame, from: finite rate chemistry simulation (black  $\bullet$ ); multi-regime model (red  $\blacksquare$ ); premixed model only (green  $\blacklozenge$ ); non-premixed model only (blue  $\blacktriangle$ ).

limits. Figure 9 shows typical density fields in the finite rate, multi-regime, and premixed simulations. In these density fields fuel-rich, unburned gas is seen to flow around the rich (lower) edge of the triple flame. As shown on the right in Fig. 4, the mixture fraction associated with this rich, unburned gas is  $Z=0.5$ . This  $Z$  value lies outside the premixed flammability limits, and the density at  $(Z=0.5, C=0.0)$  in the premixed model is therefore calculated by linearly interpolating between the unburned density at the rich flammability limit and the density at a mixture fraction of unity. Because density actually varies non-linearly between  $Z=0$  and  $Z=1$ , this interpolation introduces an error. The error is evident when the premixed density plot in Fig. 9 is compared to the finite rate density plot. The premixed model's over-prediction of density affects the deflection of velocity streamlines, and consequently slows down the leading edge speed. Density in the premixed model could of course be corrected using a different extrapolation procedure, but some ambiguity would nevertheless remain.

#### Flame Structure Comparison

Plots showing the evolution of the CO species in the triple flame simulations are provided in Fig. 10. Just as in the progress variable plots, some model dependencies appear during the transient flame development phase shown in the middle column. For example, a strip of high CO concentration is seen along the simulation centerline at the right edge of the domain

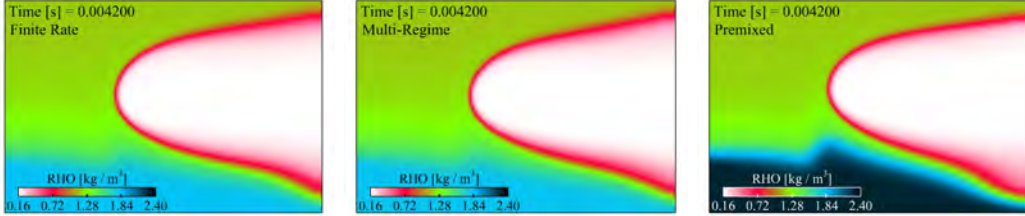


Figure 9: Density fields in the triple flame simulations, computed from the finite rate approach (left) and from the multi-regime (center) and purely premixed (right) models.

in the finite rate simulation. This high CO concentration is reproduced by the multi-regime model, but is absent in both the purely premixed and the purely non-premixed results. Further dependencies appear in the third column of Fig. 10, especially on the fuel-rich (lower) side of the triple flame. At this later time the multi-regime and premixed models again reasonably reproduce the finite rate case, with the exception of an over-prediction of CO in the rich trailing flame edge. Conversely, the non-premixed model under-predicts CO throughout the rich side of the flame.

Conditional species and temperature data from two different mixture fraction values are plotted in Figs. 11 – 12. Unlike the progress variable source terms, species and temperature data are only a mild function of the regime at  $Z=0.075$ . Fig. 11 shows that the non-premixed model somewhat under-predicts the conversion of CO to  $\text{CO}_2$ , and also slightly under-predicts the OH concentration at low progress variable. Although these differences are small, the premixed and multi-regime models agree more closely with the finite rate case than does the non-premixed model.

Conditional data from the richer mixture fraction  $Z=0.14$  is plotted in Fig. 12. Here the comparisons are more interesting, and the species' dependence on the local combustion regime is more significant. At first glance, the finite rate CO profile in Fig. 12 appears to be most accurately predicted by the purely non-premixed model. For example, at intermediate  $C$  values the overlapping multi-regime and premixed results deviate from the finite rate case much more than the non-premixed model results.

An incorrectly predicted regime does not explain the entirety of Fig. 12, however. Three observations suggest that the errors in the multi-regime CO predictions are due to more than just the regime indicator. First, the non-premixed model is seen to over-predict CO oxidation in the burned gas. This over-prediction is indicated by the sharp downturn in the non-premixed CO profile in Fig. 12 around  $C=0.22$ . Second, the lower half of Fig. 12 demonstrates that the non-premixed model does not predict temperature or OH any more accurately than the premixed model. Third, the upper right plot of Fig. 1 shows that, at the mixture fraction  $Z=0.14$  considered in Fig. 12, the lowest CO value that can be found in a non-premixed burning flamelet is  $Y_{\text{CO}} = 0.06$ . Consequently, between progress variable values of  $C=0.0$  (where  $Y_{\text{CO}} = 0.0$ ) and  $C=0.15$  (where  $Y_{\text{CO}} = 0.06$ ), the non-premixed CO profile in Fig. 12 is the result of a simple linear interpolation. The non-premixed model's agreement with finite rate chemistry in this region is consequently due less to physical

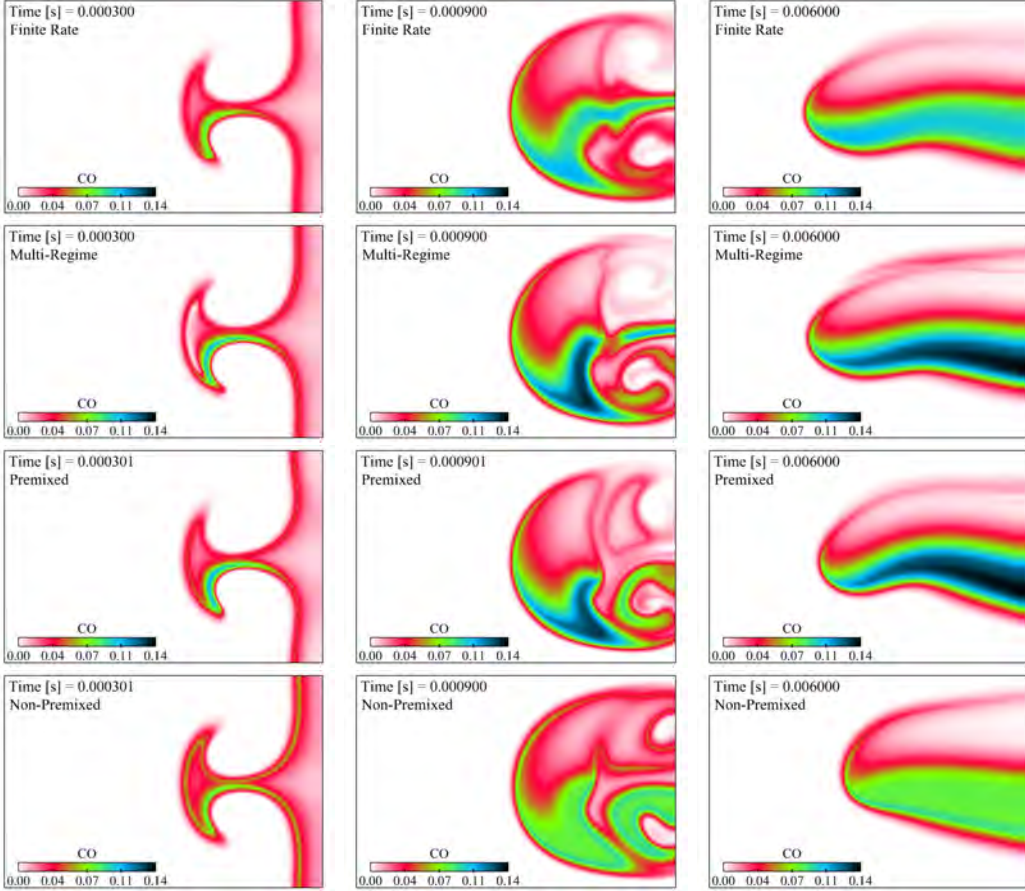


Figure 10:  $Y_{CO}$  fields in the triple flame, computed from the finite rate approach and from the multi-regime, premixed, and non-premixed flamelet models.

modeling accuracy than to numerical good fortune.

Therefore, while the CO profile in Fig. 12 does suggest that the regime is not fully premixed, the finite rate data could neither be reproduced by a fully non-premixed model. It appears, then, that chemistry on the fuel-rich side of the flame deviates from 1-D flamelet manifolds. Heat diffusion across mixture fraction surfaces is one possible source of these deviations. If a fuel-rich leading edge of the triple flame were premixed, for example, heat diffusion from an adjacent and higher temperature premixed reaction zone might cause the local temperature to rise above the relevant 1-D premixed flamelet temperature. This kind of behavior is indeed observed in the temperature plot in Fig. 12. Accounting for higher order flame structure effects [22] such as the diffusion processes associated with stratified flame propagation might improve the finite rate and multi-regime model agreement.

When comparing flame structure, it should be emphasized that the non-premixed regime must be included in the model formulation to obtain the best agreement with the finite rate

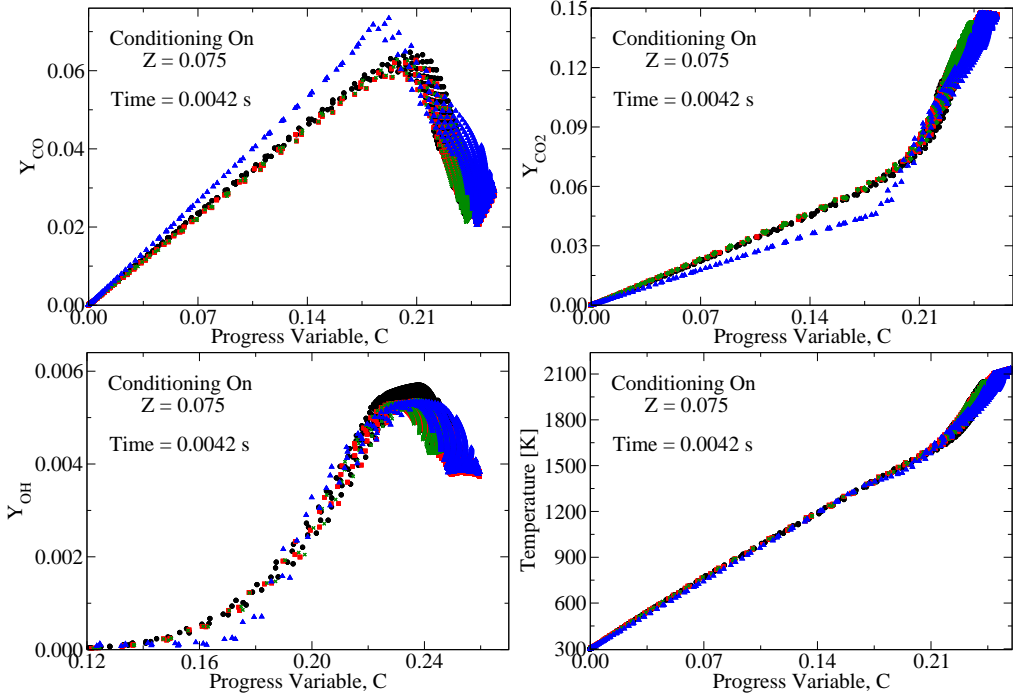


Figure 11: Flame structure profiles in the triple flame conditioned on  $Z=0.075$  from: finite rate chemistry (black  $\bullet$ ); multi-regime model (red  $\blacksquare$ ); premixed model only (green  $\blacklozenge$ ); non-premixed model only (blue  $\blacktriangle$ ).

simulation. This was first demonstrated in the more accurate flame edge speed predictions of the multi-regime model relative to the purely premixed model. It was also demonstrated by the multi-regime model's ability to most accurately represent many of the finite rate flame structures that appear during flame transients, as shown in the middle column of Fig. 5.

#### NO Comparison

Figure 13 shows the evolution of the NO species in the triple flame simulations. Again, the finite rate simulation is shown in the first row, followed by the various flamelet models. The third column of Fig 13 shows that while the premixed model comes close, none of the flamelet models predict as much NO production as the finite rate simulation. This is consistent with the presence of strain and stratification within the triple flame, and with the observation that the finite rate flame temperatures were slightly higher than the premixed flamelet model temperatures. To further investigate the regime dependency of NO production, conditional plots of both NO and the production rate of NO are shown in Fig. 14.

The data on the left side of Fig. 14 is taken at an early time in the simulation, while the data on the right side is taken at the later time associated with the third column of Fig. 13. The  $Z=0.075$  surface that is used for conditioning is very near to the mixture

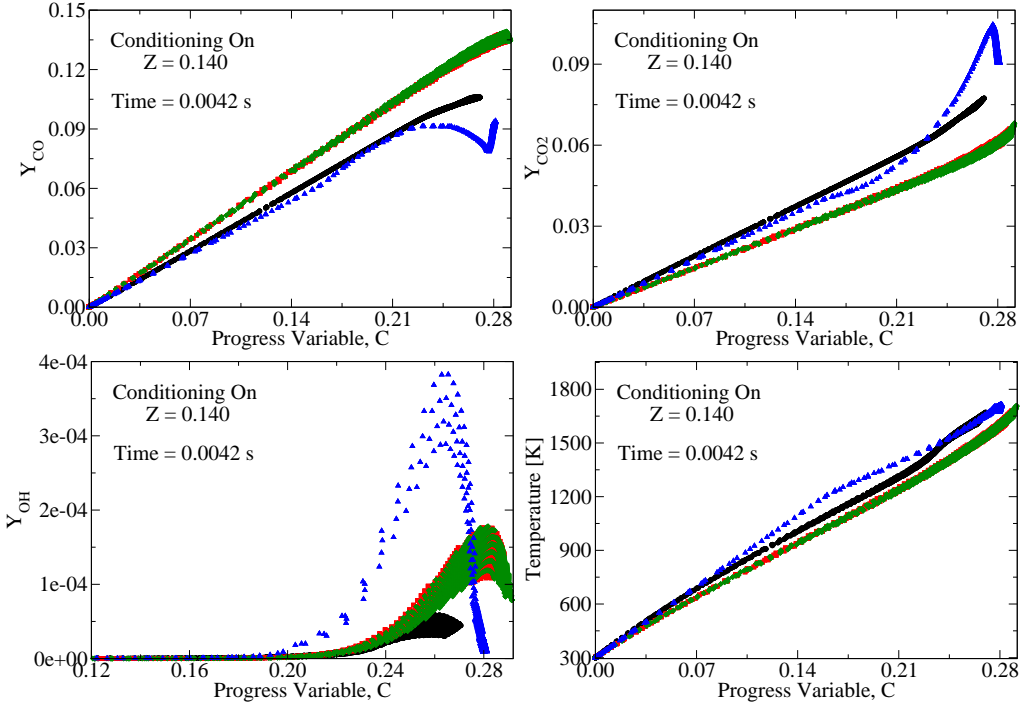


Figure 12: Flame structure profiles in the triple flame conditioned on  $Z=0.140$  from: finite rate chemistry (black  $\bullet$ ); multi-regime model (red  $\blacksquare$ ); premixed model only (green  $\blacklozenge$ ); non-premixed model only (blue  $\blacktriangle$ ).

fraction value at which NO production reaches its maximum. Although many of the multi-regime flamelet predictions up to this point have closely corresponded to the premixed flamelet predictions, Fig. 14 indicates that the opposite situation occurs with NO. The multi-regime predictions closely match those of the non-premixed flamelet model because NO forms over relatively long time scales, and the regime indicators in Fig. 6 show that regions far downstream of the flame front are predicted to be non-premixed. Interestingly, these regime observations have little practical consequence for the triple flame, since the NO production rate does not significantly vary between regimes. The similarity of these NO production rates is consistent with the underlying flamelet solutions: the non-premixed NO production rate shown in Fig. 1 and the premixed NO production rate shown in Fig. 2 both reached maximums of approximately  $0.005 \text{ kg} / \text{m}^3 \text{ s}$ . Note, however, that NO production is strongly a function of scalar dissipation rate (see Fig. 1), and in general NO production may differ significantly across combustion regimes.

### 2.3.3 Summary

Within the context of the flamelet modeling approach, an increasing need exists for models and validation data that are relevant to multi-regime combustion processes. Sections 2.2 and 2.3 of this report attempt to address a part of that need by considering 1) whether

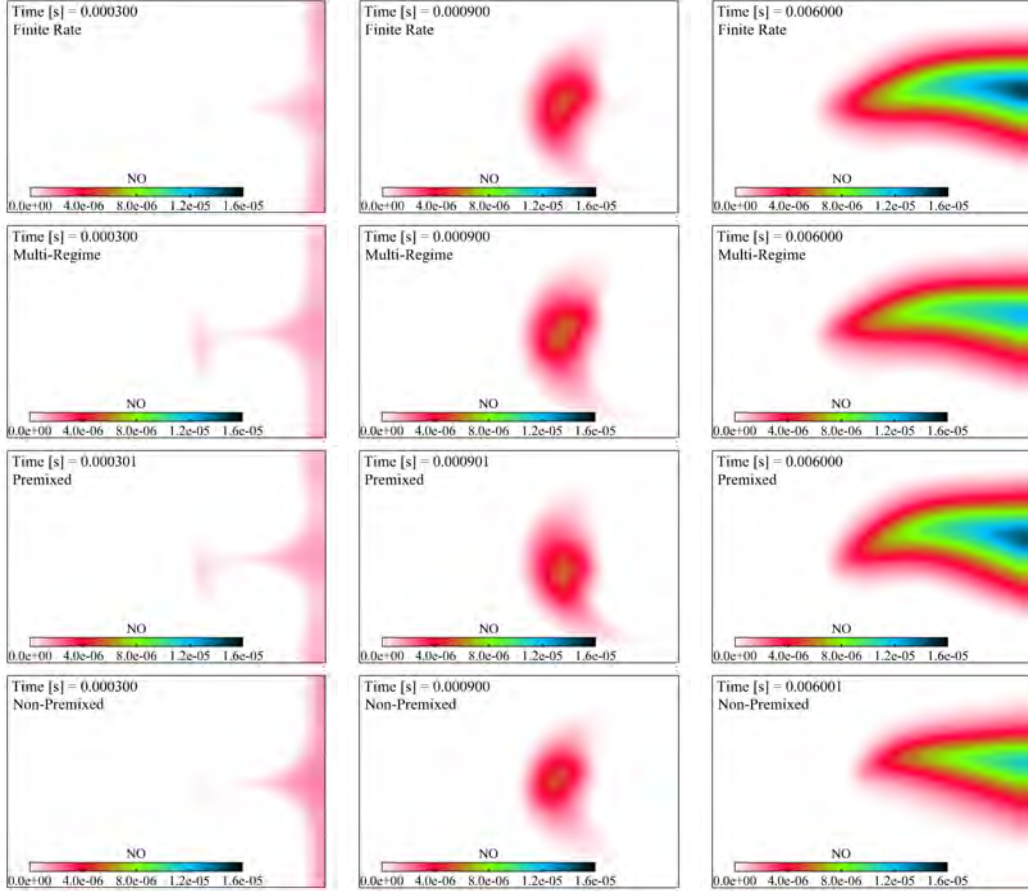


Figure 13: NO fields in the triple flame, computed from the finite rate approach and from the purely non-premixed, the purely premixed, and the multi-regime flamelet models.

a mixed regime flamelet approach can capture combustion and pollutant formation in a detailed chemistry, multi-dimensional environment, and 2) whether the errors associated with the flamelet model are attributable to incorrect regime descriptions, or to problems with the underlying single-regime flamelet assumptions.

To address these issues, simulations of a primarily premixed triple flame were performed using finite rate chemistry and a variety of flamelet combustion models. It was demonstrated that a multi-regime flamelet approach could capture the correct asymptotic combustion regime in the flame. Further details of this study can be found in references [19] and [4], which were supported by this project.

Although the multi-regime approach correctly identified combustion regimes, several of the corresponding flamelet model predictions nonetheless deviated from the finite rate data. These deviations are most likely due to strain and stratification. In the flamelet modeling context, these deviations can only be accounted for by expanding the parameters used to

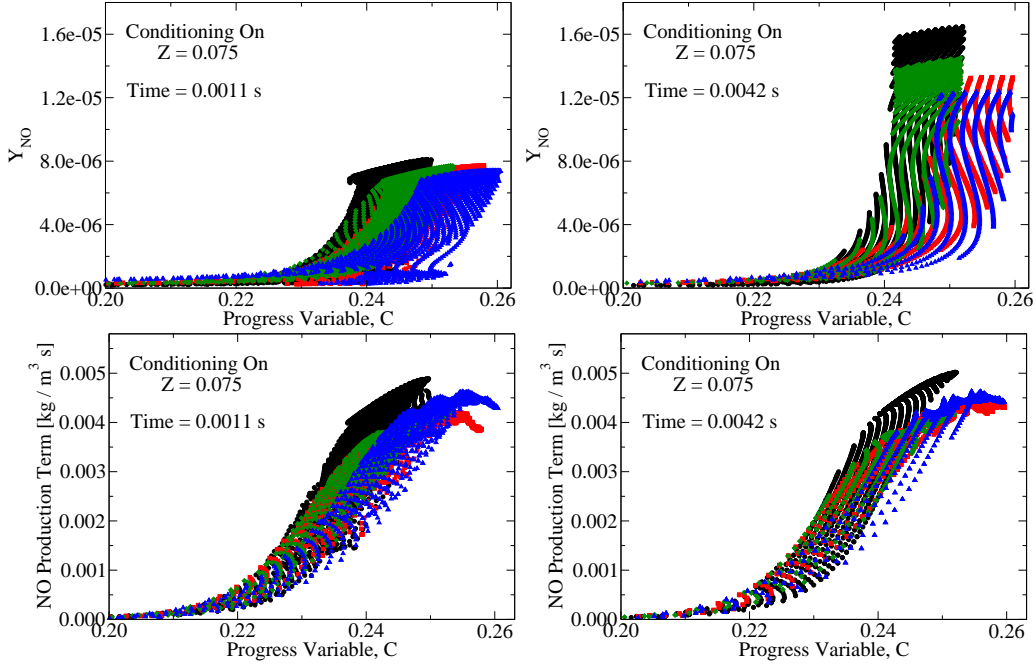


Figure 14: NO and NO production source term profiles in the triple flame conditioned on  $Z=0.075$ , and at two different times: finite rate chemistry (black  $\bullet$ ); multi-regime model (red  $\blacksquare$ ); premixed model only (green  $\blacklozenge$ ); non-premixed model only (blue  $\blacktriangle$ ).

describe chemistry. In spite of these modeling limitations, the multi-regime approach was shown to accurately distinguish between the premixed and non-premixed asymptotes. When the triple flame and the counterflow flame are considered as a single modeling challenge, the advantage of the multi-regime model is that it can be applied to both cases without the need for case-related mixing assumptions. The ability to apply a single model that dynamically accounts for regime information led to significantly improved accuracy relative to the single regime approaches.

## 2.4 Modeling Sub-Filter Scalar Dissipation In Turbulent Non-Premixed Flames

### 2.4.1 Motivation

Scalar dissipation rates and sub-filter scalar variances are critical modeling parameters in large eddy simulations (LES) of reacting flows. A variety of models for these quantities have been proposed, many having been designed to operate within a Reynolds averaged framework. Dissipation rate and variance models can be categorized according to whether they are based on an algebraic equation or a transport equation. Algebraic models for the variance [23, 24, 25, 26, 27] and the dissipation rate [23, 28, 29] directly describe the modeled parameter using information about the local scalar field and filter width, and have

the advantage of being conceptually simple and computationally inexpensive. Transport equation models for the variance [27, 30, 31] and for the dissipation rate [32, 33, 34] offer different advantages: they do not forcibly assume that production and dissipation processes are in equilibrium, they produce fields that are less noisy than algebraic models, and they incorporate a wider range of physics. Nonetheless, transport equation approaches are sensitive to the descriptions used to model unclosed sub-filter terms, and the performance of these equations is not always superior to the performance of algebraic models [27]. For example, the closure of these transport equations may be strongly affected by the details and accuracy of the numerical method that is used. Consequently, many uncertainties continue to surround the modeling of scalar variance and dissipation.

Two observations regarding the sub-filter dissipation motivate this section. First, improvements in variance and dissipation rate LES models are expected to significantly improve the quality of reactive flow predictions. Second, significant ambiguity exists regarding how these improvements should be pursued. The goal of this work is to further address these modeling needs by making use of newly available reacting direct numerical simulation data, and by proposing a new LES closure model.

#### 2.4.2 Modeling Background

The scalar dissipation rate  $\chi_Z$  of a scalar  $Z$  whose diffusivity is  $\mathcal{D}_Z$  can be written

$$\chi_Z = 2 \mathcal{D}_Z |\nabla Z|^2. \quad (23)$$

When an LES filter is applied to this quantity, the filtered dissipation rate is found,

$$\bar{\chi}_Z = 2 \overline{\mathcal{D}_Z} |\nabla \bar{Z}|^2, \quad (24)$$

where the  $(\bar{\cdot})$  operator denotes spatial filtering. The sub-filter scalar variance is typically calculated using density weighted filtering that will be denoted by the tilde operator  $(\tilde{\cdot})$ . This sub-filter variance is

$$\widetilde{Z''_{sfs}} = \widetilde{Z^2} - (\widetilde{Z})^2. \quad (25)$$

##### *Algebraic Models*

Algebraic LES models for  $\bar{\chi}_Z$  can be formulated using a variety of parameters [29]. The simplest and most widely used formulation separates the dissipation rate into resolved and sub-filter components [28],

$$\bar{\chi}_Z = 2 (\overline{\mathcal{D}}_Z + \mathcal{D}_t) |\nabla \widetilde{Z}|^2, \quad (26)$$

where the filtered molecular diffusivity  $\overline{\mathcal{D}}_Z$  is associated with the resolved dissipation, and the turbulent diffusivity  $\mathcal{D}_t$  is associated with the sub-filter dissipation. This model introduces no unknown coefficients, as the turbulent diffusivity is already available from the solution of the underlying scalar's transport equation.

Algebraic LES models for the sub-filter scalar variance can also take many forms [24, 25, 26]. The most widely used form relates the variance to gradients of the resolved scalar field,

$$\widetilde{Z''_{sfs}} = C_{var} \Delta^2 |\nabla \widetilde{Z}|^2. \quad (27)$$

The  $\Delta$  parameter in Eq. (27) is the LES filter width. This model introduces a unique coefficient that can also be dynamically calculated using a variety of methods [10, 26].

### Transport Equation Models

An exact transport equation can be written for the scalar dissipation rate. Similarly, the scalar variance can be described exactly using the solution of either a variance equation or transport equations for both  $Z$  and  $Z^2$ . In the context of LES, several of the terms that appear in the equations for these quantities require closure models. Here, exact equations for the dissipation rate and the square of a scalar ( $Z^2$ ) are introduced first.

In reacting flows, the transport equation for  $\chi_Z$  includes terms that depend on gradients of diffusivity and density. When this equation is solved in LES, these terms all require closure. To limit the appearance of unclosed terms, a transport equation for  $|\nabla Z|^2$ , rather than for  $\chi_Z$ , is considered. Letting  $D/Dt$  denote the material derivative, this equation is

$$\begin{aligned} \frac{D}{Dt} (\rho |\nabla Z|^2) &= \frac{\partial}{\partial x_j} \left( \rho \mathcal{D}_Z \frac{\partial}{\partial x_j} (|\nabla Z|^2) \right) & (28) \\ &\quad - 2\rho \left( \frac{\partial u_i}{\partial x_j} \frac{\partial Z}{\partial x_i} \frac{\partial Z}{\partial x_j} \right) & (a) \\ &\quad - 2\rho \mathcal{D}_Z \left( \frac{\partial^2 Z}{\partial x_i \partial x_j} \right)^2 & (b) \\ &\quad - \frac{2}{\rho} \frac{\partial \rho}{\partial x_i} \frac{\partial Z}{\partial x_i} \left( \frac{\partial}{\partial x_j} \left( \rho \mathcal{D}_Z \frac{\partial Z}{\partial x_j} \right) \right) & (c) \\ &\quad + 2 \frac{\partial(\rho \mathcal{D}_Z)}{\partial x_i} \frac{\partial Z}{\partial x_i} \left( \frac{\partial^2 Z}{\partial x_j \partial x_j} \right) & (d) \\ &\quad + 2 \frac{\partial Z}{\partial x_i} \frac{\partial Z}{\partial x_j} \left( \frac{\partial^2(\rho \mathcal{D}_Z)}{\partial x_i \partial x_j} \right). & (e) \end{aligned}$$

The (a) and (b) terms in Eq. (28) describe the production and dissipation, respectively, of the scalar dissipation rate. The (c) through (e) terms describe the effects of changes in density and diffusivity, and reduce to zero when  $\rho$  and  $\mathcal{D}_Z$  are constant. Once solved, the  $|\nabla Z|^2$  quantity from Eq. (28) can be multiplied with  $\mathcal{D}_Z$  to determine  $\chi_Z$ .

Applying an LES density weighted filter to Eq. (28) results in a transport equation for the term  $\widetilde{|\nabla Z|^2}$ . It will be assumed that correlations between mixture fraction gradients and the scalar diffusivity are small, so that the transported quantity can be multiplied with the filtered diffusivity to compute the dissipation rate,

$$2 \mathcal{D}_Z |\nabla Z|^2 \approx 2 \widetilde{\mathcal{D}}_Z \widetilde{|\nabla Z|^2}. \quad (29)$$

*A priori* tests have suggested that the density weighting which differentiates the filtering of  $\widetilde{|\nabla Z|^2}$  and  $\widetilde{|\nabla Z|^2}$  can be neglected on the grounds that it has a relatively small influence [35].

After filtering, the equation for the quantity  $\widetilde{|\nabla Z|^2}$  becomes,

$$\begin{aligned} \frac{D}{Dt} \left( \bar{\rho} \widetilde{|\nabla Z|^2} \right) &= \frac{\partial}{\partial x_j} \left( \bar{\rho} (\tilde{\mathcal{D}}_Z + D_t) \frac{\partial}{\partial x_j} (\widetilde{|\nabla Z|^2}) \right) & (30) \\ &\quad - 2 \overline{\rho \left( \frac{\partial u_i}{\partial x_j} \frac{\partial Z}{\partial x_i} \frac{\partial Z}{\partial x_j} \right)} & (a) \\ &\quad - 2 \overline{\rho \mathcal{D}_Z \left( \frac{\partial^2 Z}{\partial x_i \partial x_j} \right)^2} & (b) \\ &\quad - \frac{2}{\rho} \overline{\frac{\partial \rho}{\partial x_i} \frac{\partial Z}{\partial x_i} \left( \frac{\partial}{\partial x_j} \left( \rho \mathcal{D}_Z \frac{\partial Z}{\partial x_j} \right) \right)} & (c) \\ &\quad + 2 \overline{\frac{\partial(\rho \mathcal{D}_Z)}{\partial x_i} \frac{\partial Z}{\partial x_i} \left( \frac{\partial^2 Z}{\partial x_j \partial x_j} \right)} & (d) \\ &\quad + 2 \overline{\frac{\partial Z}{\partial x_i} \frac{\partial Z}{\partial x_j} \left( \frac{\partial^2(\rho \mathcal{D}_Z)}{\partial x_i \partial x_j} \right)}, & (e) \end{aligned}$$

where a standard turbulent diffusivity model has been invoked to describe sub-filter scalar flux. The (a) through (e) terms in Eq. (30) are unclosed. Sanders *et al.* [34] provides a review of the relevant closure modeling for Reynolds averaged approaches. In LES, different closures are needed. This issue will be further addressed in section 2.4.5.

The sub-filter scalar variance can be solved for in a number of different ways. Based on Kaul *et al.*'s observations [27], a transport equation for  $Z^2$  will be used here. After LES filtering, this transport equation is written

$$\frac{D}{Dt} \left( \bar{\rho} \widetilde{Z^2} \right) = \frac{\partial}{\partial x_j} \left( \bar{\rho} (\tilde{\mathcal{D}}_Z + D_t) \frac{\partial}{\partial x_j} (\widetilde{Z^2}) \right) - \bar{\rho} \widetilde{\chi}_Z. \quad (31)$$

Equation (31) is noteworthy in that it does not add to the closure modeling problem. Rather, if the scalar dissipation rate  $\widetilde{\chi}_Z$  has been closed, then Eq. (31) is closed. Once solved, Eq. (31) can be used to calculate the sub-filter variance  $\widetilde{Z''^2}_{sfs}$  using Eq. (25).

### 2.4.3 Auto-Igniting Jet

#### DNS Description

The DNS case that will be used to assess the dissipation and variance models is an auto-igniting slot jet. This ethylene fueled flame was originally the subject of a DNS study by Yoo *et al.* [36]. A schematic of the flame is shown in Fig. 15, where velocity contours are plotted on the left and temperature contours are plotted on the right. The central fuel jet has a bulk velocity of 220 m/s, a temperature of 550 K, and a composition of 82% N<sub>2</sub> and 18% C<sub>2</sub>H<sub>4</sub> by volume. This central jet stream is denoted by the mixture fraction composition  $Z = 1$ . The co-flow that surrounds the central jet consists of 100% air at a temperature of 1550 K. The air co-flow enters the domain at a bulk velocity of 20 m/s, and

this air stream is denoted by a mixture fraction of  $Z = 0$ . No nozzle separates the main jet and co-flow; rather, the velocity, temperature, and composition profiles are prescribed to smoothly transition between  $Z = 0$  and  $Z = 1$  according to the functions listed in reference [36]. The total width of the central jet is  $H = 0.002$  m, and the jet Reynolds number associated with the DNS conditions is 10,000.

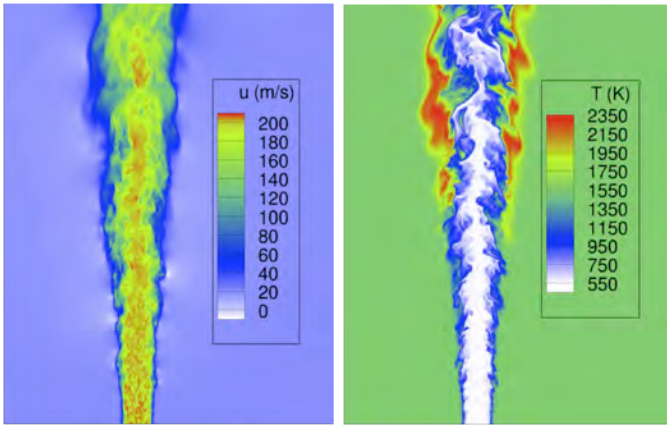


Figure 15: The ethylene flame DNS. Left: axial velocity contours; Right: temperature contours.

Chemistry in the flame is described using a 22 species ethlyene mechanism [36] that was reduced from a larger hydrocarbon mechanism. This same 22 species mechanism is used in all modeled LES calculations.

#### LES Description

In all LES simulations of the jet DNS, combustion is described using an unsteady flamelet approach similar to that of Ihme and See [37] and Pitsch [38]. The model is implemented by solving the unsteady

flamelet equations [1, 12]. Unsteady flamelet solutions are generated for a variety of reference scalar dissipation rates. They are then tabulated as a function of  $Z$ ,  $\chi_{Z,\text{ref}}$ , and the progress variable  $C$ .

Once generated, the unsteady solutions are convoluted with presumed PDFs for application in the LES. A beta PDF is presumed to describe  $Z$ , while a delta PDF is presumed to describe  $\chi_{Z,\text{ref}}$ . Additionally, it is assumed that a single unsteady flamelet solution is representative of the conditions in an LES mesh cell. Consequently, only the mean value of the progress variable is needed for modeling [10]. These assumptions lead to a tabulated LES chemistry database of the form

$$\tilde{\phi}_k = \tilde{\phi}_k(\tilde{Z}, \tilde{Z''^2}, \chi_{Z,\text{ref}}, \tilde{C}), \quad (32)$$

where  $\phi_k$  is any reacting quantity of interest. The reference dissipation rate can be determined from the local unconditional LES dissipation rate  $\bar{\chi}_Z$  by filtering Eq. (3),

$$\chi_{Z,\text{ref}} = \bar{\chi}_Z \cdot \frac{f(Z_{\text{ref}})}{\bar{f}(Z)}, \quad (33)$$

where  $\bar{f}(Z)$  is determined by convoluting the function  $f(Z)$  with a beta PDF.

Filtered  $C$  and  $Z$  scalars are transported in the LES, and the scalar dissipation rate and sub-filter variance are calculated using models from section 2.4.2. The tabulated chemistry database from Eq. (32) is accessed during the LES to determine chemical information such as the density and the progress variable source term.

Two LES runs are performed using different mesh resolutions. The first mesh consists of 1 million (1M) cells, and corresponds to an LES filter width to Kolmogorov scale ratio of approximately  $\Delta/\eta = 8$ . The second LES mesh consists of 23 million (23M) cells, and the corresponding length scale ratio is  $\Delta/\eta = 4.5$ . The DNS data is filtered for comparison with LES using coarse and fine filter widths that correspond to the 1 million cell and 23 million cell LES meshes, respectively.

#### 2.4.4 Algebraic Model Performance

Figure 16 presents fields from the 1 million cell and 23 million cell LES runs alongside DNS fields that are filtered using the  $\Delta$  from the 1 million cell LES. The filtered mixture fraction is plotted along with the algebraically modeled dissipation rate from Eq. (26) and the algebraically modeled sub-filter scalar variance from Eq. (27). The  $\tilde{Z}$  field in the higher resolution LES is seen to capture significantly more flow structure than the lower resolution LES. Consequently, the burden on the sub-filter models is eased in the higher resolution data set. The 1 million cell LES is therefore viewed as the primary sub-filter modeling challenge.

Figure 17 compares the algebraically modeled scalar dissipation rate from Eq. (26) with the filtered dissipation rate from the DNS. All quantities are time averaged, as represented by the  $\langle \cdot \rangle$  operator. Figure 17(a) shows  $\bar{\chi}_Z$  as a function of the cross-stream coordinate at various downstream planes, while Fig. 17(b) shows the mixture fraction conditioned  $\bar{\chi}_Z$  in those same planes. The algebraic model's representation of  $\bar{\chi}_Z$  is shown to be poor, especially in the lower

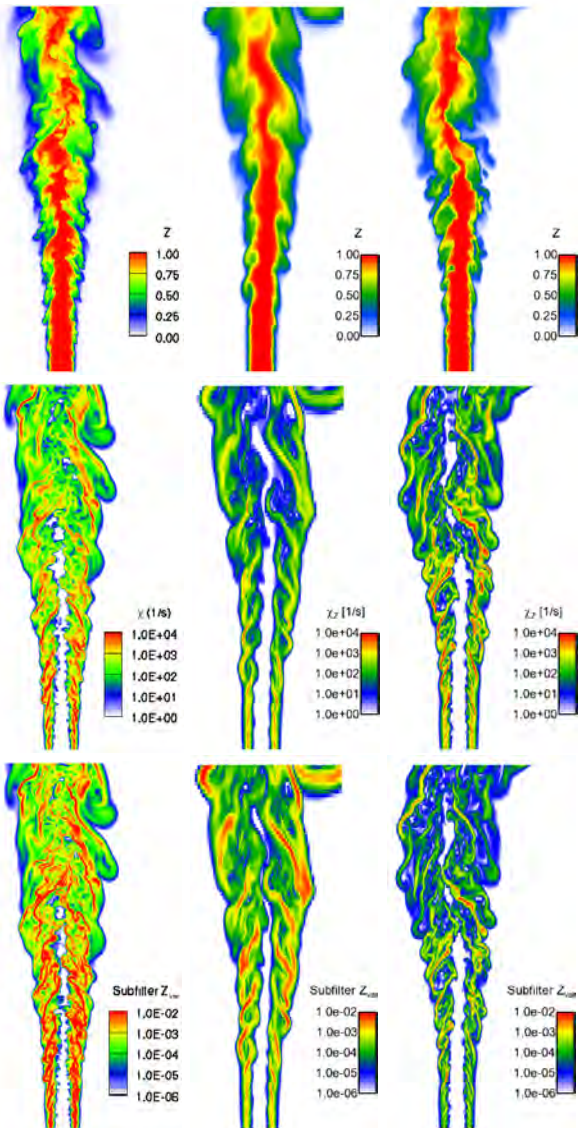


Figure 16: LES algebraic model results. Left column: DNS fields filtered using the 1 million cell LES filter width; Middle column: 1 million cell LES; Right column: 23 million cell LES. Upper row:  $\tilde{Z}$  contours; Middle row:  $\bar{\chi}_Z$  from Eq. (26); Lower row:  $\tilde{Z}_{sfs}''^2$  from Eq. (27).

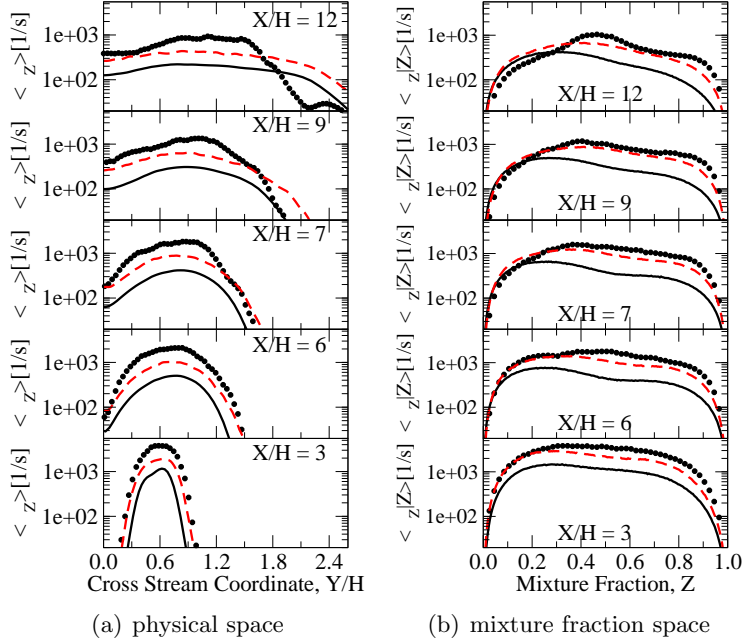


Figure 17: Algebraic  $\bar{\chi}_Z$  model results in the reacting jet, plotted in both physical (a) and conditional (b) space. DNS (●●●); 1 million cell LES (—); 23 million cell LES (— —).

resolution case. At both LES resolutions, the model under-predicts  $\bar{\chi}_Z$  from the DNS. In the lower resolution case in particular, the under-predictions are order-of-magnitude differences. Because ignition is sensitive to local dissipation, these errors lead to significant under-predictions of the flame lift-off height. Although the  $\bar{\chi}_Z$  predictions are improved when the LES resolution is increased, differences between the high and low resolution LES indicate that the algebraic model is undesirably sensitive to the filter size.

Resolved and sub-filter contributions to the LES algebraic  $\bar{\chi}_Z$  model are separated and compared with the DNS in Fig. 18. Both LES filter widths are considered. The resolved component of dissipation is calculated as  $\langle 2\bar{\mathcal{D}}_Z |\nabla \tilde{Z}|^2 \rangle$  in both the filtered DNS and LES, while the sub-filter component is calculated as  $\langle 2\mathcal{D}_Z |\nabla Z|^2 - 2\bar{\mathcal{D}}_Z |\nabla \tilde{Z}|^2 \rangle$  and  $\langle 2\mathcal{D}_t |\nabla \tilde{Z}|^2 \rangle$  in the DNS and LES, respectively. Figure 18(a) plots the dissipation rate components that are associated with the coarse filter width. At this filter resolution, the resolved dissipation from the filtered DNS (solid black circles) and sub-filter dissipation from the filtered DNS (open blue circles) are comparable in magnitude. sub-filter dissipation modeling therefore plays an important role in the 1 million cell LES, even though the Reynolds number of the case is not representative of realistic combustor conditions. The resolved DNS dissipation rate is reasonably well described by the resolved component of the LES model (black solid line), at least in the rich part of the flame where turbulence is most intense. The sub-filter LES dissipation (blue dashed line), however, universally underestimates the sub-filter

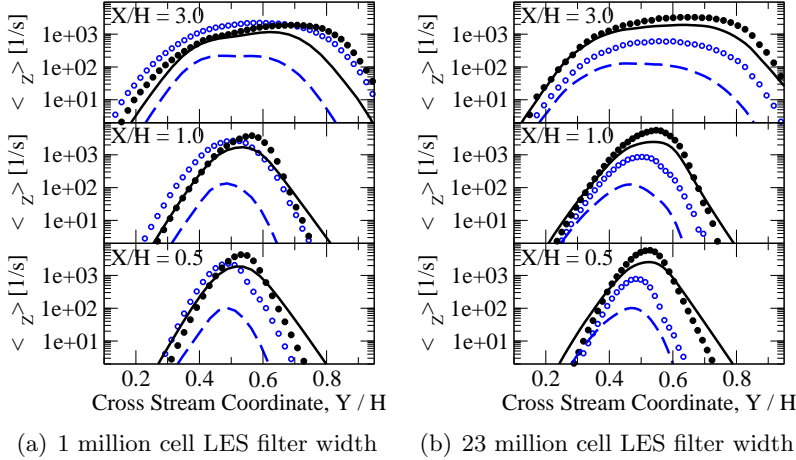


Figure 18: Budget of the algebraic  $\bar{\chi}_Z$  model in the reacting jet. Resolved dissipation from the filtered DNS (●●●); resolved dissipation from the algebraic LES model (—); sub-filter dissipation from the filtered DNS (○○○); sub-filter dissipation from the algebraic LES model (—). The filter resolutions correspond to the 1 million cell LES (a) and the 23 million cell LES (b).

dissipation seen in the DNS. This sub-filter modeling error is responsible for the bulk of the error in the total modeled dissipation rate.

Figure 18(b) demonstrates that the sub-filter component of the algebraic model performs poorly even when the filter width is decreased. In spite of this poor performance, the total dissipation rate is predicted more accurately (see Fig. 17). The explanation for the improvement is that the dissipation rate budget shifts from the sub-filter scales to the resolved scales. The sub-filter model therefore reduces in importance. Dissipation rate predictions in the 23 million cell LES can be said to improve relative to the 1 million cell LES predictions in spite of, and not because of, sub-filter model performance.

#### 2.4.5 An Adapted Dynamic LES Closure For The Dissipation Equation

One method of addressing the observed sub-filter dissipation errors would be to adjust the form of the algebraic model [25, 29]. Here, however, the transport equations that were shown in section 2.4.2 are considered as a means of improving the modeling. This section addresses the closure of the LES transport equation for  $\widetilde{|\nabla Z|^2}$ , shown in Eq. (30).

##### Production And Dissipation Closure Assumptions

Five unclosed terms labeled (a) through (e) appear in the dissipation rate equation, Eq. (30). The two most important of these are the production and dissipation terms. They

are split into resolved and sub-filter components for use in LES,

$$-2\bar{\rho} \overline{\left( \frac{\partial u_i}{\partial x_j} \frac{\partial Z}{\partial x_i} \frac{\partial Z}{\partial x_j} \right)} = -2\bar{\rho} \left( \frac{\partial \tilde{u}_i}{\partial x_j} \frac{\partial \tilde{Z}}{\partial x_i} \frac{\partial \tilde{Z}}{\partial x_j} \right) + \mathcal{P}_{sfs}, \quad (34)$$

$$-2\bar{\rho} \tilde{\mathcal{D}}_Z \overline{\left( \frac{\partial^2 Z}{\partial x_i \partial x_j} \right)^2} = -2\bar{\rho} \tilde{\mathcal{D}}_Z \left( \frac{\partial^2 \tilde{Z}}{\partial x_i \partial x_j} \right)^2 - \Omega_{sfs}. \quad (35)$$

Following Reynolds averaged modeling approaches such as those reviewed by Sanders [34, 39], the sub-filter production and dissipation terms will be written for LES as

$$\mathcal{P}_{sfs} = C_{prd} \cdot \bar{\rho} \cdot \left( \frac{u'_\Delta^3}{\Delta \cdot \nu_t} \right)^{1/2} \cdot \left( \widetilde{|\nabla Z|^2} - |\nabla \tilde{Z}|^2 \right), \quad (36)$$

$$\Omega_{sfs} = C_{dis} \cdot \bar{\rho} \cdot \frac{\tilde{\mathcal{D}}_Z}{\widetilde{Z''''_{sfs}^2}} \cdot \left( \widetilde{|\nabla Z|^2} - |\nabla \tilde{Z}|^2 \right)^2. \quad (37)$$

$C_{prd}$  and  $C_{dis}$  are model coefficients, and  $\widetilde{Z''''_{sfs}^2}$  is the sub-filter scalar variance that is modeled either algebraically or with a transport equation.  $\nu_t$  is the turbulent viscosity that, in the following sections, will be calculated using a dynamic Smagorinsky model with Lagrangian averaging [40]. The  $u'_\Delta^3/\Delta$  term in the production model can be viewed as the sub-filter momentum dissipation,  $\epsilon_\Delta$ . In the homogeneous DNS calculations presented next,  $u'_\Delta^3$  is locally calculated using the sub-filter kinetic energy  $k_{sfs,\Delta}$  as  $u'_\Delta = ((2/3)k_{sfs,\Delta})^{1/2}$ . In the LES calculations of the reacting jet that are shown later,  $u'_\Delta^3/\Delta$  is calculated following Deardorff [41, 42].

It will be assumed that the remaining (c) through (e) terms in Eq. (30) are of less importance on sub-filter scales, as justified in [42].

### Modeled LES Scalar Dissipation Equation

These dissipation closure assumptions lead to the following form of the  $\widetilde{|\nabla Z|^2}$  equation,

$$\begin{aligned} \frac{D}{Dt} \left( \bar{\rho} \widetilde{|\nabla Z|^2} \right) &= \frac{\partial}{\partial x_j} \left( \bar{\rho} (\tilde{\mathcal{D}}_Z + D_t) \frac{\partial}{\partial x_j} (\widetilde{|\nabla Z|^2}) \right) - 2\bar{\rho} \left( \frac{\partial \tilde{u}_i}{\partial x_j} \frac{\partial \tilde{Z}}{\partial x_i} \frac{\partial \tilde{Z}}{\partial x_j} \right) \\ &\quad - 2\bar{\rho} \tilde{\mathcal{D}}_Z \left( \frac{\partial^2 \tilde{Z}}{\partial x_i \partial x_j} \right)^2 - \frac{2}{\bar{\rho}} \frac{\partial \bar{\rho}}{\partial x_i} \frac{\partial \tilde{Z}}{\partial x_i} \left( \frac{\partial}{\partial x_j} \left( \bar{\rho} \tilde{\mathcal{D}}_Z \frac{\partial}{\partial x_j} (\tilde{Z}) \right) \right) \\ &\quad + 2 \frac{\partial (\bar{\rho} \tilde{\mathcal{D}}_Z)}{\partial x_i} \frac{\partial \tilde{Z}}{\partial x_i} \left( \frac{\partial^2 \tilde{Z}}{\partial x_j \partial x_j} \right) + 2 \frac{\partial \tilde{Z}}{\partial x_i} \frac{\partial \tilde{Z}}{\partial x_j} \left( \frac{\partial^2 (\bar{\rho} \tilde{\mathcal{D}}_Z)}{\partial x_i \partial x_j} \right) \\ &\quad + C_{prd} \cdot \bar{\rho} \cdot \frac{32 \cdot \nu_t}{\Delta^2} \cdot \left( \widetilde{|\nabla Z|^2} - |\nabla \tilde{Z}|^2 \right) - C_{dis} \cdot \bar{\rho} \cdot \frac{\tilde{\mathcal{D}}_Z}{\widetilde{Z''''_{sfs}^2}} \cdot \left( \widetilde{|\nabla Z|^2} - |\nabla \tilde{Z}|^2 \right)^2. \end{aligned} \quad (38)$$

Once closed,  $\widetilde{|\nabla Z|^2}$  from Eq. (38) can be multiplied with  $\widetilde{\mathcal{D}}_Z$  to determine  $\bar{\chi}_Z$ . This  $\bar{\chi}_Z$  value can then be used as the source term in the sub-filter variance equation, Eq. (31). The only remaining barrier to implementation of the transport equation models for the dissipation and variance is the specification of  $C_{prd}$  and  $C_{dis}$ .

### Scalar Mixing Turbulence Database

Closure models for  $C_{prd}$  and  $C_{dis}$  are especially difficult to develop because most of the dissipation rate's energetic content exists on the smallest scales of a flow. This small scale content inhibits the accuracy of traditional dynamic LES approaches for describing model coefficients, which tend to extrapolate information from large resolved scales to small unresolved scales. When the large scales contain negligible amounts of information relative to the small scales, the extrapolation procedure ceases to aid in modeling. Alternatives to the traditional dynamic algorithm are therefore needed.

The evaluation of  $C_{prd}$  and  $C_{dis}$  will be investigated using a second database of direct numerical simulations that describe conserved scalar mixing in the presence of forced, constant density, homogeneous isotropic turbulence. This second set of DNS data was originally developed in order to study the probability distribution functions that result from multi-scalar mixing [43, 44]. These DNS cases are run on a  $512^3$  computational mesh and are forced using the scheme of Rosales and Meneveau [45] to a Reynolds number of approximately  $Re_\lambda=100$ . Scalar fields are then initialized in the domain according to the procedure of Eswaran *et al.* [46]. Further details regarding the scalar mixing DNS can be found in [44].

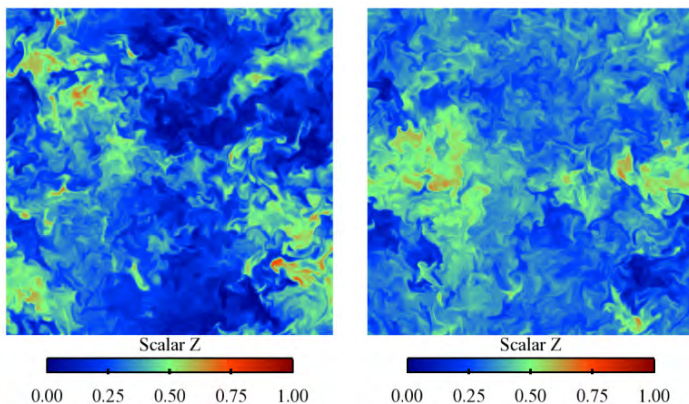


Figure 19: Typical planes from two of the the  $512^3$  scalar mixing homogeneous turbulence DNS runs [43], showing contours of the scalar.

that describe the distribution of the model coefficient  $C_{prd}$  after one eddy turnover time in the scalar mixing DNS. This coefficient is evaluated at each location in the homogeneous

Data is extracted from the homogeneous DNS for analysis at one eddy turnover time after the scalar field is initialized. Typical contour planes that show the scalar field at this point in time appear in Fig. 19. This scalar data is filtered for analysis in an LES context using clipped Gaussian filter kernels [14]. The filtering is performed using several filter widths, and model results are parameterized by these widths.

### Model Coefficient PDFs

Figure 20 shows the PDFs

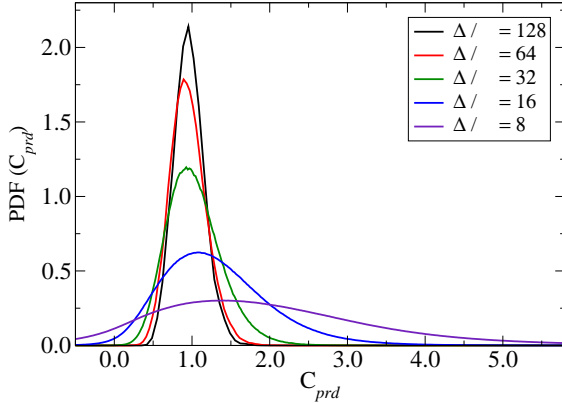


Figure 20: PDFs of the model coefficient  $C_{prd}$  from Eq. (38), evaluated from the homogeneous scalar mixing DNS. The PDFs are parameterized by the LES filter width,  $\Delta$ .

DNS domain using the formula

$$C_{prd} = \frac{-(\nu_t \Delta)^{1/2} \left[ 2\overline{\rho \frac{\partial u_j}{\partial x_i} \frac{\partial Z}{\partial x_i} \frac{\partial Z}{\partial x_j}} - 2\overline{\rho} \frac{\partial \tilde{u}}{\partial x_i} \frac{\partial \tilde{Z}}{\partial x_i} \frac{\partial \tilde{Z}}{\partial x_j} \right]}{\overline{\rho} \cdot (u'_\Delta)^{3/2} \cdot \left( \widetilde{|\nabla Z|^2} - |\nabla \tilde{Z}|^2 \right)}. \quad (39)$$

PDFs of the coefficient are constructed for a given filter size by binning results from the entire domain.

Figure 20 shows that the  $C_{prd}$  PDF is uni-modal. Additionally, the value of the model coefficient is reasonably filter independent: PDFs associated with different filter widths have approximately the same mean, and relax towards a single value as the filter width increases.  $C_{prd}$  is therefore reasonably represented by a single, filter-independent constant. In agreement with several Reynolds averaged modeling approaches [34], Fig. 20 indicates that this coefficient should have a value of unity.

PDFs of the model coefficient  $C_{dis}$  are shown in Fig. 21, where  $C_{dis}$  is calculated

$$C_{dis} = \frac{\widetilde{Z''^2_{sf_s}} \left[ 2\overline{\rho \mathcal{D}_Z \left( \frac{\partial^2 Z}{\partial x_i \partial x_j} \right)^2} - 2\overline{\rho} \widetilde{\mathcal{D}_Z} \left( \frac{\partial^2 \tilde{Z}}{\partial x_i \partial x_j} \right)^2 \right]}{2\widetilde{\mathcal{D}_Z} \left( \widetilde{|\nabla Z|^2} - |\nabla \tilde{Z}|^2 \right)^2}. \quad (40)$$

The PDFs in Fig. 21 are again unimodal, but the value of  $C_{dis}$  is filter dependent. Consequently, this coefficient cannot be described as a single value. Filter dependencies such as these are often dealt with by employing dynamic models, but the dynamic procedure is not applicable to quantities like  $|\nabla Z|^2$  whose energy content exists on small scales.

#### Adapted Dynamic LES Closure

Here an alternative to the traditional dynamic approach is proposed. This alternative is rooted in the recognition that many turbulence modeling coefficients respond similarly

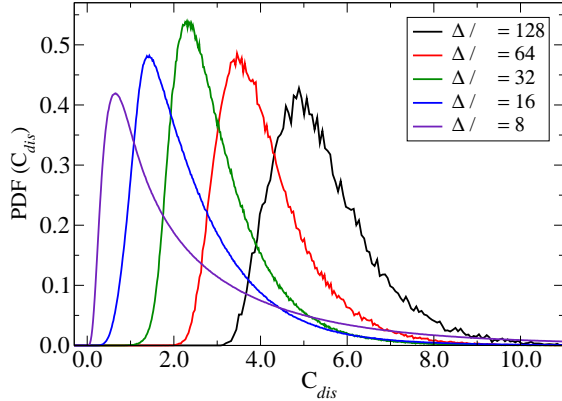


Figure 21: PDFs of  $C_{dis}$  from Eq. (38), evaluated from the homogeneous scalar mixing DNS. The PDFs are parameterized by the LES filter width  $\Delta$ .

to changes in the local intensity of turbulence. For example, if the passage of a turbulent eddy increases the local turbulent scalar flux, the scalar variance might be expected to increase in the same way. Similarly, a flow event that causes the local scalar variance to increase might also increase the local dissipation rate. Viewed from the reverse perspective, sub-filter model coefficients should tend toward zero in flow regions that laminarize or that are adjacent to walls.

The idea of the adapted dynamic closure is to take information from quantities that are amenable to dynamic calculations, and to apply that information to other quantities that are not similarly amenable. This projection of information is useful because small scale quantities are, like large scale quantities, sensitive to local turbulence. Information regarding local turbulence can be used to increase the accuracy of a model coefficient regardless of where the modeled quantity's spectrum peaks.

This projection of information is possible because an appropriate value of the model coefficient must exist. Indeed, the problem with applying a standard dynamic procedure to small scale quantities is not that the coefficients are indeterminate. Rather, the problem is that coefficient values cannot be calculated due to the absence of useful large scale information. The adapted dynamic closure simply circumvents this calculation problem by borrowing information from other readily obtained dynamic solutions.

The adapted dynamic closure can be used in the scalar mixing DNS to compute the coefficient  $C_{dis}$ . Dynamic information will be borrowed from the algebraic scalar variance model in Eq. (27), and  $C_{dis}$  will be rewritten as,

$$C_{dis} = C_{dis,d} \cdot \left( \frac{C_{var}}{C_{var}^0} \right). \quad (41)$$

$C_{dis,d}$  in this expression is now the unknown model coefficient, while  $C_{var}$  is the dynamically computed variance coefficient from Eq. (27).  $C_{var}^0$  is a baseline value of the variance coefficient that can be determined by using a Taylor series expansion to derive the algebraic

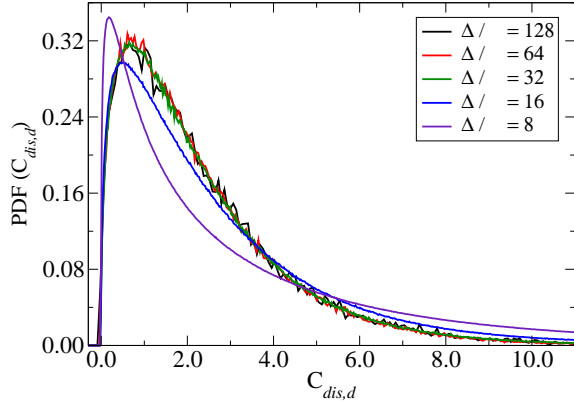


Figure 22: PDFs of the model coefficient  $C_{dis,d}$  from Eq. (41), evaluated from the homogeneous scalar mixing DNS. The PDFs are parameterized by the LES filter width,  $\Delta$ .

variance model [26]. Proceeding through this derivation leads to  $C_{var}^0 = 1/12$ . This number can be viewed as the variance coefficient's value in a particular turbulence regime. The details of this regime, and of its relationship to homogeneous turbulence, are irrelevant. These details will be accounted for in the specification of the constant  $C_{dis,d}$ . The intensity of  $C_{var}$  relative to this referenced regime is the only information of interest, and this information is captured by the ratio in Eq. (41).

The adapted dynamic closure is tested by using the scalar mixing DNS to calculate PDFs of the coefficient  $C_{dis,d}$ . Coefficients are determined by first using the DNS to determine the exact value of  $C_{var}$  at all locations in the DNS domain.  $C_{dis,d}$  is then determined from the expression

$$C_{dis,d} = \left( \frac{C_{var}^0}{C_{var}} \right) \frac{\widetilde{Z''^2_{sfs}} \left[ 2\rho \mathcal{D}_Z \left( \frac{\partial^2 Z}{\partial x_i \partial x_j} \right)^2 - 2\bar{\rho} \widetilde{\mathcal{D}}_Z \left( \frac{\partial^2 \tilde{Z}}{\partial x_i \partial x_j} \right)^2 \right]}{2\widetilde{\mathcal{D}}_Z \left( |\nabla \widetilde{Z}|^2 - |\nabla \tilde{Z}|^2 \right)^2}, \quad (42)$$

where  $C_{var}^0 = 1/12$ . The sub-filter variance  $\widetilde{Z''^2_{sfs}}$  in this expression is computed directly from the DNS, and the coefficient  $C_{var}$  is computed so that the algebraic sub-filter variance model is exact. Equation (42) differs from the expression used to calculate  $C_{dis}$  only in that it is multiplied by the inverse of the ratio ( $C_{var} / C_{var}^0$ ).

PDFs describing the distribution of  $C_{dis,d}$  in the scalar mixing DNS are plotted in Fig. 22. These distributions are largely independent of the LES filter width, and are unimodal. The information that is provided by the dynamic variance calculation therefore does account for the filter dependencies of the  $C_{dis}$  coefficient. The removal of this information reduces the extent of the physics that a model coefficient must attempt to describe. When the adapted dynamic procedure is incorporated into the modeling framework, the remaining coefficient  $C_{dis,d}$  can be accurately treated as a single, constant value.

The mean values of the  $C_{dis,d}$  distributions are approximately  $C_{dis,d} = 2.3$ , but the peaks of the distributions occur around  $C_{dis,d} = 0.75$ . Many RANS models use a dissipation model coefficient of approximately 1.0 [34] that sits in between these peak and mean values. To complete the closures for the LES  $|\widetilde{\nabla Z}|^2$  equation the value  $C_{dis,d} = 1.0$  is used, and the coefficient  $C_{dis}$  in Eq. (38) is modeled as

$$C_{dis} = C_{dis,d} \cdot \frac{C_{var}}{C_{var}^0} = 1.0 \cdot \frac{C_{var}}{(1/12)} = 12 C_{var}. \quad (43)$$

The LES transport equation for  $|\widetilde{\nabla Z}|^2$  may then be written in final form as

$$\begin{aligned} \frac{D}{Dt} \left( \bar{\rho} |\widetilde{\nabla Z}|^2 \right) &= \frac{\partial}{\partial x_j} \left( \bar{\rho} (\widetilde{\mathcal{D}}_Z + D_t) \frac{\partial}{\partial x_j} (|\widetilde{\nabla Z}|^2) \right) - 2\bar{\rho} \left( \frac{\partial \widetilde{u}_i}{\partial x_j} \frac{\partial \widetilde{Z}}{\partial x_i} \frac{\partial \widetilde{Z}}{\partial x_j} \right) \\ &\quad - 2\bar{\rho} \widetilde{\mathcal{D}}_Z \left( \frac{\partial^2 \widetilde{Z}}{\partial x_i \partial x_j} \right)^2 - \frac{2}{\bar{\rho}} \frac{\partial \bar{\rho}}{\partial x_i} \frac{\partial \widetilde{Z}}{\partial x_i} \left( \frac{\partial}{\partial x_j} \left( \bar{\rho} \widetilde{\mathcal{D}}_Z \frac{\partial}{\partial x_j} (\widetilde{Z}) \right) \right) \\ &\quad + 2 \frac{\partial (\bar{\rho} \widetilde{\mathcal{D}}_Z)}{\partial x_i} \frac{\partial \widetilde{Z}}{\partial x_i} \left( \frac{\partial^2 \widetilde{Z}}{\partial x_j \partial x_j} \right) + 2 \frac{\partial \widetilde{Z}}{\partial x_i} \frac{\partial \widetilde{Z}}{\partial x_j} \left( \frac{\partial^2 (\bar{\rho} \widetilde{\mathcal{D}}_Z)}{\partial x_i \partial x_j} \right) \\ &\quad + C_{prd} \cdot \bar{\rho} \cdot \frac{32 \cdot \nu_t}{\Delta^2} \cdot \left( |\widetilde{\nabla Z}|^2 - |\nabla \widetilde{Z}|^2 \right) - 12 C_{var} \cdot \bar{\rho} \cdot \frac{\widetilde{\mathcal{D}}_Z}{\widetilde{Z}_{sfs}''^2} \cdot \left( |\widetilde{\nabla Z}|^2 - |\nabla \widetilde{Z}|^2 \right)^2, \end{aligned} \quad (44)$$

where  $C_{prd}=1.0$  and  $C_{var}$  is the dynamically computed sub-filter scalar variance coefficient from Eq. (27). The variance  $\widetilde{Z}_{sfs}''^2$  that appears in the last term in Eq. (44) is determined from the solution of the conserved  $\widetilde{Z}$  equation and the  $\widetilde{Z}^2$  equation (Eq. (31)).

#### 2.4.6 Transport Equation Model Performance

The transport equation models for  $\bar{\chi}_Z$  and  $\widetilde{Z}_{sfs}''^2$  are now evaluated by returning to the LES simulations of the reactive jet case. Additional computations of both the 1 million cell LES and the 23 million cell LES are performed, and the  $|\widetilde{\nabla Z}|^2$  and  $\widetilde{Z}^2$  variables are solved for using Eqs. (44) and (31), respectively. These two variables are used to locally compute the dissipation rate  $\bar{\chi}_Z$  and the sub-filter variance  $\widetilde{Z}_{sfs}''^2$ .

Time averaged transported dissipation rates from both LES simulations are compared to the time averaged DNS dissipation rate and to the original algebraic model results in Fig. 23. The transported dissipation rate model improves upon the algebraic model in two ways. First, mesh dependencies are reduced. The algebraic model results were shown to be a strong function of the LES filter width. Conversely, the transport equation results in Fig. 23 are only weakly dependent on the LES filter. This change represents a significant improvement in model robustness. Second, the transported dissipation rate in the 1 million cell LES is in significantly better agreement with the DNS than the 1 million cell LES algebraic model.

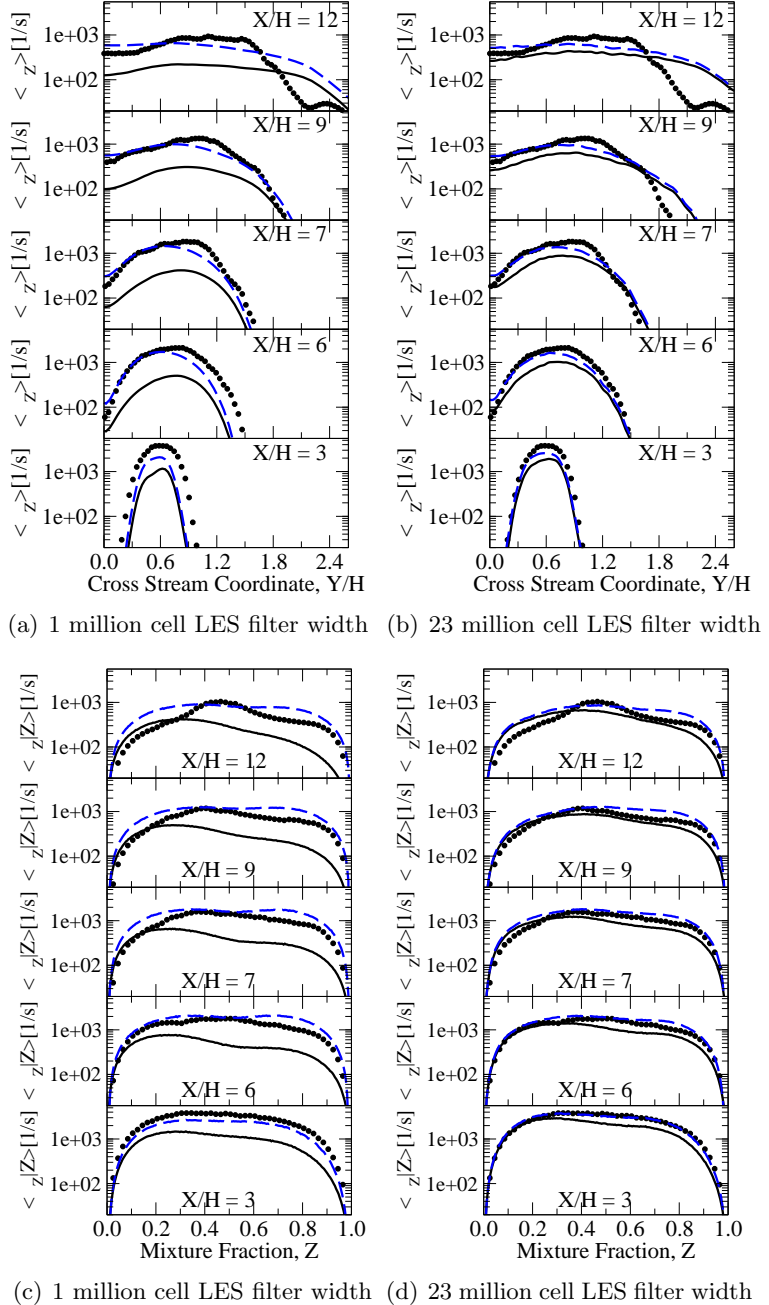


Figure 23: Dissipation rate,  $\bar{\chi}_Z$ , in both physical and mixture-fraction conditioned space in the reacting jet. DNS ( $\bullet \bullet \bullet$ ); algebraic  $\bar{\chi}_Z$  model (—); transported  $\bar{\chi}_Z$  model (—). (a) and (c): 1 million cell LES filter width; (b) and (d): 23 million cell LES filter width.

The improved agreement is attributed to two factors: 1) to improved prediction of the sub-filter variance production and variance dissipation processes that were inadequately represented by the algebraic approach, and 2) to the relaxation of the assumption that the dissipation rate is always in equilibrium with the local rate of variance production.

#### 2.4.7 Summary

This work has used an auto-igniting jet DNS to analyze the performance of LES algebraic and transport equation models for both the scalar dissipation rate and the sub-filter scalar variance. It was shown that the algebraic models under-predicted both the dissipation and the sub-filter variance in the jet. The under-predictions were almost entirely due to the sub-filter components of the algebraic expressions. These model errors motivated an examination of the closure of a transported scalar dissipation rate equation. An additional DNS of scalar mixing in homogeneous turbulence was introduced to aid this examination. The scalar mixing DNS demonstrated that sub-filter production of  $\bar{\chi}_Z$  could be described using a single model coefficient, while the coefficient associated with sub-filter dissipation of  $\bar{\chi}_Z$  was dependent on the LES filter. To account for this filter dependence, an adapted dynamic procedure was introduced and applied to the dissipation model coefficient. This procedure used information from a dynamic algebraic variance model to reduce the amount of physics that the dissipation model must describe. The resulting transport equation closure for  $\bar{\chi}_Z$  was shown to perform well for a variety of LES filter widths. The transport equation models were then applied in the reacting jet LES. The transported  $\bar{\chi}_Z$  model performed significantly better than the algebraic model and improved the agreement with the DNS results.

## 2.5 Modeling Sub-Filter Strain Effects In Turbulent Premixed Flames

### 2.5.1 Motivation

Premixed combustion is difficult to describe using Large Eddy Simulation (LES) because premixed flame structures are typically thinner than computationally tractable LES filter widths. The interaction of mixing physics and chemical kinetics is therefore under-resolved. Separation between the resolved LES scales and the flame structure scales creates modeling challenges when mixing is strong enough to perturb flame structures. For example, premixed flame structures respond to the influence of differential diffusion when non-unity Lewis number fuels are used, and to the influence of turbulence when the flame is in the thin reaction zones or broken reaction zones regime of the premixed regime diagram [1]. Quantities of interest such as burning velocities and pollutant formation rates can be highly sensitive to the details of these flame structure perturbations. Modeling these perturbations is therefore critically important in premixed LES.

Describing flame structure perturbations continues to be a critical modeling challenge, and the question of how to best describe these perturbations in LES remains open. In this section a two coordinate flamelet model is applied in an *a posteriori* LES of a highly strained

jet flame to address this challenge. A tractable implementation of a flamelet model that accounts for strain will be proposed and then validated using a DNS database.

### 2.5.2 Case Description: Premixed Jet DNS

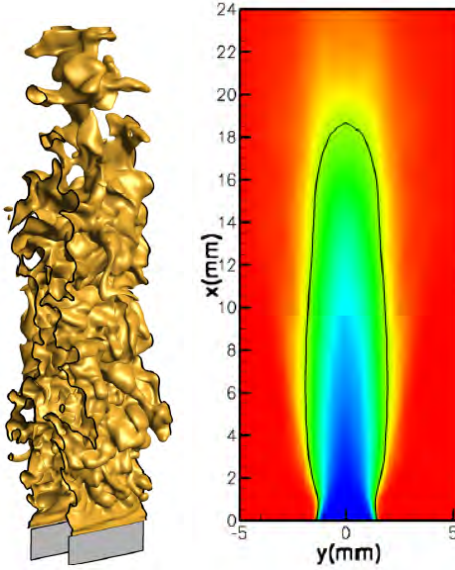


Figure 24: Premixed  $\text{CH}_4$  jet DNS from references [47, 48]. Left: instantaneous  $C = 0.065$  isosurface. Right: density weighted and time averaged  $C$  field, ranging from 0.00 (blue) to 0.19 (red), with the  $C = 0.065$  isosurface denoted as a black line.

of the central jet is  $H = 1.8$  mm and the corresponding jet Reynolds number is  $\text{Re}_j = 2100$ .

The magnitude of the turbulent fluctuations in the central jet is  $u'/s_L = 10$  and the integral turbulent length scale is  $l_t/l_F = 4$ . The corresponding Karlovitz ( $\text{Ka} = l_F^2/\eta^2$ ) and Damköhler ( $\text{Da} = s_L l_t/u' l_F$ ) numbers are  $\text{Ka} = 225$  and  $\text{Da} = 0.4$ , implying that this flame sits just inside the broken reaction zones regime of the turbulent premixed flame regime diagram [1, 49]. Turbulence is therefore expected to strongly influence premixed flame structures. The DNS was run on a 195 million ( $1200 \times 600 \times 270$ ) cell mesh.

### 2.5.3 Strained Premixed Flamelet Model

#### *Strained Flamelet Formulation*

This section introduces the strained premixed flamelet LES model. The model builds upon laminar strained flamelet models [22, 50, 51, 52] and turbulent unstrained flamelet models [19, 49, 53] by considering strain in the context of LES. Chemistry in the model will be described using solutions of the counterflow premixed flamelet equations that were

developed by Dixon-Lewis *et al.* [54]. These equations describe premixed flames that burn in a back-to-back fashion while subject to strain. Because the full form of the equations is available in reference [54], they are only briefly reviewed here. The equations are expressed as a function of a 1-D similarity coordinate  $\eta$  defined as

$$\eta = \left( \frac{a}{\nu_0} \right)^{1/2} \int_0^y \frac{\rho(s)}{\rho_0} ds. \quad (45)$$

The  $y$  variable is a physical space coordinate that is aligned perpendicular to the counterflow flame fronts and parallel to the direction of the incoming unburned gas flow. The density is  $\rho$ , the viscosity is  $\nu$ , and the subscript 0 denotes a reference point in the unburned gas. A coordinate  $x$  is aligned perpendicular to the  $y$  coordinate, and the strain rate in the flame system is defined as the derivative of the velocity in the  $x$  direction ( $u$ ), evaluated in the unburned gas,  $a = du_0/dx$ .

The similarity coordinate can be used to write species equations for the asymptotic counterflow premixed flames as a function of one variable. For example, the transport equation for the species  $\phi_i$  is

$$\frac{-f}{(a\nu_0)^{1/2}} \frac{d\phi_i}{d\eta} = \frac{-1}{\rho_0(\nu_0 a)^{1/2}} \frac{d}{d\eta} (\rho\phi_i V_{i,\eta}) + \frac{\dot{m}_i}{a\rho}, \quad (46)$$

where  $V_{i,\eta}$  is the standard diffusion velocity of  $\phi_i$  written in terms of the  $\eta$  direction. The function  $f$  appears in expressions for the physical space velocities  $u$  and  $v$  and is defined so that continuity is satisfied,

$$\rho v = -\rho_0 f \quad , \quad \rho u = x\rho_0 (df/d\eta). \quad (47)$$

Inserting these velocities into the momentum transport equations yields an expression that can be solved to determine  $f$ . Further details about the strained equations can be found in reference [54].

In the present study, the flamelet equations will be used to describe a symmetric counterflow flame configuration, and will therefore be solved only between one inlet stream and the symmetry plane. Boundary conditions in the inlet stream are set using information from the central jet in the DNS: unburned CH<sub>4</sub> and air at an equivalence ratio of  $\phi = 0.7$  and a temperature of  $T_u = 800\text{K}$ . Neumann conditions are applied at the symmetry plane.

The FlameMaster program [16] is used to solve the stretched flamelet equations (Eq. (46), e.g.) with the 17 species CH<sub>4</sub> mechanism that was employed in the DNS. Differential diffusion is expected to be important within the inner reaction zone, and constant non-unity Lewis numbers are therefore used for all chemical species. Flamelet solutions are generated for a variety of values of the strain rate parameter  $a$ , and the standard s-curve [1] that results from these calculations is shown in of Fig. 25(a). This figure shows that the maximum flamelet temperature will initially decrease as the imposed strain is increased. A turning point is eventually reached, however. Increasing the strain beyond the critical value associated with this turning point has the effect of quenching the flamelet. Decreasing the

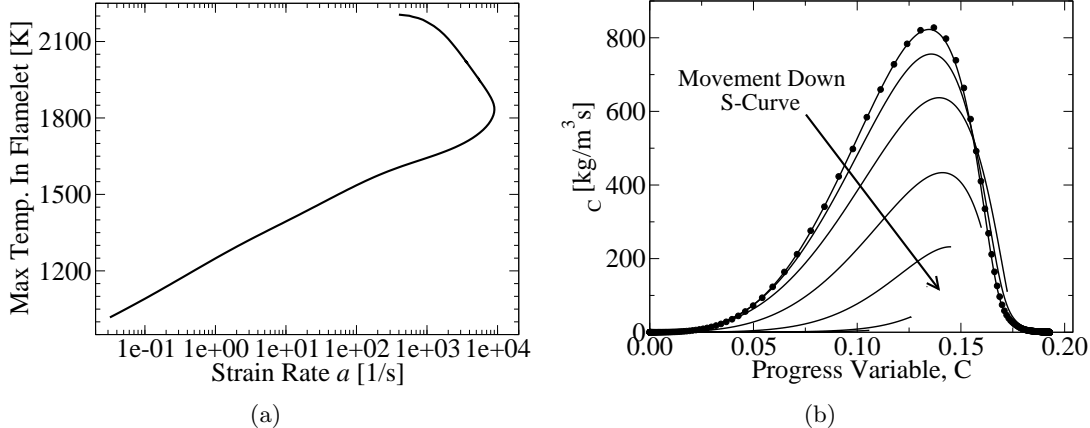


Figure 25: Premixed strained flamelets. (a): maximum flamelet temperature vs. imposed strain rate (the so-called s-curve). (b): progress variable source terms in unstrained (•••) and strained (—) flamelet solutions. The rightmost ends of the strained flamelet solutions in (b) correspond to the symmetry boundary condition, and the strained solutions represent the entire range of strainrates shown in (a).

strain imposed on a flamelet near the turning point, conversely, may push the solution onto the so-called middle branch of the s-curve. This branch describes steady flamelet solutions which are unstable in the sense that they will relax toward the upper or lower branches when perturbed. Although unstable, these middle branch solutions are important in the premixed slot-jet DNS where turbulence induces unsteadiness in the premixed flame structure.

A progress variable will be defined in this study as  $C = Y_{H_2O} + Y_{H_2} + Y_{CO_2} + Y_{CO}$ , where the  $Y_i$ 's denote species mass fractions. Figure 25(b) shows the chemical source term associated with  $C$  in several of the strained flamelet solutions. Movement down the s-curve decreases the magnitude of these source terms. This demonstrated sensitivity to strain is a leading order effect in the flamelet model, and it will be shown below that this effect must be captured if the slot-jet DNS is to be predicted correctly.

#### Tabulation Coordinate Selection

The stretched flamelet solutions are parameterized and tabulated for use in LES. Changes along a single flamelet solution are parameterized using the progress variable  $C$ . A second coordinate is needed to parameterize the influence of the imposed strain rate  $a$ . The dissipation rate of the progress variable,  $\chi_C = 2\mathcal{D}_C|\nabla C|^2$ , the mass fraction of a minor species, and the strain rate itself could all be used as a second coordinate. It is important to note that spatial variations of each of these coordinates are characterized by length scales on the order of the premixed flame structure, and that this presents modeling challenges. Any coordinate that parameterizes strain will be subject to this challenge, however, because coordinates that only exist on larger scales will not be sensitive to turbulent strain effects. The particular choice of a second coordinate that is used in this study will be motivated by referring to profiles from the strained flamelet solutions plotted in Fig. 26.

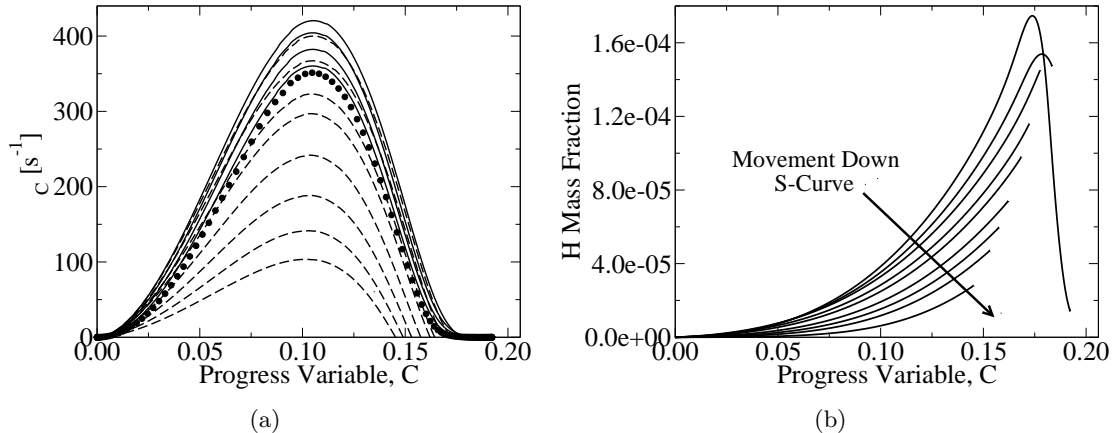


Figure 26: (a): progress variable dissipation rate in an unstrained flamelet ( $\bullet\bullet\bullet$ ), and in strained flamelets above (—) and below (—) the turning point of the s-curve. (b): hydrogen mass fractions in the strained flamelets.

Figure 26(a) shows  $\chi_C$  as a function of  $C$  in several flamelets. The limiting solution of zero strain ( $a \rightarrow 0$ ) is shown as solid circles, while solutions associated with the upper branch of the s-curve in Fig. 25(a) are shown as solid lines. On the upper branch, the dissipation rate tends to increase as the imposed strain rate increases. Dissipation peaks near the turning point of the s-curve and then begins to fall as the strain rate is decreased. Flamelet solutions from the middle branch of the s-curve are shown as dashed lines in Fig. 26(a). Many of these middle branch solutions are characterized by dissipation rates that are similar to the rates in the upper branch solutions. The  $\chi_C$  parameter therefore fails to uniquely parameterize strain: both upper and middle branch solutions can be found at a single location in  $(C, \chi_C)$  space. This lack of uniqueness is analogous to the lack of uniqueness associated with parameterizing non-premixed flamelet solutions using the mixture fraction and its dissipation rate [10].

Unlike the dissipation rate, the hydrogen radical mass fraction ( $Y_H$ ) does uniquely parameterize the influence of strain. Figure 26(b) shows  $Y_H$  as a function of  $C$  in flamelets spanning the entire s-curve. Movement down the s-curve results in a monotonic decrease of hydrogen over virtually all of progress variable space. Additionally, the hydrogen radical's concentration varies significantly as a function of the imposed strain. This variation is helpful in that small numerical errors made in the calculation of  $Y_H$  are not expected to influence the flamelet solution that is accessed. The hydrogen mass fraction is therefore selected as a second parameterizing coordinate, and the stretched flamelet solutions are tabulated as

$$\phi_i = \phi_i(C, Y_H). \quad (48)$$

The use of hydrogen captures the same kind of information as the coordinates suggested by other researchers in fully resolved contexts. For example, strain effects have also been

described using elemental mass fractions [51], the CO radical [55], the OH radical [22], and the temperature [52]. The advantages of hydrogen include its sensitivity to strain, its straightforward transport equation, and its small Lewis number which allows for some implicit capture of differential diffusion effects. Additionally, the use of a chemical species in place of a strain rate is expected to reduce the sensitivity of the model to the details of how strain is induced in the flamelet equations (back-to-back flamelets versus a different configuration).

#### *Unstrained Flamelet Model For Comparison*

The strained flamelet model will be compared with an unstrained model to better understand the importance of strain effects in the jet flame DNS. In place of the strained flamelet equations (Eq. (46), e.g.), this unstrained model solves 1-D unstrained premixed flamelets. This model is representative of a typical premixed flamelet LES implementation [53, 19]. The equation that governs the species mass fraction  $\phi_i$  in the unstrained flamelets is

$$\rho_u s_{L,u} \frac{d}{dx} (\phi_i) = \frac{d}{dx} (\rho \phi_i V_{i,x}) + \dot{\omega}_i. \quad (49)$$

The diffusion velocity in the  $x$  direction,  $V_{i,x}$ , accounts for typical molar molecular diffusion effects. The chemical source term is  $\dot{\omega}_i$ , the unstrained laminar burning velocity is  $s_{L,u}$ , and the density in the unburned gas is  $\rho_u$ . Just as in the strained flamelet model, constant non-unity Lewis numbers are used for all species and the equations are solved with the 17 species CH<sub>4</sub> mechanism employed in the DNS.

Because no strain parameter appears in the unstrained model, only one flamelet can be used to describe the conditions in the DNS ( $\phi = 0.7$ ,  $T_u = 800\text{K}$ ). The resulting flamelet solution is parameterized using the progress variable  $C$ , and flamelet quantities in the unstrained model are accessed as

$$\phi_i = \phi_i(C). \quad (50)$$

#### *Sub-filter Modeling*

LES filtering will be accounted for in these combustion models using a standard presumed probability distribution function (PDF) approach [10, 14, 19]. This approach assumes that the sub-filter distribution of the independent flamelet parameters may be modeled using presumed distributions whose exact shapes depend on the LES filtered moments of the parameters. The filtered value of any chemical quantity may then be determined by integrating the product of the flamelet solution and the presumed distribution. In both the strained and unstrained models, a beta-PDF ( $\beta$ ) will be used to describe sub-filter progress variable distributions. A beta-PDF depends on a mean and a variance, so that filtered quantities in the unstrained model are calculated as

$$\tilde{\phi}_i(\tilde{C}, \tilde{C''^2}) = \int \phi_i(C) \cdot \beta(C; \tilde{C}, \tilde{C''^2}) dC. \quad (51)$$

Beta-PDFs typically describe distributions that are bounded between zero and one, but the maximum progress variable in the flame is less than unity. To account for this, the

beta-PDF is rescaled so that it describes distributions between  $C = 0$  and the maximum expected progress variable value,  $C = 0.20$ .

In the strained model, the mass fraction of hydrogen is employed as an additional tabulation coordinate. This mass fraction is used to determine which strained flamelet solution from the chemistry database is accessed by the flow solver. Just as in the unstrained model, the mean and variance of the progress variable in any LES cell can be used to specify a beta-PDF,  $\beta(C; \tilde{C}, \tilde{C}'^2)$ , that approximates the distribution of  $C$  in the cell. The beta-PDF can be integrated against the hydrogen profile from any single strained flamelet solution to determine its conditional hydrogen mass fraction,  $\tilde{Y}_H|C$ . The particular strained flamelet that is selected for access is the one whose conditional hydrogen mass fraction matches that of the transported LES hydrogen mass fraction,  $\tilde{Y}_H$ . This comparison is mathematically performed by presuming that the distribution of the conditional hydrogen value is a delta-PDF. Chemical quantities then are written

$$\tilde{\phi}_i(\tilde{C}, \tilde{C}'^2, \tilde{Y}_H) = \iint \phi_i(C, Y_H) \beta(C; \tilde{C}, \tilde{C}'^2) \delta(\tilde{Y}_H - \tilde{Y}_H|C) dC dY_H. \quad (52)$$

The variance of the progress variable is calculated using an algebraic model with a dynamically computed coefficient  $C_s$  [23],  $\tilde{C}'^2 = C_s \Delta^2 |\nabla \tilde{C}|^2$ .

#### 2.5.4 LES Approach

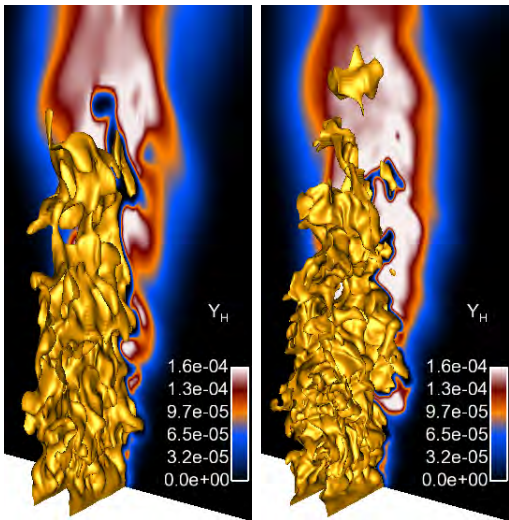


Figure 27: Schematics of the strained model LES runs. The  $\tilde{C} = 0.065$  surface is plotted over contours of the transported  $\tilde{Y}_H$  scalar. Left: 1.2 million cells. Right: 9.3 million cells.

LES computations of the slot-jet DNS are performed using two different mesh resolutions. The first mesh consists of 1.2 million cells, and the corresponding filter width ratios are  $\Delta/\eta = 8$  and  $\Delta/l_F = 0.5$ . The second LES mesh consists of 9.3 million cells, and the corresponding filter ratios are  $\Delta/\eta = 4$  and  $\Delta/l_F = 0.25$ . Although they are relatively fine, these LES resolutions rigorously test the models because they describe unresolved inner premixed flame structures using only the flamelet databases.

Both meshes employ stretching, so that the cell size increases in the downstream and radial directions. The LES simulations are performed using a parallel finite difference code [56] that is advanced in time using a Crank-Nicolson-type second order implicit scheme. Spatial gradients are calculated using second order schemes for velocities and third order schemes for scalars. The code is

run in a low-Mach formulation, and a Poisson equation is solved for the pressure variable that enforces mass conservation.

Both the strained and unstrained flamelet models are applied on the 1.2 million cell mesh, while only the strained model is applied on the 9.3 million cell mesh. A schematic of the strained flamelet results on the two different meshes is shown in Fig. 27. Comparison of the flame fronts in Figs. 24 and 27 indicates that the features of the flame surface are reasonably captured by the LES. The hydrogen mass fraction that is shown in the contour plots in Fig. 27 on a streamwise-transverse plane is characterized by relatively smooth structures on the burned side of the front due to the particularly high diffusivity of hydrogen at high temperatures.

$\tilde{C}$  and  $\tilde{Y}_H$  scalars are both solved for in the LES using standard transport equations. The Lewis number of the progress variable is set as  $\text{Le}_C = 1$ , while that of the hydrogen radical is set as  $\text{Le}_H = 0.18$ .

It is known [49] that premixed flame fronts are under-resolved in standard implicitly filtered LES computations. This issue is dealt with in the current study by coupling the progress variable transport equation with a level set solution according to the procedure in reference [14]. In this coupling the level set solution is used to adjust the progress variable chemical source in the immediate vicinity of the flame front. This adjustment ensures that the flame front propagates at an appropriate turbulent burning velocity even in the presence of numerical errors caused by poor flame resolution. The source term in the hydrogen mass fraction transport equation is not directly coupled with the level set because it rapidly responds to the progress variable field and the changes that the level set induces in this field.

The transported level set requires a laminar burning velocity, a model for the turbulent burning velocity, and a method of reinitializing the level set field to ensure it maintains a smooth gradient. The laminar burning velocity is accessed from the unstrained and strained flamelet databases using Eq. (51) and Eq. (52), respectively. The influence of the local hydrogen mass fraction is therefore accounted for in the strained model LES simulations. The model of Pitsch [49] is used to describe the influence of turbulence on the burning velocity, and level set reinitialization is accomplished using a parallel fast marching method [57].

### 2.5.5 Results And Discussion

#### *Progress Variable*

Time averaged progress variable and progress variable source term results from the strained and unstrained LES runs are compared with corresponding DNS results in Fig. 28. At the first three measurement stations, the unstrained flamelet LES (black line) is seen to over-predict the progress variable source term. The stretched flamelet models, conversely, are able to predict how turbulent mixing perturbs the flame structure and lowers the source terms. These different conditional source term profiles do not affect the progress variable solutions near the nozzle, where resolved mixing processes control scalar transport. The

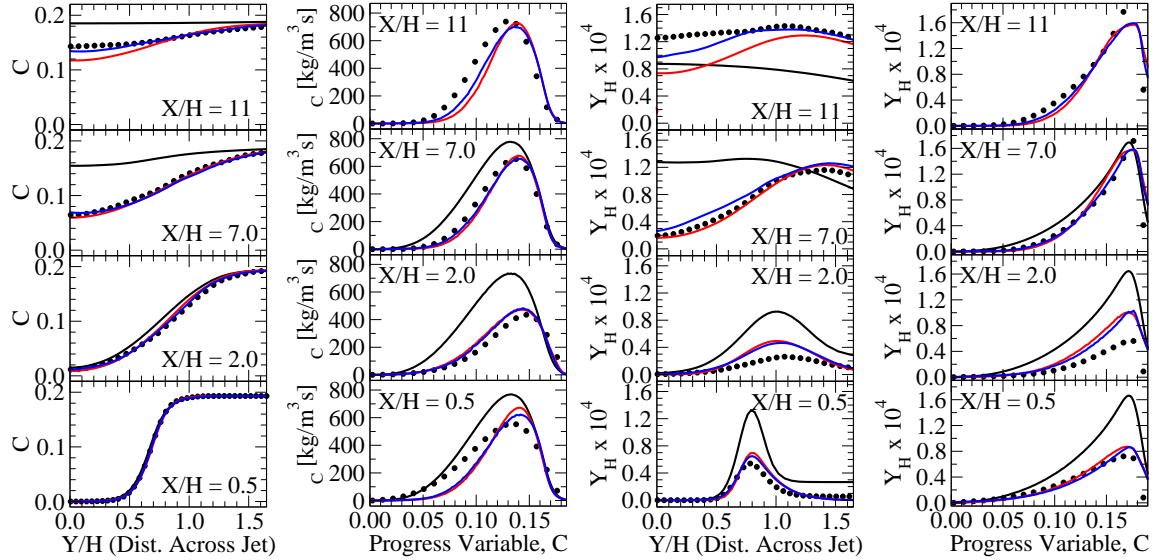


Figure 28: Progress variable, progress variable source term, and unconditional and conditional hydrogen from: DNS (●●●); unstrained flamelet LES (—); strained flamelet LES with 1.2 million cells (—); strained flamelet LES with 9.3 million cells (—).

influence of the source term does appear, however, by the time fluid parcels reach the  $X/H=7.0$  station. There the unstrained model over-predicts the progress variable, indicating that the burning velocity is not correctly described. This error in the  $\tilde{C}$  predictions persists at the farthest downstream station ( $X/H=11$ ). In contrast with the unstrained model, the strained model is able to reproduce both the source term and progress variable DNS results. Some mesh sensitivity is noticeable at  $X/H=11$ , but agreement with the DNS improves with increasing LES resolution, as expected.

### Hydrogen

LES and DNS hydrogen results are compared in Fig. 28, where both unconditioned and conditional data are plotted. The unstrained model tends to overpredict  $\tilde{Y}_H$  near the inlet, where turbulence induced strain is strongest. The strained flamelet models, conversely, agree well with the DNS. This trend is consistent with the progress variable data in Fig. 28 in that strain tends to moderate the progress variable source term and the buildup of the radical pools that drive flame propagation. At downstream locations where turbulence has attenuated, Fig. 28 indicates that the unstrained model predicts conditional hydrogen profiles quite well. The unconditional data is poorly predicted, however, due to the over-prediction of  $\tilde{C}$  that was discussed above.

### Minor Species

Minor species data from the LES and DNS runs are compared in Fig. 29. The strained model has more difficulty predicting CO than it does predicting the transported  $\tilde{C}$  and  $\tilde{Y}_H$

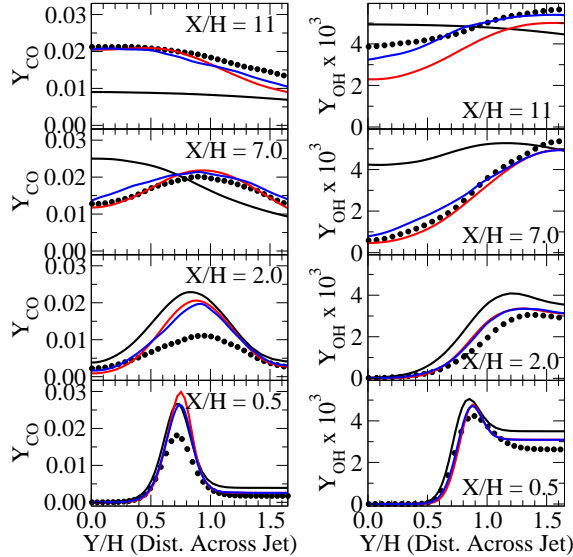


Figure 29: CO (left) and OH (right) mass fractions from: DNS ( $\bullet \bullet \bullet$ ); unstrained flamelet LES (—); strained flamelet LES with 1.2 million cells (—); strained flamelet LES with 9.3 million cells (—).

scalars. The first two stations in Fig. 29, for example, are characterized by significant CO over-predictions. Thornber *et al.* [58] also observed some error in their LES-CMC predictions of CO near the  $X/H=2.0$  station, although the error changed from an over-prediction of CO on a coarse mesh to an under-prediction on a finer mesh. These errors may arise because CO is responsive to the details of the imposed strain field. A reduced flamelet manifold in which this species is assumed to be completely described by two parameters may therefore be insufficient. The progress variable, which contains CO, benefits from the fact that it is defined to simultaneously consider CO and  $CO_2$ , reducing sensitivity to oxidation reactions involving both species.

At downstream stations the quality of the strained model CO predictions improve, and little sensitivity to the LES mesh is noticeable. Strained flamelet predictions of the OH radical are in relatively good agreement with the DNS throughout the flame, while the unstrained model OH predictions are subject to errors at downstream locations.

### 2.5.6 Summary

This study proposed a strained flamelet model for describing high Karlovitz number premixed flames in the context of LES. The model was validated by performing a series of LES computations of a premixed slot-jet flame DNS that exists on the edge of the broken reaction zones regime. The LES computations compared the strained flamelet model with an unstrained model, and considered two LES mesh resolutions. It was found that strain effects had a leading order influence on flame propagation, and that the strained flamelet model could accurately predict this influence in LES.

## 3 Chemical Mechanisms For Jet Fuel Surrogates

### 3.1 Review Of Objectives

Part two of this project aimed to develop a consistent, reliable, and compact chemical scheme for a potential jet fuel surrogate. The first project objective was the formulation of a surrogate mixture that can accurately represent the average properties of jet fuel. This formulation is accomplished using a constrained optimization approach, as discussed below. The second objective was the development of a chemical mechanism that can describe the oxidation of this potential surrogate. Development of this mechanism is discussed in the second half of the section.

A single consistent chemical mechanism was developed earlier [59] to describe the oxidation of smaller hydrocarbons, from C<sub>1</sub> to C<sub>8</sub> species. Pathways for soot formation were included in its formulation. This mechanism is used as a base model for the kinetic approach that is developed here. In the current project, the base model is extended so that it includes the oxidation pathways of the individual components of the surrogate mixture. The combined chemical scheme's description of oxidation is validated at each step of this process. The resulting chemical model's ability to describe the global combustion characteristics of jet fuel is then examined.

The mechanism development process utilizes the multi-stage reduction strategy developed under a previous AFOSR-funded project. The reduction tools exploited include the Directed Relation Graph with Error Propagation (DRGEP) reduction method [60]. DRGEP automatically eliminates from a kinetic mechanism the species and reactions that do not contribute significantly to the overall dynamics of a chemical process. Additionally, a chemical lumping scheme [61] is used to group chemical isomers into lumped species. All numerical calculations have been performed using the FlameMaster program [62].

### 3.2 Definition Of Surrogates For Jet Fuels

#### 3.2.1 Choice Of Individual Components

A natural procedure to select suitable components of the surrogate mixture for a particular fuel, is to identify a representative hydrocarbon, to stand for each of the major hydrocarbon classes found in the real fuel. Based on molecules identified as relevant to jet fuels [8], the components of the jet fuel surrogate for this work have been chosen as: (a) *n*-dodecane, to represent the paraffin class; (b) methylcyclohexane, to represent the naphthene class; and (c) *m*-xylene to represent the aromatics.

This choice is motivated by several observations. First, *n*-dodecane has physical properties close to JP-8/Jet-A over temperature ranges of 100–650°C [63, 64]. Second, *m*-xylene aids the surrogate in reproducing the sooting tendencies of a jet fuel. Finally, methylcyclohexane is the simplest branched naphthene that can be modeled reliably. The global ignition and flame propagation characteristics of these components have been examined in several experimental studies, and some of their key chemical reaction pathways have also been the object of theoretical and experimental kinetic rate determinations. It is important

Parameters	Gasoline	Jet fuel	Diesel fuel
Lower HV [MJ/kg]	43.4	43.3	42.7
Carbon number range	4-12	8-16	9-23
Approximate formula	$C_{6.9}H_{13.5}$	$C_{11}H_{21}$	$C_{16}H_{28}$
Liquid density [kg/l]	0.735	0.775-0.840	0.850
Molecular weight [g/mol]	$\sim 96.3$	$\sim 153$	$\sim 220$

Table 1: Average properties of transportation fuels key to define surrogates for combustion applications. Data compiled from several sources [63, 65, 66, 67].

to choose representative components that have been carefully studied, in order to assess the ability of the surrogate kinetic model for the individual component description, which is in itself key to the performance of the multi-component surrogate model.

### 3.2.2 Composition Of Individual Components

A constrained optimization approach is used to determine the composition of the individual components of the surrogate mixture. Given a choice of components to make up the surrogate (here *n*-dodecane, methylcyclohexane, and *m*-xylene), an optimized component composition is determined, so that the properties of the surrogate fuel resemble the target real fuel properties. The procedure itself was developed as a part of a previous AFOSR grant. A brief description is provided here.

The average properties of typical transportation fuels that need to be considered to design a surrogate for combustion applications are shown in Table 1. The problem of determining the composition of individual components in the surrogate mixture is formulated as a constrained optimization problem. The average real fuel properties are the desired optimization targets, and some of the target real fuel properties could be used as constraints. In recasting the problem, the mixture properties are determined by exploiting the fact that most of these target real fuel properties are indeed bulk properties; the multi-component surrogate fuel's average properties are hence expressed as combinations of individual component properties. Structural group analysis is also used wherever appropriate, for instance to determine Threshold Sooting Index (TSI) of the surrogate fuel.

The optimal component composition of a jet fuel surrogate that is obtained by solving the constrained optimization problem for *n*-dodecane, methylcyclohexane, and *m*-xylene is provided in Table 2. It can be seen that the proposed jet fuel surrogate agrees with the target real fuel properties as far as the composition of major hydrocarbons, and H/C ratio (which is indicative of the heating value of the jet fuel) is concerned. The sooty tendency measure, *Threshold Sooting Index*, of the jet fuel is also captured by the model surrogate. However, the average chemical formula and the fuel molecular weight are different between the real fuel and the model surrogate. If a heavier naphthalene were to be included, these differences could be resolved. In spite of these discrepancies, it will be shown in the later sections that the surrogate proposed here accurately describes the real fuel's combustion characteristics.

	Jet-A/JP-8 properties	Model JP-8 Surrogate
H/C ratio	$1.91 \pm 0.05$	1.94
Average formula	$C_{11}H_{21}$	$C_{9.64}H_{18.75}$
Liquid density (kg/l)	0.810	0.769
Molecular weight (g/mol)	153	134.80
Threshold Sooting Index (TSI)	15	15.34
Composition (% volume)	~60% paraffins ~20% cyclo paraffins ~18% aromatics	62% <i>n</i> -dodecane 19.8% methylcyclohexane 17.6% <i>m</i> -xylene

Table 2: A model jet fuel surrogate

### 3.3 A Single Chemical Mechanism Describing A Jet Fuel Surrogate

Having determined the composition of an optimal jet fuel surrogate as described above, it is our objective to elaborate the development of a single, consistent and reliable chemical scheme to accurately model such a surrogate mixture. The basic idea is pictorially represented in Fig. 30. As mentioned earlier, the present work uses the detailed mechanism published by Blanquart *et al.* [68] as the base chemical model. This mechanism has been developed for the oxidation of thirteen fuels ranging from the C<sub>1</sub> to the C<sub>8</sub> species, and including alkanes such as *n*-heptane and iso-octane. Additionally, aromatic species such as benzene and toluene are included. This base mechanism has been extensively validated against ignition delay times and laminar burning velocities over a wide range of temperatures and pressures. Finally, it has been applied to a series of laminar premixed and diffusion flames. In all the cases investigated, the mechanism was found to reproduce the experimental measurements well.

Here, a detailed discussion of the extension of the base chemical model is provided. This extension will introduce the reaction pathways of several substituted aromatics, including *m*-xylene. Particular attention is paid to demonstrate the ability of the mechanism to predict the kinetics of *m*-xylene, since it is a component of the proposed surrogate. Thereafter, the procedure to extend the chemical model to include kinetics of *n*-dodecane is discussed, and extensive validation tests for this normal alkane are provided. A similar approach to extend the chemical scheme to include reaction pathways of the naphthene representative in the proposed surrogate, methylcyclohexane, is then discussed. The resulting chemical mechanism would serve to reliably predict the kinetics of the model jet fuel surrogate proposed in Table 2.

#### 3.3.1 Extension To Substituted Aromatics

Aromatic compounds are major constituents of real engine fuels: 25% by volume in gasoline, 33% in diesel, and 16% in jet fuels (JP-8, Jet A/A-1) [69]. They are used as anti-knock additives to enhance the octane number of the fuels, since they have high resistance to auto-ignition [70]. Aromatic species also play a crucial role in the formation of soot as

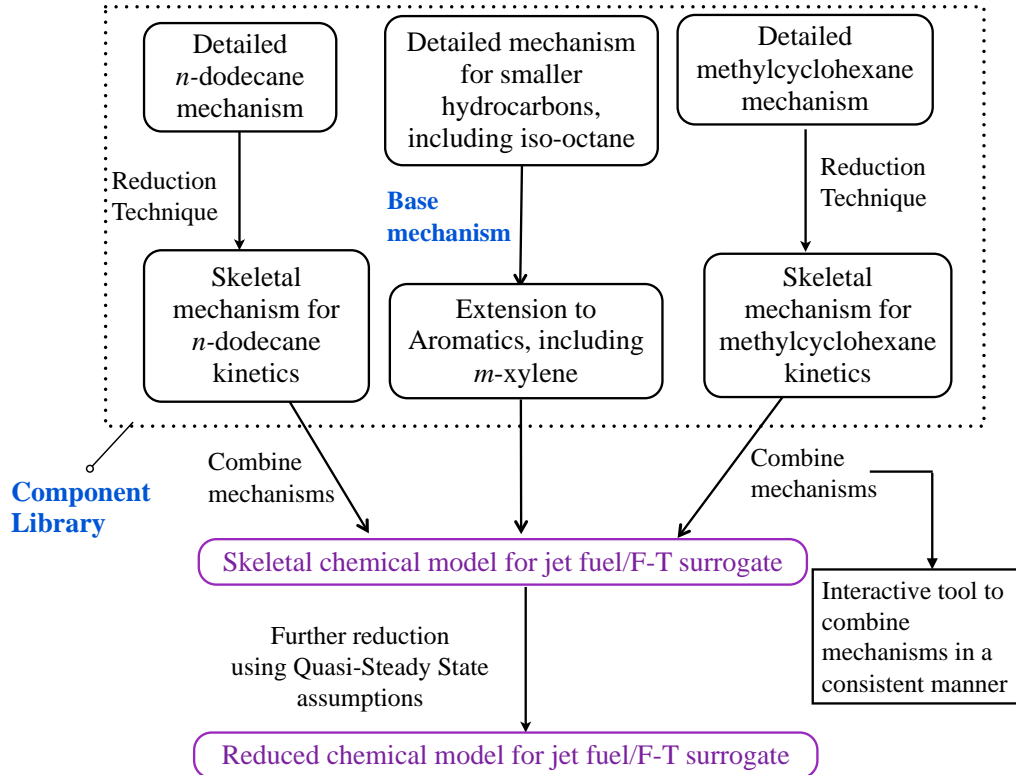


Figure 30: Schematic of the development of a chemical model for the oxidation of a proposed jet fuel surrogate.

they enhance the formation of soot precursors such as Polycyclic Aromatic Hydrocarbons (PAHs). Therefore, understanding and accurately modeling the chemistry of aromatic compounds is an essential component of the process of describing surrogate fuels.

Much work in the past has been devoted to modeling combustion of toluene. Chemical mechanisms for high-temperature (875 - 1500 K) gas-phase oxidation of benzene, toluene, ethylbenzene, and propylbenzene are described and discussed in detail by Brezinsky *et al.* [70, 71]. A detailed chemical kinetic mechanism for combustion of toluene at intermediate and high temperatures has been assembled and evaluated by Lindstedt and Maurice [72] for a wide range of oxidation regimes.

Mechanisms for dimethylbenzenes (xylenes) have also been established in the literature. Battin-Leclerc *et al.* [73] measured ignition delay times of xylenes in a shock tube and proposed a reaction scheme to reproduce the experimental results. Gail and Dagaut [74] studied oxidation of *p*-xylene (1,4-dimethylbenzene) and *m*-xylene (1,3-dimethylbenzene) in a Jet Stirred Reactor (JSR) at atmospheric pressure. Similarly, a detailed kinetic model was developed to describe the oxidation of *p*-xylene that represents the experimental JSR results. Finally, a detailed chemical mechanism was proposed for the oxidation of *o*-xylene (1,2-dimethylbenzene) and *m*-xylene by the same group [75, 76] to represent their JSR and

ignition delay time results.

In the study of bi-ringed substituted species, Shaddix *et al.* [77] proposed reaction pathways for the high temperature oxidation of 1-methylnaphthalene based on the observed intermediate species profiles in plug flow reactor (PFR) measurements [77]. Pitsch [78] proposed a mechanism for the oxidation of 1-methylnaphthalene and validated the mechanism with PFR and ignition delay time data. More recently, Mati *et al.* [79] also developed a model for 1-methylnaphthalene oxidation and validated their mechanism with JSR measurements and ignition delay times.

As is evident, in almost all of the work done thus far, the focus has been on developing detailed chemical mechanisms for the oxidation of individual fuel species. In the present effort, a single mechanism has been developed from on the base model described earlier. This single mechanism can be used to describe several substituted aromatics: toluene, ethylbenzene, styrene,  $\alpha$ -methylnaphthalene and *m*-xylene [80]. The focus of this report is laid on *m*-xylene since this is a component of the proposed surrogate for jet fuels. The *m*-xylene validation tests that will be discussed include ignition delay times, species concentration profiles in shock tube experiments, PFR data, and laminar burning velocities.

For clarity, in the rest of the article, abbreviations according to those introduced by Frenklach *et al.* [81] have been used. For instance,  $A_1$  is benzene,  $A_1CH_3$  is a methyl-substituted species consisting of one aromatic ring (*i.e.* toluene),  $A_1(CH_3)_2$  refers to a bi-methyl substituted one-ringed aromatic (*i.e.* xylene),  $A_1^-$  refers to a phenyl radical,  $A_1CH_3^*$  refers to a methylphenyl radical,  $A_2^-$  is the naphthyl radical, and  $A_2CH_3$  refers to a methyl-substituted species consisting of two aromatic rings (*i.e.* methylnaphthalene). In the following sections, substitutions on a naphthyl ring refer to the  $\alpha$  site if not stated otherwise.

## Mechanism Development

The present chemical mechanism is composed of 158 species and 1804 reactions (forward and backward reactions counted separately). Most of the reactions are treated as reversible with the rate constants for the reverse reactions evaluated from the corresponding equilibrium constants.

The oxidation pathways of substituted aromatic molecules are strongly coupled. For instance, the chemistry of xylene depends on the chemistry of toluene, which in turn depends on the chemistry of benzene. The present chemical model proposes a consistent framework to describe the pyrolysis and oxidation of these aromatic fuels. Consistency here has three different meanings. First, the chemistry of all the fuels is described by one single kinetic mechanism. This means, for example, that the toluene part of the mechanism is used to describe the oxidation of toluene itself, but also as a sub-mechanism in the oxidation of larger species, such as xylene, ethylbenzene, and others. In addition, the chemistry for all aromatic fuel molecules is based on the same chemical mechanism for smaller hydrocarbons. Second, the rate constants used for reactions of a given class of chemical reactions are correlated. When published data is unavailable, rates have been determined by analogy to other reactions. The underlying rates used in these analogies are consistent throughout the

mechanism. As an example, the rate of H-abstraction from a methyl group in toluene and in xylene are taken in analogy to the same reaction and are not independently adjusted. Third, none of the reaction rates has been fitted to match experimental data. All kinetic rate data are consistent with published literature. Note that while this mechanism is developed to describe combustion of several components, which might be crucial for surrogates of realistic transportation fuels, blends of fuels have not been validated here. The term consistent therefore does not refer to the interactions of oxidation reactions of different fuels.

The reaction rate parameters used in the mechanism are obtained from quantum chemical calculations reported in the literature or from experimental measurements from the literature when available. In certain cases, the reaction rates are adapted from the rates of reactions of the smaller hydrocarbon species, which for consistency have been taken from the base mechanism described by Blanquart *et al.* [68].

### Xylene Oxidation

The chemistry of dimethylbenzene or xylene ( $A_1(CH_3)_2$ ) oxidation in this reaction scheme is mostly based on the chemistry of toluene. The reaction scheme has been developed for *m*-xylene oxidation, and the reaction pathways included are primarily those of importance to *m*-xylene. The main reaction pathways involving the radicals and stable intermediates formed during the oxidation of xylene are shown in Fig. 31.

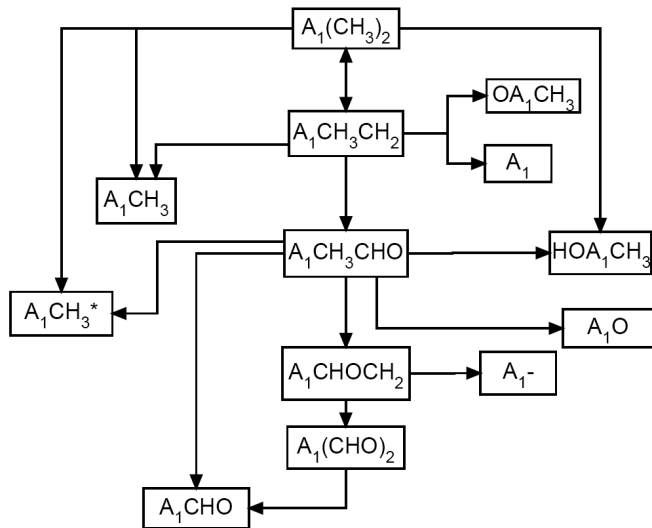


Figure 31: Reaction pathway for *m*-xylene oxidation.

### Xylene Decay And Xylyl Decomposition

Following Emdee *et al.* [82], *m*-xylene is oxidized by sequential reaction and removal of the methyl side chains. Abstraction of a benzylic H from xylene forms the xylyl (methylbenzyl)

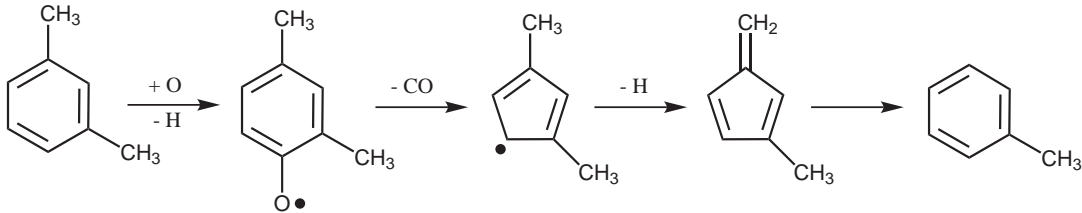
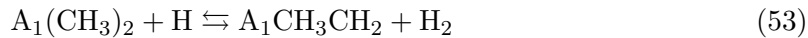


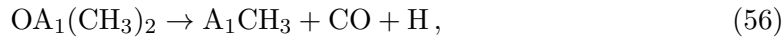
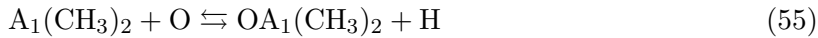
Figure 32: O attack on the aromatic ring of xylene.

radical ( $A_1CH_3CH_2$ ) and the substitution of a methyl group by an H atom produces toluene and a methyl radical



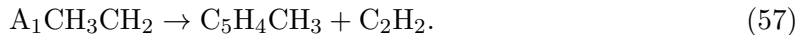
Substitution of a methyl group in xylene by an OH radical leads to the formation of cresols ( $HOA_1CH_3$ ). Xylene also leads to the formation of methylphenyl radicals upon loss of a methyl group.

An O atom attack on xylene leads to the formation of a dimethylphenoxy radical ( $OA_1(CH_3)_2$ ), the bi-substituent analogue of cresoxy. In the present work,  $OA_1(CH_3)_2$  is assumed to form toluene with the loss of CO and H atoms (see Fig. 32). However, we have not included the  $OA_1(CH_3)_2$  species and the intermediates in the pathway. Instead, we have laid out a direct pathway to form toluene from an O attack on xylene assigning the full entrance channel rate to the products. Bypassing this intermediate oxygenated species is supported by the work of Shaddix *et al.* [77], who observed for the 1-methylnaphthalene + O reaction that the intermediate  $OA_2CH_3$  is short-lived. The direct pathway laid out to form the products in the above reactions is further justified by results that we obtained by simulations with a more complete representation of this pathway. No differences were observed in the results when the intermediate oxygenated species shown in the xylene + O pathway ( $OA_1(CH_3)_2$ ) was introduced in the mechanism, as



where the reaction rates for these reactions were adapted from those of the reactions of benzene + O and  $A_1O$  forming  $C_5H_5$  + CO.

The xyl radical undergoes reactions similar to those of the benzyl radical. The principal decomposition pathway is shown in Fig. 33. Unimolecular decomposition of the xyl radical results in the formation of methylcyclopentadienyl radical ( $C_5H_4CH_3$ ) and acetylene ( $C_2H_2$ )



The methylcyclopentadienyl radical ( $C_5H_4CH_3$ ) formed here is analogous to the cyclopentadienyl radical ( $C_5H_5$ ) formed in benzyl radical decomposition. Emdee *et al.* [82] proposed

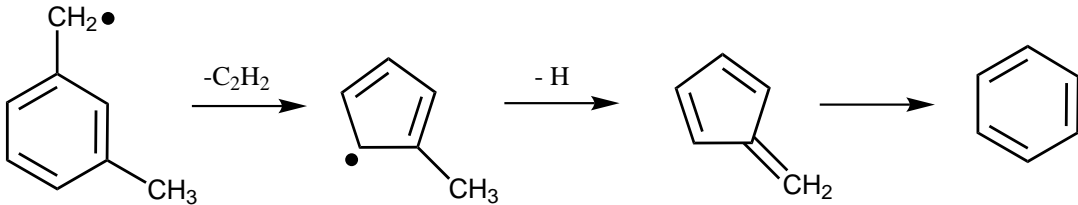


Figure 33: Decomposition of xylyl radical.

Reactions	A	n	E
$A_1CH_3CH_2 + O \rightarrow A_1CH_3CHO + H$	$4.37 \cdot 10^{18}$	-1.34	6.66
$A_1CH_3CH_2 + O \rightarrow A_1CH_3^* + CH_2O$	$5.99 \cdot 10^{23}$	-2.47	67.75
$A_1CH_3CH_2 + O \rightarrow A_1CH_3 + HCO$	$1.97 \cdot 10^{22}$	-2.36	34.11
$A_1CH_3CH_2 + O_2 \rightarrow A_1CH_3CHO + OH$	$1.38 \cdot 10^2$	+2.42	31.13
$A_1CH_3CH_2 + O_2 \rightarrow OA_1CH_3 + CH_2O$	$6.57 \cdot 10^3$	+1.87	20.93

Table 3: Reactions whose rates have been derived. Refer to text for details. Rate coefficients in Arrhenius form ( $k = AT^n \exp(-E/RT)$ ); Units are  $cm^3$ , K, mol, s and kJ.

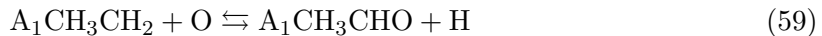
a fast rearrangement of the methylcyclopentadienyl radical to give benzene and H atom.



A global reaction has been proposed in the current mechanism for the unimolecular decomposition of the xylyl radical forming benzene, acetylene, and H atom. Such a global reaction has also been used in the work of Battin-Leclerc *et al.* [73]. However, for consistency with the toluene chemistry, the rate assigned to xylyl radical decomposition is that of the unimolecular decomposition of benzyl radicals [83] used in the present mechanism.

#### Successive Oxidation Of The Methyl Groups

The xylyl radical reacts with an O atom to form the  $A_1CH_3CH_2O$  species which decomposes to give tolualdehyde, toluene, and methylphenyl radicals in a manner similar to the reactions of benzoxy radical ( $A_1CH_2O$ ) in toluene oxidation



The species  $A_1CH_3CH_2O$  is assumed to rapidly decompose into products and has been bypassed in the  $A_1CH_3CH_2 + O$  reaction. The reaction rates for the overall reactions have been derived using the corresponding reaction rates of the O attack on benzyl radical and the decomposition of the benzoxy radical ( $A_1CH_2O$ ), assuming that the  $A_1CH_3CH_2O$  species exists in quasi steady state. The reaction rates derived here are presented in Table 3.

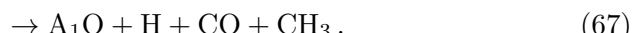
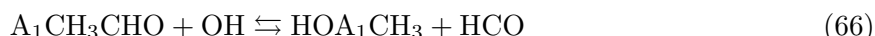
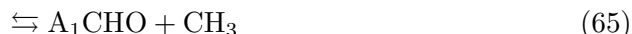
The reaction of molecular oxygen with a xylyl radical forms a methylbenzylperoxy radical which further decomposes into tolualdehyde ( $A_1CH_3CHO$ ) or a cresoxy species in a manner similar to the reactions of the benzyl radical



In determining the rates for this reaction, an approach similar to that for the benzyl +  $O_2$  reaction is used. Canneaux *et al.* [84] computed the rate constant for the four-centered isomerization of the methylbenzylperoxy radical to form the methyl(hydroperoxy)benzyl radical using an elaborated CASPT2 method. This isomerization reaction is the rate determining step for the formation of tolualdehyde from methylbenzylperoxy radicals. Murakami *et al.* [85] performed a study at the CBS-QB3 level of theory to compute the rate constants and product branching ratios for *o*-xylyl +  $O_2$  and its subsequent reactions.

The individual reaction rates to directly form tolualdehyde and cresoxy species from xylyl +  $O_2$  are obtained assuming the methylbenzylperoxy radical to exist in quasi-steady state. In this calculation, the forward and the backward reaction rates of xylyl +  $O_2$  forming methylbenzylperoxy radical, and the reaction rate to form cresoxy species from methylbenzylperoxy radical are obtained from Murakami *et al.* [85], assuming the rates are roughly the same for both *m*-xylene and *o*-xylene; the reaction rate for the conversion of methylbenzylperoxy to tolualdehyde is derived from Canneaux *et al.* [84]. The final rate constant for the formation of tolualdehyde was found to be slightly smaller than that for benzyl (about 30% lower). Given the sensitivity of the results to this rate constant, it was found very important to evaluate this reaction rate.

The reactions of tolualdehyde are based on the reactions of toluene and benzaldehyde. The methyl side chain of tolualdehyde reacts like the methyl group on toluene to give methoxybenzyl ( $A_1CHOCH_2$ ) radicals. The formyl (-CHO) side chain of tolualdehyde reacts like the -CHO group on benzaldehyde to give methylphenyl radicals. Tolualdehyde can lead also to the formation of toluene, benzaldehyde, cresol, and phenoxy species via substitution of the side chain groups (-CH<sub>3</sub>, -CHO) by H and OH radicals



The methoxybenzyl radical ( $A_1CHOCH_2$ ) formed from tolualdehyde undergoes reactions similar to the benzyl radical. The primary product of the attack of an O atom on the methoxybenzyl radical is phthalaldehyde ( $A_1(CHO)_2$ ). Other pathways for the same reaction lead to the formation of benzaldehyde and phenyl radicals analogous to the O atom attack on benzyl radicals.

Finally, phthalaldehyde is consumed by reactions similar to those of benzaldehyde. Following the abstraction of an H atom, phthalaldehyde forms the  $A_1CHOCO$  species, which fur-

Ignition delay times	Plug flow reactors	Burning velocity
Battin-Leclerc <i>et al.</i> [73]		Johnston and Farrel [88]
Gail <i>et al.</i> [86, 75]	Emdee <i>et al.</i> [82]	Egofopoulos <i>et al.</i> [89]
Shen <i>et al.</i> [87]		

Table 4: Validation cases for *m*-xylene undertaken in the present study.

ther forms benzaldehyde with the loss of CO. Substitution of the -CHO group on phthalaldehyde by H forms benzaldehyde and substitution by OH is assumed to form phenoxy radicals. With these reaction pathways, the oxidation of xylene, hereafter reduces to the oxidation of toluene and its derivative species which has been discussed in detail in Narayanaswamy *et al.* [80].

### Validation Tests For *m*-Xylene

Table 4 lists the validation cases considered for *m*-xylene in the present study. The different experimental setups used for the validation of the present mechanism were chosen based on their relevance to the modes of combustion typically found in realistic engines.

Experimental data for the oxidation of aromatic fuels under engine conditions (high pressure) are limited. As a result, most of the validation cases have been performed at atmospheric pressure. While the chemical model has been validated extensively and under a large range of conditions, there remain some uncertainties on the behavior of the model in more realistic conditions.

#### *Ignition Delay Results*

Comparison of modeled results with the experimentally measured ignition delay times for xylene isomers are presented next. In all our computations, the ignition delay times are defined in the same way as in the respective experimental studies.

Battin-Leclerc *et al.* [73] performed shock tube ignition measurements for all three isomers of xylene at reflected shock conditions of 1330 to 1800 K, 6.7 to 9 bar,  $\phi = 0.5$  to 2.0, and 92 to 98% argon dilution. They note that the three isomers show almost identical reactivity at the experimental conditions investigated. The ignition delay time was defined based on the 10% rise in the OH radical emission. Accordingly, our computations use the time to reach 10% of the maximum OH concentration to indicate the ignition delay time. The comparison between the computed ignition times and the experimental data for *m*-xylene is shown in Fig. 34(a).

As shown, the computed ignition delay times follow the experimental measurements at  $\phi = 2.0$  and those at  $\phi = 1.0$  except at very high temperatures, while they are slower than the experiments at lean conditions. To better understand the results and properly estimate the performance of the present chemical model, we found it beneficial to consider also the auto-ignition behavior of the other xylenes isomers.

Gail *et al.* [75] measured ignition delay times of *o*-xylene at similar temperatures and fuel

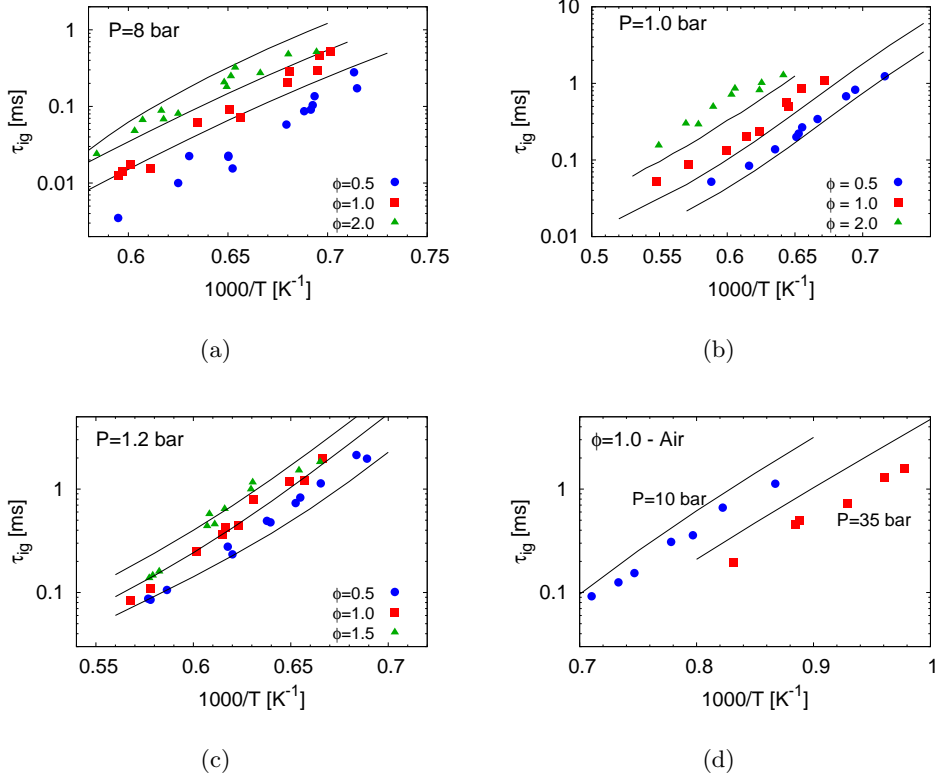


Figure 34: Ignition delay times of xylenes. Symbols - experiments; (a) *m*-xylene: Battin-Leclerc *et al.* [73]; (b) *o*-xylene: Gail *et al.* [75]; (c) *p*-xylene: Gail *et al.* [86]; (d) *m*-xylene: Shen *et al.* [87]; solid lines - results from numerical simulations.

concentrations as investigated by Battin-Leclerc *et al.* [73] but at close to atmospheric pressure. The ignition delay time definition in these experiments and the present computations are based on the time for the maximum rate of rise of CH radical emission. Figure 34(b) shows the comparison between the present computed ignition delay times for *m*-xylene and the experimental measurements. Note that these are two different isomers and that the present comparison is only motivated by the observation that all the three isomers of xylene show similar reactivity at these high temperatures [73]. From the figure, it is seen that the ignition delay times predicted by the mechanism are faster than the experiments, in contrast to the comparison with the data of Battin-Leclerc *et al.* [73].

Much closer agreement at equivalence ratios of 1.0 and 1.5 is seen in Fig. 34(c) where the computed ignition delay times for *m*-xylene are compared with the ignition delay times for *p*-xylene measured by Gail *et al.* [86] at similar temperature ranges and pressures spanning 1 to 1.4 atm. In effect, the computed ignition delay time plots show approximately the same slope for the different experimental data sets at the studied high temperatures and stoichiometric conditions. However, the magnitudes of the ignition delay shows some differences.

Finally, Shen *et al.* [87] measured ignition delay times for the three isomers of xylene at lower temperatures (941-1408 K) and higher pressures (9-45 atm) at equivalence ratios of 0.5 and 1.0. Figure 34(d) shows the comparison between the computed ignition delay times and the experimental data. The ignition delay times are slightly overpredicted by the present computations at both 10 bar and 35 bar pressure, though the slope of the variation is predicted closely. However, the predictions are much closer to the experiments at 10 bar when compared to those at the higher pressure of 35 bar. This trend is consistent with that observed for toluene ignition at elevated pressures. This could be expected because the xylene oxidation is mostly based on the toluene chemistry.

From the extensive comparison of ignition delay times for all three isomers at various temperatures, pressures, and equivalence ratios, it is possible to draw several conclusions about the performance of the chemical model. The mechanism seems to predict consistently longer ignition delay times than measured for *m*-xylene at elevated pressures (from 8 bar to 35 bar). On the other hand, at atmospheric pressure, the predicted ignition delay times are shorter than measured experimentally for *o*-xylene and *p*-xylene. These results are surprising, for the ignition delay times of *o*-xylene are expected to be similar or shorter than those of *m*-xylene under these conditions. In the absence of data for *m*-xylene ignition at atmospheric pressure, it is difficult to explain unequivocally the observed discrepancies.

### Results For Plug Flow Reactor Experiments

Concentration profiles of the fuels and their derivatives are validated against PFR experimental data next. The time shifts applied to the experimental data (in order to define zero time) have been indicated in the plots.

Emdee *et al.* [82] conducted atmospheric flow reactor tests with *m*-xylene and *p*-xylene at temperatures ranging from 1093 K to 1199 K and equivalence ratios from 0.47 to 1.7. They estimate an uncertainty in mole fractions of  $\pm 5\%$  for non-aromatic carbon-containing species and  $\pm 10\%$  for aromatics in their data. The uncertainty in  $H_2$  is expected to be  $\pm 100$  ppm and  $\pm 5\%$  for  $O_2$  measurements. An absolute uncertainty of  $\pm 10$  K is expected in measured temperature.

The PFR simulation results obtained for *m*-xylene from the present scheme are validated against the set of experimental data for *m*-xylene available from Emdee *et al.* [82]. Figure 35 shows the comparison at stoichiometric conditions, 1155 K, and 1 atm.

The fuel (*m*-xylene) decay follows the experimental measurements closely. The predictions remain well within the experimental uncertainty throughout. The decay pathways of *m*-xylene are similar to those of toluene. The primary path of consumption is via H atom abstraction from the methyl side chain of *m*-xylene forming methylbenzyl radicals. Substitution of a methyl group in *m*-xylene by an H atom leading to the formation of toluene contributes roughly 15% to the fuel decay. However, from a reaction flux analysis, this reaction is found to be primarily responsible for all the toluene found during *m*-xylene oxidation. Figure 35a shows the the computed profile of toluene in comparison with the experiments. Toluene leads to the formation of benzyl radicals, which on combining with methyl radicals form ethylbenzene. The computed profile of ethylbenzene in *m*-xylene oxidation is shown

in Fig. 35(b).

Most of the methylbenzyl radicals formed from *m*-xylene result in the formation of tolualdehyde via reactions described earlier in the article. Figure 35(c) shows that the concentration profiles of tolualdehyde and benzaldehyde are in very good agreement with the experiments. About 70% of tolualdehyde forms methylphenyl ( $A_1CH_3^*$ ) radicals. It was found to be highly important to include the reaction pathways that involve formation of methylphenyl radicals from tolualdehyde in order to describe the oxidation of *m*-xylene fairly accurately. The methylphenyl radical further forms cresoxy species and fulvene and eventually leads to the formation of benzene. Figure 35(d) shows the comparison between the computed profile for benzene and the experimental measurements. The differences observed in the benzene profile could be attributed to some of the global reactions used in the mechanism.

The concentration profiles of some of the smaller hydrocarbons are also compared with the experiments. The  $C_2H_2$ ,  $CH_4$ , and  $H_2$  profiles (Figs. 35(d), 35(e)) agree fairly well with the experiments. The profile of CO formation (Fig. 35(f)) and oxidizer decay (Fig. 35(g)) are also seen to agree closely with the experimental measurements.

### Laminar Flame Speed Results

In this section, zero stretch burning velocity data computed for *m*-xylene are compared with available experimental data.

The burning velocities of *m*-xylene at different temperatures computed using the present oxidation model are compared with the experimental burning velocity measurements for *m*-xylene made by Johnston and Farrel [88] in Fig. 36(c). It can be seen that the computed burning velocities are higher than those reported in the experiments. However, such a trend was observed earlier when comparing the burning velocities of benzene [68] and toluene (Fig. 36(a)) and ethylbenzene (Fig. 36(b)) with the data of Johnston and Farrel. Therefore, it was found essential to validate against other published data for *m*-xylene burning velocities.

More recently, Ji *et al.* [89] measured laminar flame speeds and extinction rates of *m*-xylene as a function of equivalence ratio at elevated temperatures and atmospheric pressure. Experiments were performed in the counterflow configuration and the flow velocities were measured using Laser Doppler Velocimetry. The unstretched laminar burning velocity is determined by a linear extrapolation of the flame speed versus strain rate curve. The uncertainty in the experiments are about 2 to 3 cm/sec.

Figure 36(c) shows the comparison between the burning velocities computed using the present reaction mechanism and the experimentally measured values. It can be noted that our computed values are lower than those reported experimentally by about 2 to 4 cm/s. Ji *et al.* [89] also report the burning velocities of other fuels. Their non-linearly extrapolated burning velocities are found to be lower than the linearly extrapolated values at all equivalence ratios by about 4-5 cm/sec. This could account for the observed differences in our results. It would be interesting to compare our computed results with the non-linearly extrapolated burning velocities for *m*-xylene.

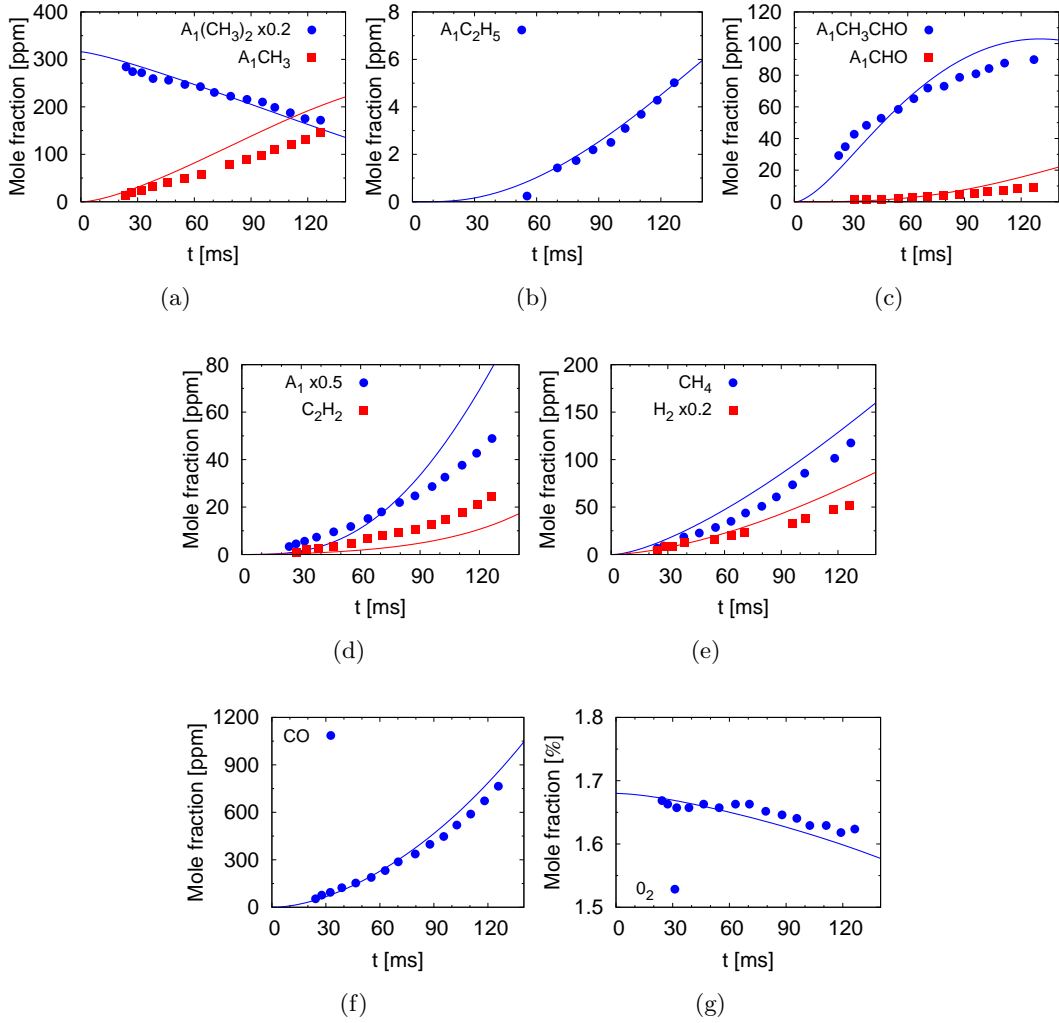


Figure 35: PFR data for *m*-xylene at 1155 K, symbols - experiments: Emdee *et al.* [82]; solid lines - numerical simulations; shift: 20 ms.

In all, with the extensive validation undertaken in the present study, the overall ability of the model to predict the oxidation of *m*-xylene has been found to be very good given the fact that a single and consistent chemical model is used to describe the oxidation of a large range of species. Similar satisfactory agreement was also obtained for the other substituted aromatics under consideration, namely, toluene, ethylbenzene, styrene, and  $\alpha$ -methylnaphthalene. More extensive validation tests for these substituted aromatic species are presented in Narayanaswamy *et al.* [80].

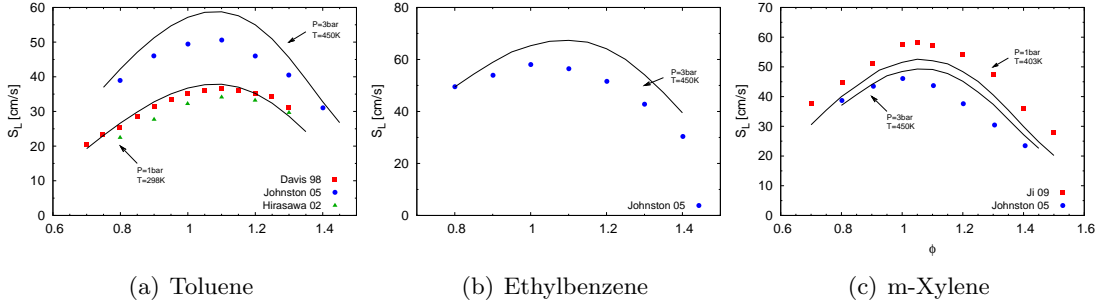


Figure 36: Laminar burning velocity: symbols - experiments; solid lines - numerical results.

### 3.3.2 Extension To *n*-Dodecane

Several detailed mechanisms for *n*-dodecane exist in literature. Dahm *et al.* [90] and later Herbinet *et al.* [91], developed a detailed mechanism for *n*-dodecane, and were able to predict the results of pyrolysis experiments and thermal decomposition in a jet-stirred reactor. Ranzi *et al.* [92] proposed and validated a lumped mechanism for *n*-alkanes including *n*-dodecane for low to high temperature oxidation in various configurations. You *et al.* [93] proposed a detailed kinetic model for normal alkanes up to *n*-dodecane above 850 K. They validated their kinetic model against laminar flame speeds, and ignition delays behind reflected shock waves, with *n*-dodecane being the emphasis.

JetSurF v2.0 [94] is an ongoing effort for jet fuel surrogate mechanism development that includes oxidation of *n*-dodecane at moderate to high temperatures.

Of particular interest to this work is the detailed mechanism proposed by Westbrook *et al.* [95], which includes high and low temperature pathways to describe the pyrolysis and oxidation of several *n*-alkanes up to *n*-tetradecane. As this mechanism was built based on well-established reaction classes originally developed for *n*-heptane, it has been chosen as the starting point for our approach. This scheme for *n*-dodecane is first reduced to a skeletal level, and then incorporated in the base mechanism, now extended to aromatics, as described in the previous section. The methodology is discussed next, followed by a demonstration of the performance of the combined mechanism for different targets.

### Mechanism Development

The reference mechanism for *n*-dodecane oxidation from Westbrook *et al.* [95], referred below as the LLNL mechanism, has 16313 forward and reverse reactions among 2112 species. First, this extensive mechanism is reduced to a skeletal level using a multi-stage reduction strategy put forth by Pepiot-Desjardins and Pitsch, involving species and reaction elimination using the DRGEP approach [60], and chemical species lumping [61]. The database used to carry out the reduction includes plug flow reactor-like configurations, and ignition delays for low to high temperatures (600–1500 K), pressures from 1 to 40 atm, and equivalence ratios from 0.5 to 1.5.

The skeletal mechanism for *n*-dodecane that is obtained from the application of the

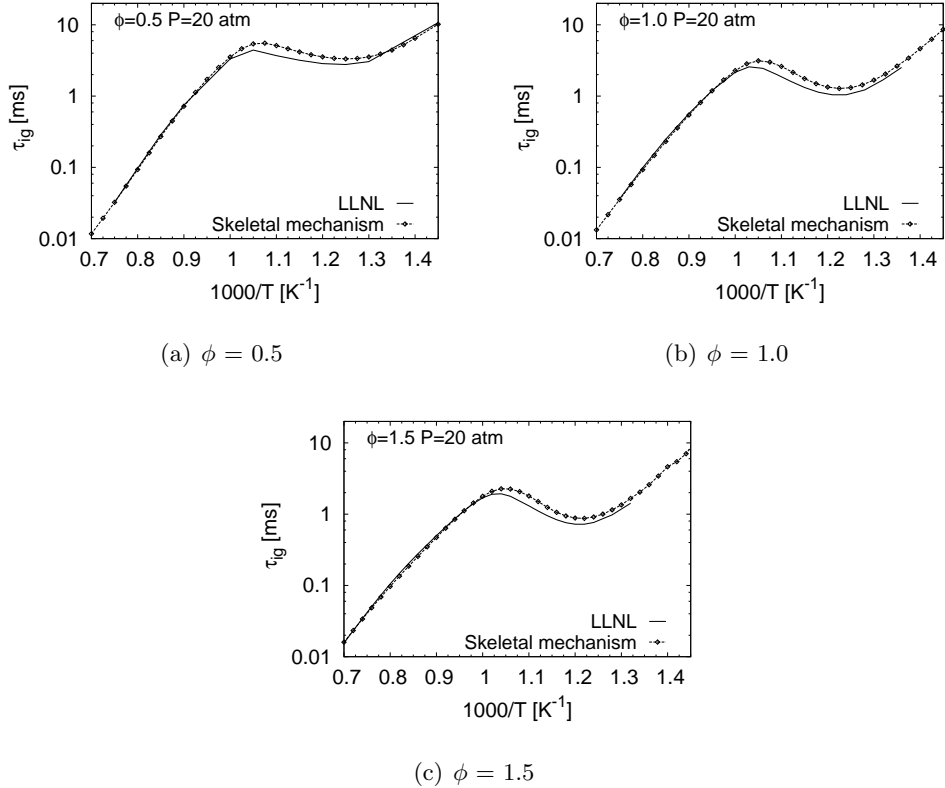


Figure 37: Ignition delay times of *n*-dodecane/air, comparing the skeletal level mechanism with the detailed mechanism results; solid lines - detailed mechanism: Westbrook *et al.* [95] (LLNL).

DRGEP approach consists of 862 reactions among 156 species. Figure 37 compares ignition delay times computed using the detailed and skeletal schemes for lean, stoichiometric and rich *n*-dodecane/air mixtures at 20 atm. The skeletal mechanism provides very good predictions in the low ( $T < 850$  K) and high ( $T > 1000$  K) temperature regions. The skeletal mechanism predicts slightly longer ignition delays in the Negative Temperature Coefficient (NTC) region. However, considering the high reduction ratio that was achieved ( $\sim 95\%$ ) and the small magnitudes of the errors, this skeletal scheme is treated as acceptably accurate and is used in the subsequent mechanism development steps.

The merging of the *n*-dodecane with the base mechanism (including aromatics) is accomplished using an interactive tool [96] that automatically identifies common species and reactions from the different mechanisms, and incompatibilities between the kinetic data sets. To ensure a smooth and consistent merging, (a) Rate conflicts detected during the merging were always resolved in favor of the thoroughly validated base mechanism, therefore leaving this mechanism virtually unchanged, and (b) Repeated/redundant reaction pathways, described as elementary steps in the base mechanism while global in the *n*-dodecane sub-mechanism, or vice versa, were removed from the incremental *n*-dodecane sub-mechanism.

Shock tubes		Burning velocity
Ignition delays	Species profiles	
Davidson <i>et al.</i> [97]		Kumar and Sung [100]
Vasu <i>et al.</i> [64]	Davidson <i>et al.</i> [99]	Ji <i>et al.</i> [101]
Shen <i>et al.</i> [98]	Vasu <i>et al.</i> [64]	Kelley <i>et al.</i> [102]
Davidson <i>et al.</i> [99]		

Table 5: Validation cases for *n*-dodecane undertaken in the present study.

The combined mechanism thus retains the rates in the base model.

The resulting combined mechanism includes oxidation pathways of *n*-dodecane at a variety of temperatures. These pathways provide additions to several hydrocarbon oxidation pathways already described in the base mechanism. The incremental *n*-dodecane sub-mechanism consists of 267 reactions among 78 species, some of which are lumped. A few reaction rate changes have been introduced to improve the performance of the mechanism under different idealized configurations as described next. The validation tests for the substituted aromatics presented in our earlier work [80] have been repeated using the combined mechanism, and found to produce negligible changes in results.

### Validation Tests For *n*-Dodecane

The validation cases to evaluate the mechanism focus on oxidation, and include ignition delays spanning wide ranges of temperatures and pressures, species concentration profiles measured in shock tubes, and burning velocities obtained at different pressures. Fuel pyrolysis and transport dominated configurations are not tested. The list of all validation cases examined for *n*-dodecane are summarized in Table 5.

#### *Ignition Delay Results*

Ignition delays are computed using a isochor homogeneous reactor configuration, using the same ignition criterion as in the experiments.

#### *n*-Dodecane/Air Mixtures

Vasu *et al.* [64] measured ignition delays of *n*-dodecane/air mixtures over 727–1422 K, 15–34 atm, and  $\phi=0.5, 1.0$ . Their experimental data scaled to 20 atm, and the ignition delays computed using the present mechanism (labelled p.w.) at 20 atm, 600–1500 K are shown in Fig. 38. Some improvement over the original LLNL mechanism predictions is seen, due to different  $\text{H}_2/\text{O}_2$ ,  $\text{C}_1\text{--C}_4$  chemistry in the present base model.

Further, H-abstraction from *n*-dodecane by  $\text{CH}_3\text{O}_2$  was introduced in the combined mechanism. This abstraction was analogous to a similar iso-octane reaction pathway in the base model, with reaction rates adapted from Carstensen *et al.* [103]. This introduction led to faster ignition at  $T > 900$  K. However, some differences are observed in the NTC region. A sensitivity analysis reveals that the H-abstraction rate from the fuel by  $\text{HO}_2$  is key in

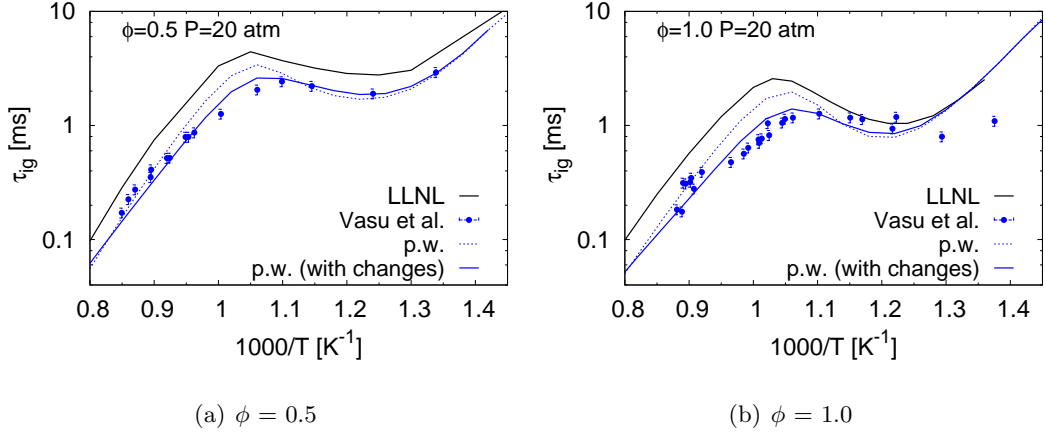
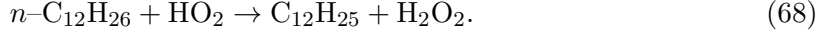


Figure 38: Ignition delay times of *n*-dodecane/air mixtures; symbols - experiments: Vasu *et al.* [64].

determining the ignition delays around 1000 K:



Alkene plus HO<sub>2</sub> reactions were examined and found to have negligible effect on the ignition delays, therefore ruling out some missing consumption pathways involving HO<sub>2</sub> in the mechanism and prompting a more thorough investigation of reaction (68).

While a direct evaluation of this reaction rate for *n*-dodecane is unavailable in the literature, it can be estimated from kinetic evaluations available for smaller carbon alkanes. The quantum chemical calculations by Carstensen *et al.* [103] and Aguilera-Iparraguirre *et al.* [104] provide the reaction rates for H-abstraction by HO<sub>2</sub> from primary and secondary carbons in *n*-butane, the latter study using a more accurate theory than the former. By scaling these rates to account for the number of primary and secondary carbons in *n*-dodecane, as compared to *n*-butane, two possible reaction rates for reaction (68) can be obtained. These rates vary over a factor of 2 to 7 at different temperatures, with the rate from Carstensen *et al.* being higher. The difference is attributed to the different levels of theory used in these studies [104]. For best agreement with experimental data, a reaction rate which is 1.7 times that suggested by Aguilera-Iparraguirre *et al.*, well within the uncertainty range, is chosen here.

The ignition delays obtained with the modified reaction (68) are added to Fig. 38, and are labeled as “p.w. (with changes).” As expected, the agreement between the computed lines and the experiments has improved significantly in the NTC region, with minimal changes at high and low temperatures. Finally, the mechanism captures the low temperature data (T < 850 K) at  $\phi=0.5$ , but not at  $\phi=1.0$ . This will further be investigated when more measurements at such low temperatures become available.

Ignition delays for *n*-dodecane/air mixtures were also measured by Shen *et al.* [98] at 14 and 40 atm, 900–1300 K, and  $\phi=0.5, 1.0$ . In Fig. 39, a comparison of the ignition delays

between simulations and experiments shows some differences in all cases for  $T < 1050$  K, with an over-prediction at 14 atm, and under-prediction at 40 atm.

A more comprehensive comparison can be obtained by scaling Vasu *et al.* [64] 20 atm data down to 14 atm and up to 40 atm using the  $P^{-1}$  scaling law, used by both groups to scale data to a common pressure. At 14 atm,  $T > 1000$  K and  $\phi=0.5$  (Fig. 39(a)), the previously observed discrepancies between experiments and simulations can be traced to potential outliers in the Shen *et al.* data in this region. At high temperatures and pressures, the computed results are within the experimental uncertainty and variability of the combined experimental data.

Note that the inverse pressure law used to scale the experimental data is appropriate only in the high temperature region ( $T > 1000$  K). The strongly pressure dependent peroxy pathways, dominant in the NTC region, would call for a stronger relation,  $\sim P^{-a}$ , where  $a>1$  [105], which would significantly improve the agreement between the scaled data of Vasu *et al.* and the computations.

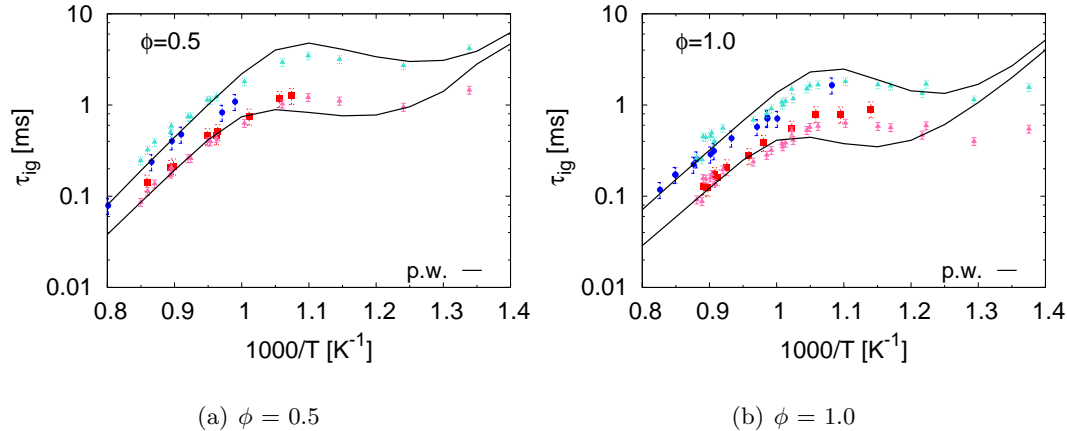


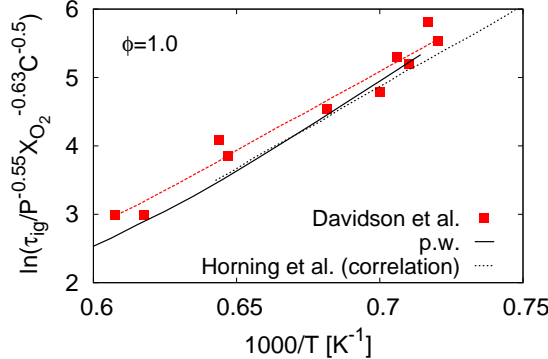
Figure 39: Ignition delays of *n*-dodecane/air mixtures; symbols - experiments: Shen *et al.* [98] at  $P=14$  atm and 40 atm (blue circles and red squares respectively); Vasu *et al.* [64] data at 20 atm is scaled to 14 atm and 40 atm (cyan and pink triangles respectively) using  $P^{-1}$  scaling (see text).

### *n*-Dodecane/O<sub>2</sub>/Argon Mixtures

Davidson *et al.* [99] and Vasu *et al.* [64] measured low fuel concentration ignition times of *n*-dodecane/O<sub>2</sub>/argon mixtures at  $\phi=1.0$ ,  $P=2.25$  atm, and  $\phi=0.5$ ,  $P=15$  atm respectively, for  $T > 1100$  K. Davidson *et al.* [97] also measured ignition delays of *n*-dodecane/O<sub>2</sub>/Argon mixtures in an aerosol shock tube, at  $\phi=0.5$  and  $P=6.7$  atm.

To evaluate the performance of the mechanism at those different experimental conditions in a consistent fashion, the correlation developed by Horning *et al.* [106] for ignition delay times of stoichiometric *n*-alkane/O<sub>2</sub>/Argon mixtures is considered:

$$n\text{-alkane} (\phi = 1.0) : \tau = 9.4 \times 10^{-12} P^{-0.55} X_{O_2}^{-0.63} C^{-0.50} \exp(46, 550/RT), \quad (69)$$



(a)  $X_{fuel}^0 = 400$  ppm

Figure 40: Low fuel concentration ignition delays of *n*-dodecane/O<sub>2</sub>/argon mixtures at  $\phi=1.0$ ; symbols - experiments: Davidson *et al.* [99]. The experimental data, the least square fit to the experimental data (red dashed line) and the computed ignition delays are scaled according correlation from Horning *et al.* [106].

where ignition delays are in microseconds, pressure is in atmospheres, X<sub>O<sub>2</sub></sub> is the oxygen mole fraction, C is the number of carbons in the fuel molecule, and the activation energy is in cal/mole. This correlation was obtained from their experimental data of propane, *n*-butane, *n*-heptane, *n*-decane, for P=1–6 atm, T = 1315–1560 K, and X<sub>O<sub>2</sub></sub> = 2%–20%.

The experimental conditions of Davidson *et al.* [99],  $\phi=1.0$ , P=2.25 atm, T=1388–1660 K, X<sub>O<sub>2</sub></sub>=0.75% fall roughly within this validity range. In Fig. 40, the experimental ignition delays measured by Davidson *et al.* [99] and the computed ignition delays have been scaled according to equation (69), by assuming that it holds true for *n*-dodecane as well. The computations agree well with this correlation, though there are differences when compared to the scaled experimental data. While the definition of ignition criterion used by Horning *et al.* (time to reach peak CH\* concentration) and Davidson *et al.* (time to reach 50% peak OH concentration) are different, this should not introduce >10% difference in ignition delays. Consequently, the computed ignition delays appear satisfactory for the experimental conditions studied.

Ignition delays of lean *n*-dodecane/O<sub>2</sub>/Argon mixtures are discussed next. Vasu *et al.* [64] measured ignition delays at low fuel concentrations: X<sub>n-C<sub>12</sub>H<sub>26</sub></sub> = 1000 ppm, 750 ppm, 514 ppm; X<sub>O<sub>2</sub></sub>=10%, P=15 atm,  $\phi=0.5$ , and T=1250–1400 K. To complement the small number of experimental data points, ignition delays of other *n*-alkane/O<sub>2</sub>/argon mixtures at similar conditions, expected to show similar ignition characteristics [98], have been included. The experimental data for ignition delays of *n*-heptane/O<sub>2</sub>/Argon mixtures from several groups [106, 107, 108] at different experimental conditions, included in the study of Horning *et al.* have been scaled to 15 atm and X<sub>O<sub>2</sub></sub>=10%, using P<sup>-0.55</sup> and X<sub>O<sub>2</sub></sub><sup>-0.63</sup> from correlation (69) discussed above, which has been found to be true for  $\phi=0.5$  as well [106]. Again, eq. (69) is assumed to be valid for these conditions.

In Fig. 41, a comparison of the computed ignition delays with those measured by Vasu

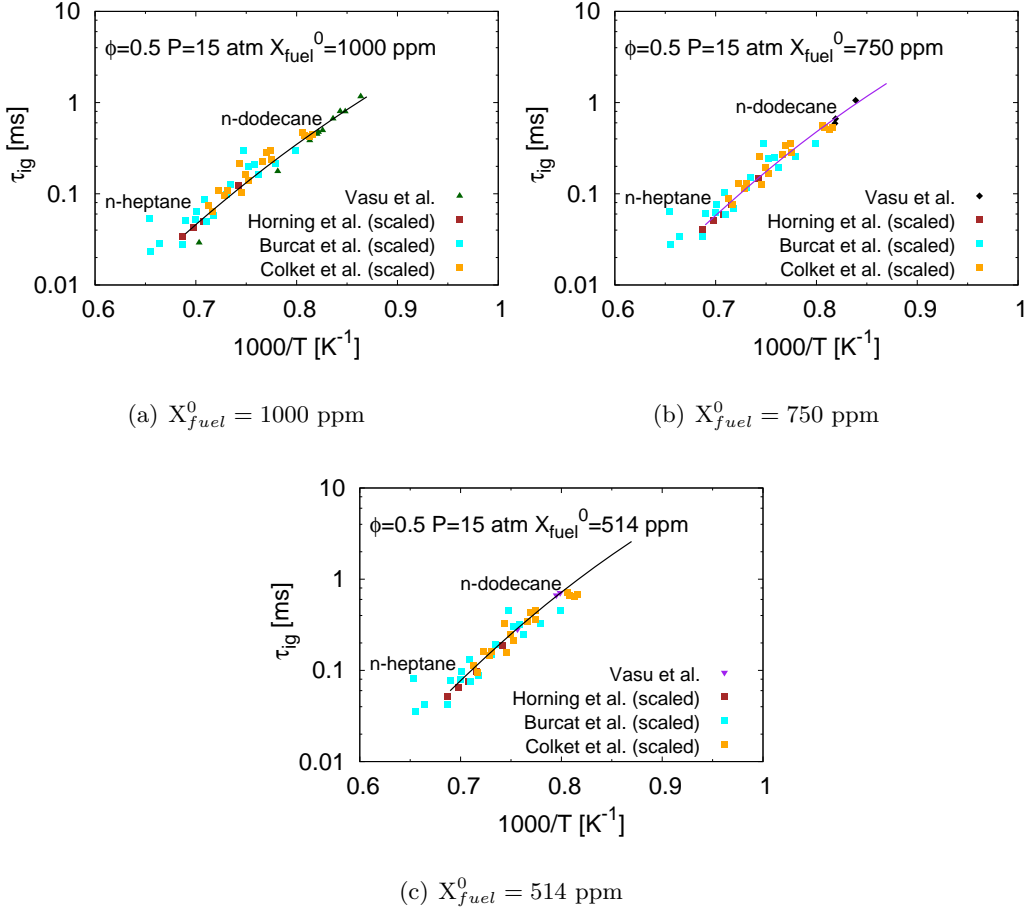


Figure 41: Low fuel concentration ignition delays of *n*-dodecane/O<sub>2</sub>/argon at  $\phi=0.5$ , P=15 atm; solid line - present work; symbols - experimental data [64, 106, 107, 108]. Experimental data for *n*-heptane/O<sub>2</sub>/argon mixtures are scaled to the experimental conditions using correlation from Horning *et al.* [106].

*et al.* shows good agreement wherever data are available, except at  $1000/T = 0.7\text{ K}^{-1}$ ,  $X_{n\text{-C}_{12}\text{H}_{26}}=1000$  ppm. However, when appraising the computed results together with the scaled ignition data for *n*-heptane, it can be concluded that the slopes of the computed ignition delays are consistent with the scaled data, for all fuel concentrations.

Another set of data for ignition delays of lean *n*-dodecane/O<sub>2</sub>/Argon mixtures measured in an aerosol shock tube facility, at 6.7 atm,  $\phi=0.5$ , T=1050–1330 K comes from Davidson *et al.* [97]. In Fig. 42, a comparison of the ignition delays of *n*-dodecane between the simulations and experiments shows wide disagreement. However, in conjunction with the ignition delay data for *n*-heptane scaled to these experimental conditions, a few comments can be made.

Ignition delays for *n*-alkanes are expected to decrease as the size of the alkane increases.

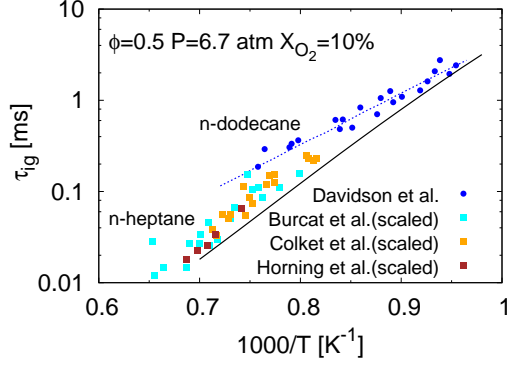


Figure 42: Ignition delay times of *n*-dodecane/O<sub>2</sub>/argon mixtures at P=6.7 atm,  $\phi=0.5$ ; solid line - present work; symbols - experimental data [97, 106, 107, 108]; dotted line - fit to Davidson *et al.* data. Experimental data for *n*-heptane/O<sub>2</sub>/argon mixtures are scaled to the experimental conditions using correlation from Horning *et al.* [106].

Accordingly, the computed *n*-dodecane ignition delays are shorter than the scaled ignition delay data of *n*-heptane throughout the high temperature region, which is not the case for the experimental *n*-dodecane ignition data. Secondly, the slope of the computed ignition delays is consistent with the scaled *n*-heptane data, which is not the case for the *n*-dodecane data points (shown in Fig. 42). From the extensive discussions, consistency checks and the range of validation tests studied, the present mechanism predicts the ignition delays of *n*-dodecane fairly satisfactorily.

#### Species Time History Results

Davidson *et al.* [99] measured concentration profiles of *n*-C<sub>12</sub>H<sub>26</sub>, C<sub>2</sub>H<sub>4</sub>, OH, CO<sub>2</sub>, and H<sub>2</sub>O during the oxidation of *n*-dodecane/O<sub>2</sub>/Argon mixtures at P=2.25 atm,  $\phi=1.0$ . In Fig. 43, the species profiles computed at these conditions, are shown to agree well with the experiments for a major part of the studied time interval. Vasu *et al.* [64] also measured OH time histories during the oxidation of *n*-dodecane/O<sub>2</sub>/Argon mixtures at P=15 atm,  $\phi=0.5$ . In Fig. 44, the computed OH profiles closely follow the measured rise of OH, except at T=1158 K, where the ignition seems to occur earlier than predicted by experiments.

#### Laminar Flame Speed Results

Kumar and Sung [100] measured laminar flame speeds of *n*-dodecane/air mixtures for a range of equivalence ratios, at atmospheric pressure, and unburnt temperature T<sub>u</sub>=400 K and 470 K. Ji *et al.* [101] also measured flame speeds at P=1 atm and T<sub>u</sub>=403 K. Figure 45(a) compares computed flame speeds with the experimental data of Kumar *et al.* and the linearly and non-linearly extrapolated flame speeds of Ji *et al.* The computed results agree with the experiments at T<sub>u</sub>=470 K, and are within the experimental uncertainties at T<sub>u</sub>=403 K for lean fuel/air mixtures. On the rich side, the computed flame speeds are consistently higher than the non-linearly extrapolated data from Ji *et al.*, while still within

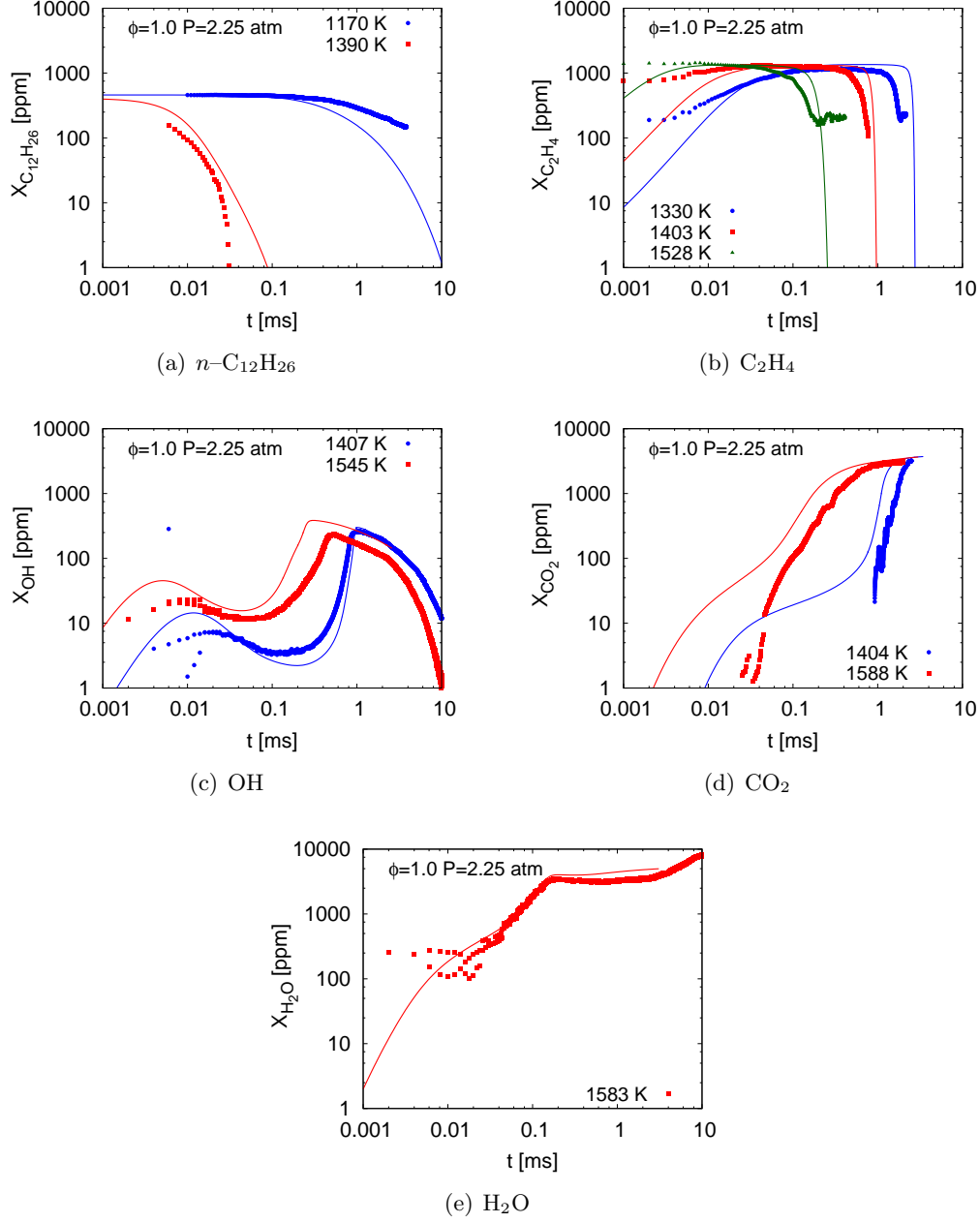


Figure 43: Species profiles during the oxidation of *n*-dodecane/O<sub>2</sub>/argon mixtures in shock tubes as a function of time, at P=2.25 atm,  $\phi=1.0$ ; symbols - experiments: Davidson *et al.* [99]; solid lines - present work.

the uncertainty in the linearly extrapolated flame speeds, and also agreeing closely with the data of Kumar *et al.*

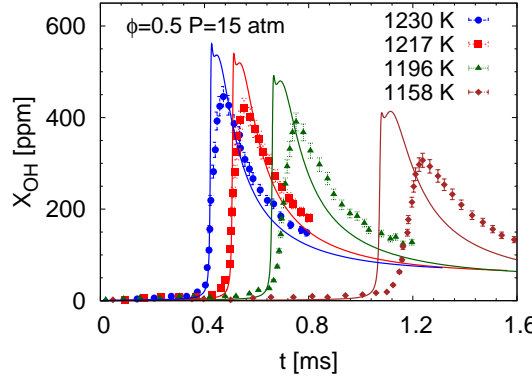


Figure 44: OH concentration profiles during the oxidation of *n*-dodecane/O<sub>2</sub>/Argon in shock tubes as a function of time at P=15 atm,  $\phi=0.5$ ; symbols - experiments: Vasu *et al.* [64]; solid lines - present work.

Ji *et al.* [101] found that the laminar flame speeds of normal alkanes up to *n*-dodecane were similar at P=1 atm, extending a previous such finding for C<sub>4</sub> to C<sub>7</sub> alkanes. Kelley *et al.* [102] measured laminar flame speeds for various *n*-alkanes at higher pressures, and extended the fuel similarity to elevated pressures. To evaluate the performance of the mechanism at different pressures, and unburnt temperatures, we seek to exploit the fuel similarity exhibited by *n*-alkanes.

The laminar flame speeds of *n*-alkanes/air mixtures measured by Kelley *et al.*, at T<sub>u</sub>=353 K, and P=1, 2, 5, and 10 atm, and the *n*-dodecane flame speeds computed using the present mechanism are plotted in Figs. 45(b) and 45(c). The computed results agree closely with the experimental data for all pressures examined. In addition, the agreement between computations and experiments improve with increasing pressure, a welcome trend, since applications include engine-like elevated pressure environments.

The similarity exhibited by the normal alkanes is further explored by considering flame speeds for *n*-heptane, which is part of the base mechanism. At P=1 atm, T<sub>u</sub>=353 K, and  $\phi=1.0$ , the computed flame speeds of *n*-dodecane/air and *n*-heptane/air mixtures are very close, 51.2 cm/s and 51.6 cm/s, respectively. Also, Fig. 46(a) shows very similar temperature profiles for the two fuels as a function of distance along the flame. This is also true of the CO profiles, indicative of similar heat release for the two fuels, consistent with similar flame speeds. The concentrations of C<sub>2</sub> and C<sub>3</sub> species from unimolecular fuel decomposition in Fig. 46(b) show minor differences. However, upon examining the profiles of the key radicals H, O, and OH in Fig. 46(c) for the two fuels, it can be concluded that these profiles are virtually identical, further supporting fuel similarity and consistency within the mechanism.

#### *n*-Dodecane Summary

Using these validation studies, the base chemical mechanism [59, 80] has been extended to include the reaction pathways of *n*-dodecane oxidation. The resulting mechanism has been extensively validated for *n*-dodecane oxidation against various experimental data sets that

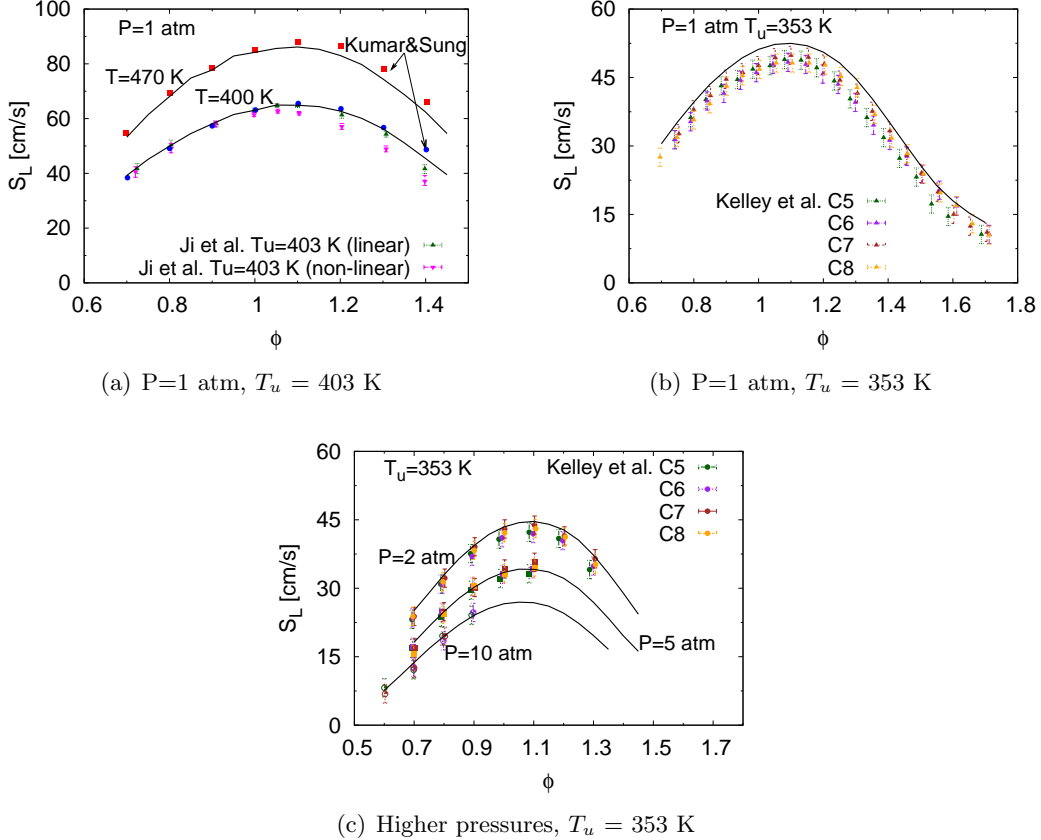


Figure 45: Laminar burning speeds of *n*-dodecane/air mixtures; symbols - experiments: (a) - Kumar & Sung [100], Ji *et al.* [101], (b),(c) - Kelley *et al.* [102]; solid lines - present work.

included ignition delays and species profiles from shock tubes, and laminar burning velocity measurements. The observed similarity in ignition delays and laminar flame speeds among normal alkanes has been invoked to assess the mechanism. Viewed collectively, the ability of the present mechanism to predict different targets has been found to be satisfactory.

### 3.3.3 Extension To Methylcyclohexane

Several detailed chemical mechanisms have been proposed for methylcyclohexane [109, 110, 111]. Of specific interest here is the chemical scheme proposed by Pitz *et al.* [111], combining a low-temperature mechanism with the high temperature mechanism previously developed by Orme *et al.* [110]. This chemical scheme was validated against ignition delay time data from rapid compression machine studies. The Pitz model has been used as the starting detailed mechanism for methylcyclohexane in the present effort, and is reduced to a skeletal level so that the resulting skeletal level mechanism can be combined with the base model. This is the same base model that was extended to include aromatics and *n*-dodecane. The

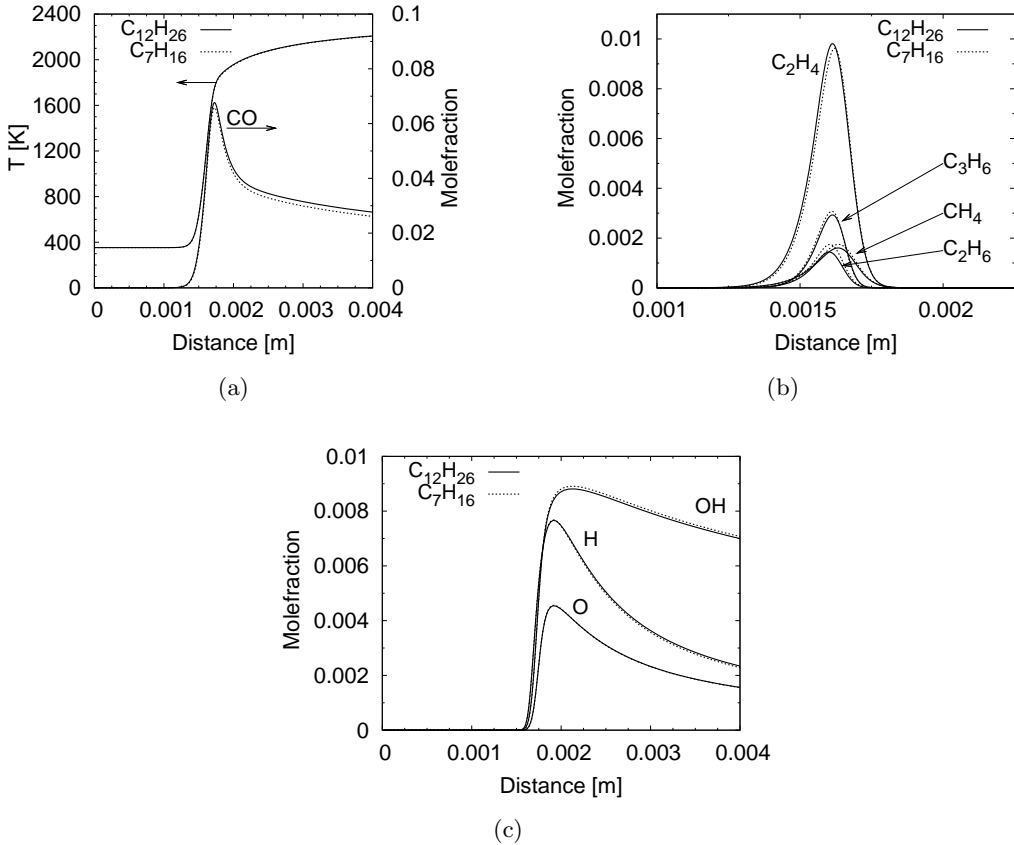


Figure 46: Analysing structures of *n*-dodecane and *n*-heptane premixed flames using the present mechanism, at  $P=1$  atm,  $T_u = 353$  K,  $\phi=1.0$ .

methodology associated with the extension to methycyclohexane is discussed next, followed by a demonstration of the performance of the combined mechanism for different targets.

### Mechanism Development

The reference mechanism for methylcyclohexane oxidation from Pitz *et al.* [111], which will be referred to as the LLNL mechanism, has 8807 forward and reverse reactions and 999 species. This detailed mechanism is first reduced to a skeletal level using a multi-stage reduction strategy put forth by Pepiot-Desjardins and Pitsch, involving species and reaction elimination using the DRGEP approach [60], and chemical species lumping [61]. The database used to carry out the reduction includes plug flow reactor-like configurations, and ignition delays for low to high temperatures (600–1500 K), pressures from 1 to 40 atm, and equivalence ratios from 0.5 to 1.5.

The resulting skeletal mechanism for methylcyclohexane consists of 509 reactions and 187 species. In Fig. 47, ignition delays computed using the detailed and skeletal schemes

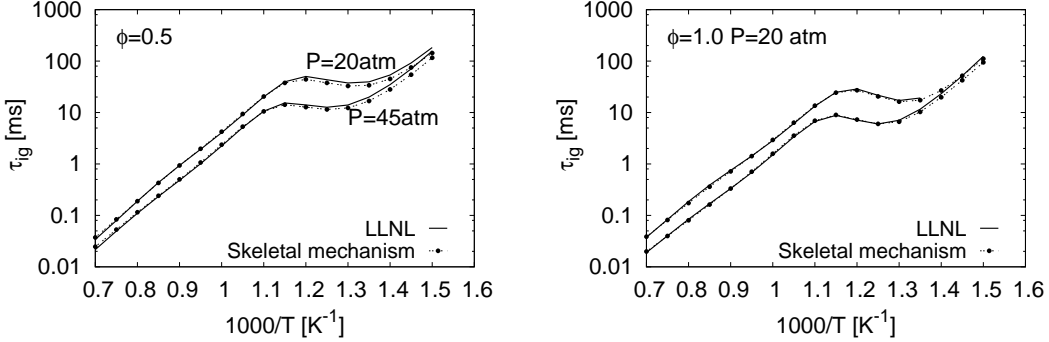


Figure 47: Ignition delay times of methylcyclohexane/air, comparing the skeletal level mechanism with the detailed mechanism results; solid lines - detailed mechanism: Pitz *et al.* [111] (LLNL).

are compared for lean and stoichiometric methylcyclohexane/air mixtures. The comparisons show very good agreement for a variety of temperatures and pressures. A high reduction ratio is achieved here ( $\sim 80\%$ ) and negligible error has been introduced in the skeletal scheme relative to the detailed chemical mechanism.

Combination of the skeletal level methylcyclohexane mechanism and the base mechanism is accomplished in a consistent fashion, along similar lines as that for *n*-dodecane, described in the previous section. The ignition delays computed using the resulting mechanism were found to be too long compared to the experimental data at all temperatures (not shown here). A few changes have been introduced in the combined mechanism to better describe the kinetics of methylcyclohexane oxidation. These changes will now be discussed.

### Validation Tests For Methylcyclohexane

The methylcyclohexane extension is validated using ignition delay measurements in shock tubes and rapid compression machines. These experiments consider a wide range of temperatures, pressures, and fuel/air mixture ratios. Additionally, validation is performed using OH and H<sub>2</sub>O profiles from shock tube measurements, major species measurements in Plug Flow Reactors (PFR), and laminar flame speed measurements at various pressures. The complete list of methylcyclohexane validation tests, which are discussed in further detail below, appears in Table 6.

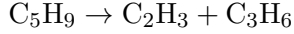
#### *Ignition Delay Results*

Several changes have been introduced in the combined mechanism to better describe the kinetics of methylcyclohexane oxidation, and thus improve the agreement of the present reaction scheme when compared to experimental ignition delay times. The reaction rate changes introduced are summarized here. First, bi-radical pathways were removed from the combined mechanism as suggested by Silke *et al.* [122]. With this change, the ignition delays at all temperatures showed better agreement with the experimental data. The reaction rate

Shock tubes		Plug Flow Reactor	Burning velocity
Ignition delays	Species profiles		
Vanderover <i>et al.</i> [112]			Kumar <i>et al.</i> [118]
Vasu <i>et al.</i> [113]			Singh <i>et al.</i> [119]
Pitz <i>et al.</i> [111]	Vasu <i>et al.</i> [116]	Zeppieri <i>et al.</i> [117]	Ji <i>et al.</i> [120]
Hong <i>et al.</i> [114]	Hong <i>et al.</i> [114]		Kelley <i>et al.</i> [121]
Orme <i>et al.</i> [110]			
Hawthorn <i>et al.</i> [115]			

Table 6: Validation cases for methylcyclohexane undertaken in the present study.

for the decomposition reaction:

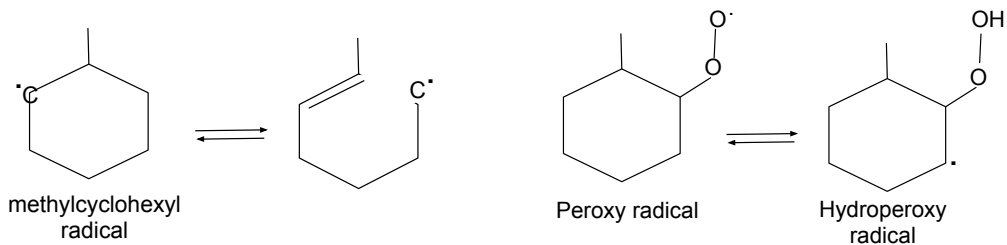


was found to be sensitive for high temperature ignition, and this rate was adopted from Tsang *et al.*, leading to faster ignition at high temperatures.

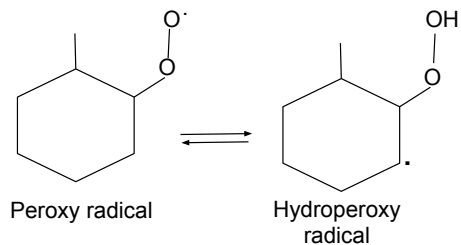
Improvements in NTC region ignition delays were achieved by updating reaction rates for the following key reactions based on recent theoretical studies. The ignition delays in the NTC region were found to be sensitive to (i) ring opening of methylcyclohexyl radicals, for instance as depicted in Fig. 48(a), (ii) reactions involving isomerization of peroxy radicals to hydroperoxy radicals, as in Fig. 48(b), and (iii) reactions for formation of epoxides (cyclic ether) and OH from the hydroperoxy radical as shown in Fig. 48(c). Recent theoretical studies by Sirjean *et al.* have focussed on similar reactions for cyclohexyl radicals [123], cyclohexyl peroxy, and hydroperoxy radicals [124]. In the present chemical model, the reaction rates for the methylcyclohexyl ring opening and closure are adapted from those of cyclohexyl radicals [123]. Similarly, the rate for the formation of epoxide from methylcyclohexyl hydroperoxy radical, and the isomerization of methylcyclohexyl peroxy radical is adapted from that of the cyclohexyl counterparts [124]. The reverse isomerization rate is computed from thermodynamic properties. These rate changes help achieve better agreement with experimental data in the NTC region.

### *Methylcyclohexane/Air Ignition Delays*

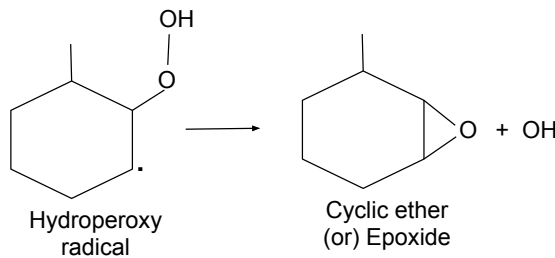
The performance of the mechanism for ignition delays in methylcyclohexane/air mixtures is demonstrated by comparing against experimental ignition delay time data from the shock tube experiments of Vasu *et al.* [113] at  $\phi = 1.0$  and  $P=20$  and  $45$  atm. Comparisons are also performed with the data of Vanderover and Oehlschlaeger [112] at  $\phi = 0.25, 0.5, 1.0$  and  $P=12$  and  $50$  atm. Very good agreement is obtained for ignition delay times between the present scheme and the experimental data in Fig. 49 for low through high temperatures as a result of the changes introduced above. Also shown in these figures are comparisons against ignition delay times measured in a Rapid Compression Machine by Pitz *et al.* [111] at  $\phi = 1.0$ , with  $P$  equal to either  $15$  or  $20$  atm. The present scheme captures the pressure



(a) Ring opening of methylcyclohexyl radical



(b) Peroxy radical isomerization



(c) Hydroperoxy radical forming cyclic ether + OH

Figure 48: Methylcyclohexane reactions that are important in the NTC ignition regime.

dependence of the ignition delays as well the variation with fuel mixture ratios with good accuracy.

#### *Methylcyclohexane/O<sub>2</sub>/Ar Ignition Delays*

Ignition delay time measurements have been made for methylcyclohexane/O<sub>2</sub>/Ar mixtures at near-atmospheric pressures by Hong *et al.* [114] for  $\phi = 0.5$  and  $\phi = 1.0$  mixtures. A comparison of the predicted ignition delay times and the experimental data is shown in Figs. 50(a) and 50(b). The computed ignition delays show good agreement with the experimental data considered in Fig. 50(a), but shorter ignition delays than experiments for  $T < 1200$  K in Fig. 50(b).

Other ignition delay time measurements for methylcyclohexane/O<sub>2</sub>/Ar mixtures at similar pressures come from Vasu *et al.* [113], Orme *et al.* [110], and Hawthorn and Nixon [115].

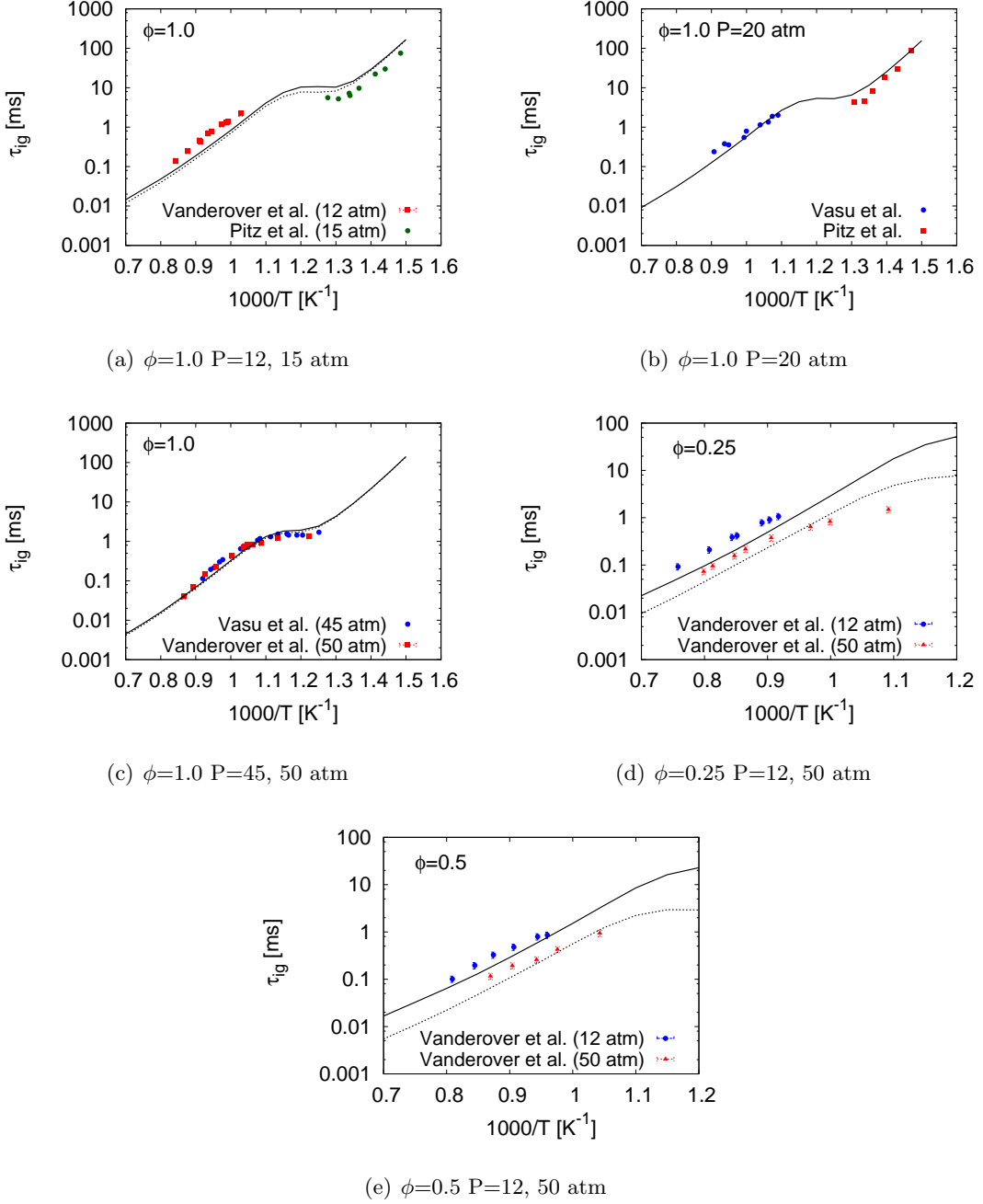


Figure 49: Ignition delay times of methylcyclohexane/air mixtures: Symbols - experimental data from Vanderover and Oehlschlaeger [112], Pitz *et al.* [111], Vasu *et al.* [113]; Solid lines - ignition delays computed using the present reaction scheme.

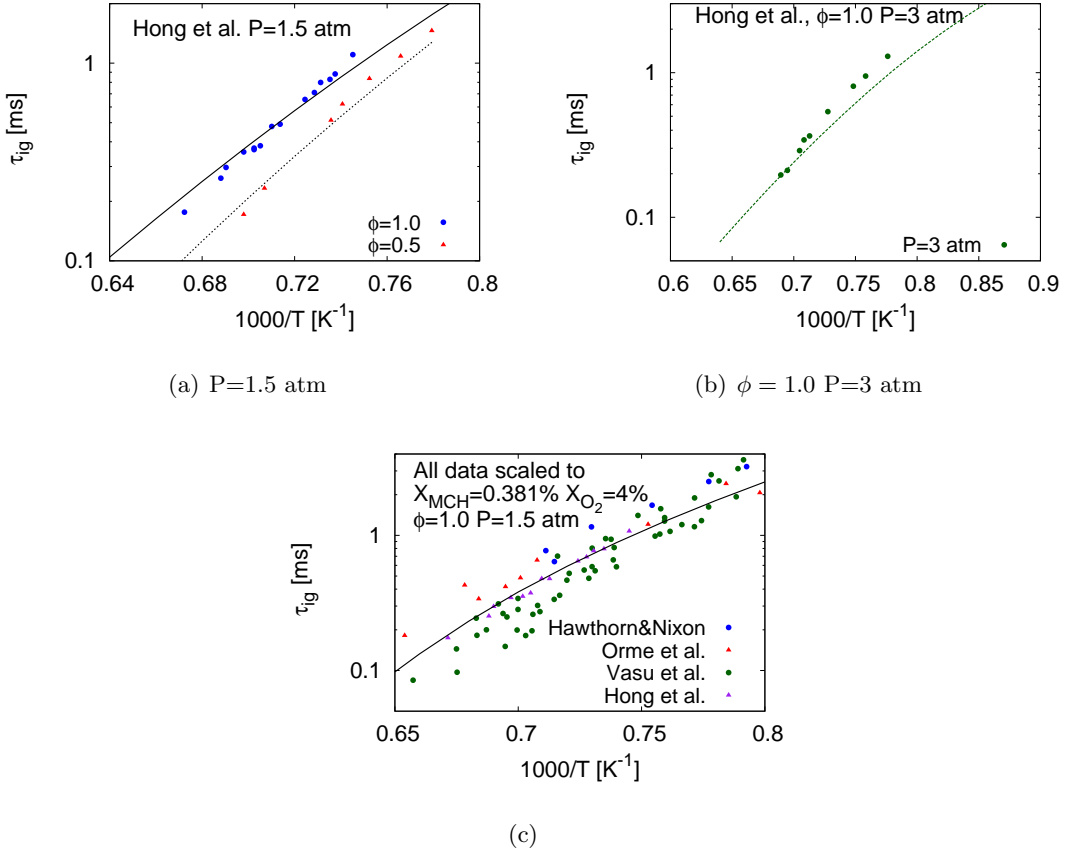


Figure 50: Ignition delay times of methylcyclohexane/O<sub>2</sub>/Ar mixtures: Symbols - experimental data from (a,b,c) Hong *et al.* [114], (c) Vasu *et al.* [113], Orme *et al.* [110], Hawthorn and Nixon [115]; Solid lines - ignition delays computed using the present reaction scheme.

In Fig. 50(c), these data, along with those of Hong *et al.* are scaled to a common fuel concentration  $X_{MCH} = 0.381\%$ ,  $X_{O_2}=2\%$ , balance Ar ( $\phi = 1.0$ ),  $P=1.5$  atm, using the correlation proposed by Vasu *et al.* [113],

$$\tau_{ign} \propto P^{-0.98 \pm 0.13} X_{MCH}^{-0.82 \pm 0.08} \phi^{1.47 \pm 0.09}.$$

The ignition delays computed at these conditions using the present scheme fall within the variability in the scaled experimental data in Fig. 50(c).

#### Results For OH/H<sub>2</sub>O Time-Histories

Vasu *et al.* [116] measured OH profiles during methylcyclohexane/O<sub>2</sub>/Ar oxidation, with  $X_{MCH} = 1000$  ppm,  $X_{O_2} = 0.021$ , balance Ar, at an equivalence ratio of  $\phi = 0.5$  and a pressure of  $P=15$  atm. The OH profiles predicted using the present reaction scheme are compared with the experimentally measured profiles of Vasu *et al.* in Fig. 51. The agreement

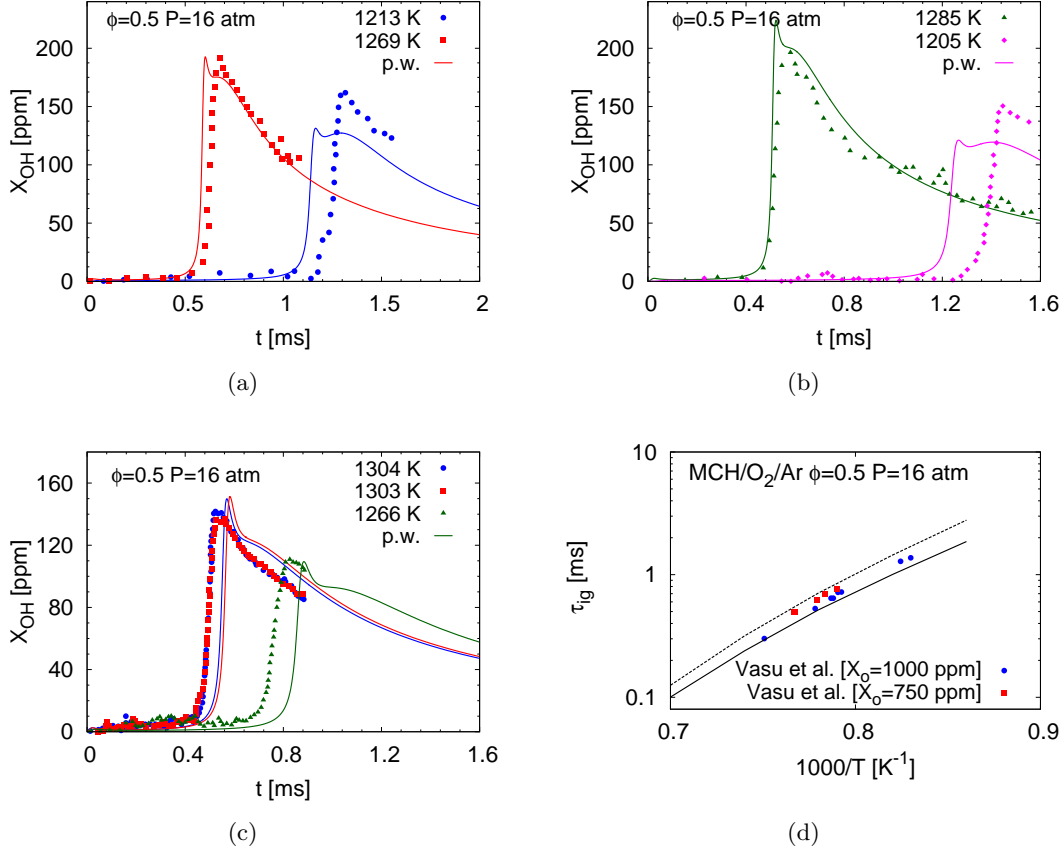


Figure 51: Methylcyclohexane/O<sub>2</sub>/Ar oxidation: (a–c) OH profiles at  $X_{\text{MCH}} = 1000$  ppm,  $X_{\text{O}_2} = 0.021$ , balance Ar, ( $\phi = 0.5$ )  $P=16$  atm (d) Ignition delay times corresponding to (i) the experimental conditions of (a–c), and (ii)  $X_{\text{MCH}} = 750$  ppm,  $\phi = 0.5$ ,  $P=16$  atm; Symbols - experimental data from Vasu *et al.* [116]; Solid lines - results computed using the present reaction scheme.

is satisfactory across the conditions being considered, with the peak OH value and the rise of OH profiles predicted reasonably well. The ignition delays were also measured by Vasu *et al.* at the same conditions at which the OH profiles were obtained, along with another set of ignition delay data at  $X_{\text{MCH}} = 750$  ppm,  $\phi = 0.5$ , and  $P=15$  atm. These data are compared to the ignition delay times computed using the present chemical model in Fig. 51(d), and show good agreement.

Hong *et al.* [114] also measured OH and H<sub>2</sub>O profiles during methylcyclohexane/O<sub>2</sub>/Ar oxidation, at  $\phi \sim 0.85$  and  $P=2.2$  atm in a shock tube facility. The computed species profiles are compared with the experimentally measured profiles of Hong *et al.* in Fig. 52. While the predictions show good agreement with the experimental peak values and rise of OH and H<sub>2</sub>O time-histories, at  $T=1359$  K the predicted rise of profiles occurs earlier than in the experiments. This early rise of the OH/H<sub>2</sub>O profiles was also observed when comparing the

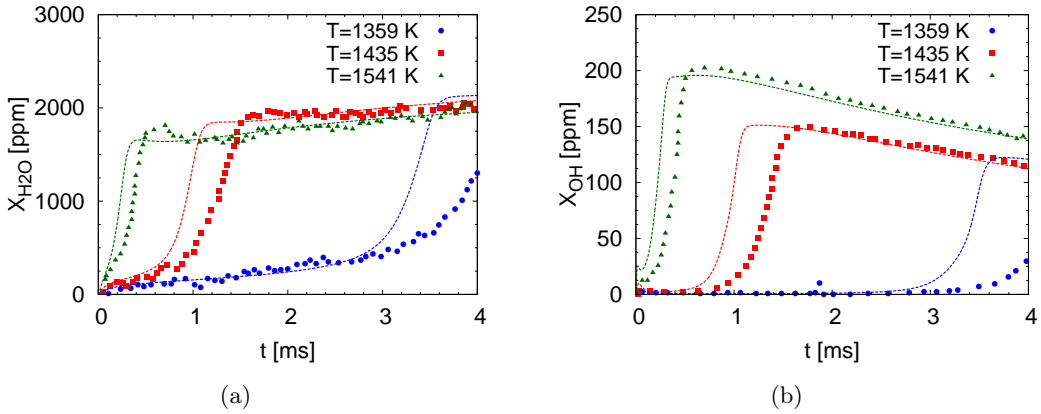


Figure 52: Species time-histories during methylcyclohexane/O<sub>2</sub>/Ar oxidation. Conditions: (1) T = 1359 K, P=2.2 atm, 380 ppm MCH/4200 ppm O<sub>2</sub>/Ar,  $\phi = 0.95$ , (2) T = 1435 K, P=2.2 atm, 340 ppm MCH/4200 ppm O<sub>2</sub>/Ar,  $\phi = 0.85$ , (3) T = 1541 K, P=2.1 atm, 320 ppm MCH/4200 ppm O<sub>2</sub>/Ar,  $\phi = 0.80$ ; Symbols - experimental data from Hong *et al.* [114]; Dashed lines - OH and H<sub>2</sub>O profiles computed using the present reaction scheme.

jetSurF mechanism predictions with these experimental data (Fig. 15 in Hong *et al.* [114]), and this warrants further investigation.

#### Laminar Flame Speed Results

Several experimental studies have measured laminar flame speeds of methylcyclohexane/air mixtures using different measurement techniques. At atmospheric pressure and an unburnt temperature of T<sub>u</sub>=353 K, Ji *et al.* [120] determined flame speeds in a counterflow configuration. Kelley *et al.* [121] measured propagation speeds of spherically expanding methylcyclohexane/air flames at several pressures with T<sub>u</sub>=353 K. Similar techniques were used by Singh *et al.* [119] to measure flame speeds at P=1 atm and T<sub>u</sub>=400 K. Also, Kumar & Sung [118] used a counterflow twin-flame technique to determine flame speeds of methylcyclohexane/air mixtures at these conditions.

The flame speeds computed using the present reaction scheme are compared with these experimental data in Fig. 53. At atmospheric pressure, the flame speeds at T<sub>u</sub>=400 K in Fig. 53(a) agree closely with the data of Singh *et al.*, while at T<sub>u</sub> = 353 K in Fig. 53(b), the computed curves agree closely with the data of Kelley *et al.* The degree of agreement with the Kelley *et al.* data remains consistently good at the higher pressures as well. In all, the ability of the reaction model to predict laminar flame speeds is demonstrated to be good, and within the variability of the experimental flame speed data determined using different measurement techniques.

#### Species Profiles In Plug Flow Reactors

High temperature oxidation of methylcyclohexane/air mixtures was studied by Zeppieri *et*

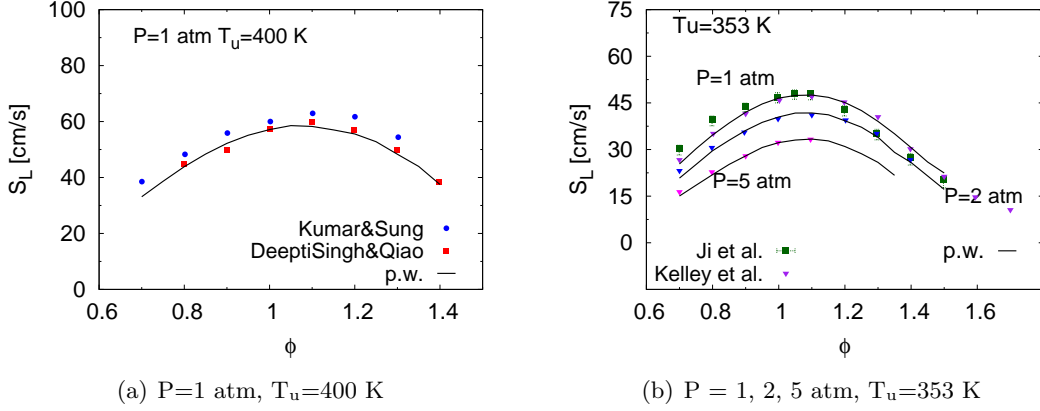


Figure 53: Laminar flame propagation speeds in methylcyclohexane/air mixtures: Symbols - experimental data from Kumar & Sung [118], Deepti Singh & Qiao [119], Ji *et al.* [120], Kelley *et al.* [121]; Solid lines - flame speeds computed using the present reaction scheme.

*al.* [117] in the Princeton Turbulent Flow Reactor. They measured concentrations of methylcyclohexane (MCH), as well as typical major and minor species formed during oxidation. The experimental data was obtained at  $P=1$  atm,  $T = 1160$  K, initial MCH concentration of 1815 ppm, and fuel/air mixture ratio of  $\phi = 1.3$ . The experimental configuration is modeled as a isobaric reactor in the present work.

A comparison between the species concentration time evolution predicted using the present scheme and the experimental data is presented in Fig. 54. The change in temperature as a function of time is accurately represented by the present scheme in Fig. 54(b). The fuel decay is faster than the experiments in Fig. 54(a), which is also consistent with the discrepancies between the predictions in ethene and ethane profiles and the experiments. An improvement in the fuel decay profile is therefore expected to lead to better agreement in  $\text{C}_2\text{H}_4$  and  $\text{C}_2\text{H}_6$  profiles as well. The evolution of  $\text{CO}_2$  has been predicted accurately in Fig. 54(d). However, some discrepancies are seen in  $\text{CO}$ ,  $\text{C}_3\text{H}_6$  and  $\text{CH}_4$  concentrations in Figs. 54(c), 54(g), and 54(h).

#### *Methylcyclohexane Summary*

With the extensive validation tests presented here, it can be concluded that the present methylcyclohexane oxidation model is able to reproduce experimental ignition delay times,  $\text{OH}/\text{H}_2\text{O}$  profiles, major species, and laminar flame speeds with reasonable accuracy.

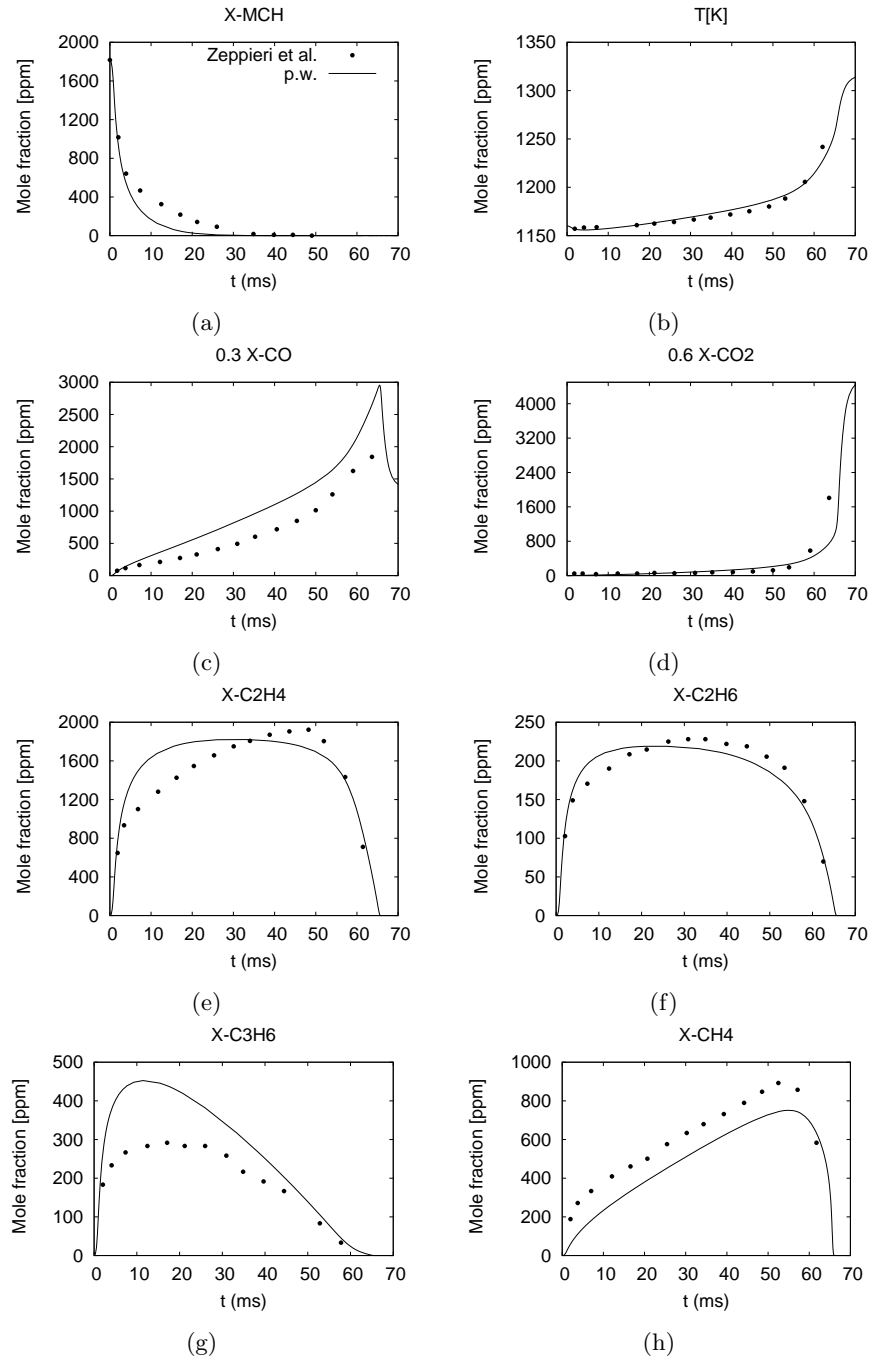


Figure 54: Major species time-evolution during methylcyclohexane/air oxidation in a Plug Flow Reactor at  $P=1$  atm,  $T = 1160$  K,  $X_{\text{MCH}}^0 = 1815$  ppm,  $\phi = 1.3$ : Symbols - experimental data from Zeppieri *et al.* [117]; Solid lines - species profiles computed using the present reaction scheme.

## Re-Validation Of Individual Components In The Surrogate Mechanism

With the addition of the reaction pathways of methylcyclohexane, several aromatics (especially *m*-xylene), and *n*-dodecane to the base model, the combined chemical mechanism can be used to describe the oxidation of the jet fuel surrogate proposed in Table 2. The final step of this process consists of re-validating the different surrogate fuel components now that they have been combined to form the final surrogate mechanism. This re-validation is used to evaluate any non-linear changes that might have occurred because of the added reaction modules. The results for the different test cases for the individual surrogate components were recomputed using this reaction scheme, and little changes were observed from the previous results (not shown here). Most of the differences resulted in improved agreement with the relevant experimental data.

### 3.4 Performance Of The Model Jet Fuel Surrogate

The capabilities of the model JP-8 surrogate proposed in Table 2 are now evaluated. Global kinetic targets such as ignition delay times and laminar flame speeds computed using the present reaction scheme are compared with experimental data for real JP-8 fuels in this section.

#### *Ignition Delay Results*

Figure 55 shows a comparison of ignition delays predicted using the present scheme with experimental measurements from Vasu *et al.* [125]. The experiments were conducted in a shock tube at  $P=20$  atm, using fuel/air mixture ratios of  $\phi = 0.5$  and 1.0. Agreement of the model and the experiments is excellent for both of the equivalence ratios that are considered here.

#### *Laminar Flame Speed Results*

Ji *et al.* [126] measured laminar flame speeds of JP-7 and JP-8 fuels at atmospheric pressure and at an unburnt temperature of  $T_u = 403$  K. The computed flame speeds for the model surrogate are compared with this experimental data in Fig. 56. The flame speed predictions closely follow the JP-8 flame speeds at all fuel/air ratios. It can also be seen that the experimentally determined flame speeds of *n*-dodecane are approximately equal to those of the jet fuels, justifying the use of this component as the significant alkane within the model surrogate.

The ability of the present scheme to predict global oxidation characteristics of real jet fuels, such as ignition delays and laminar flame speeds, can be concluded to be excellent. The chemical model will be further assessed in other configurations of interest in future work.

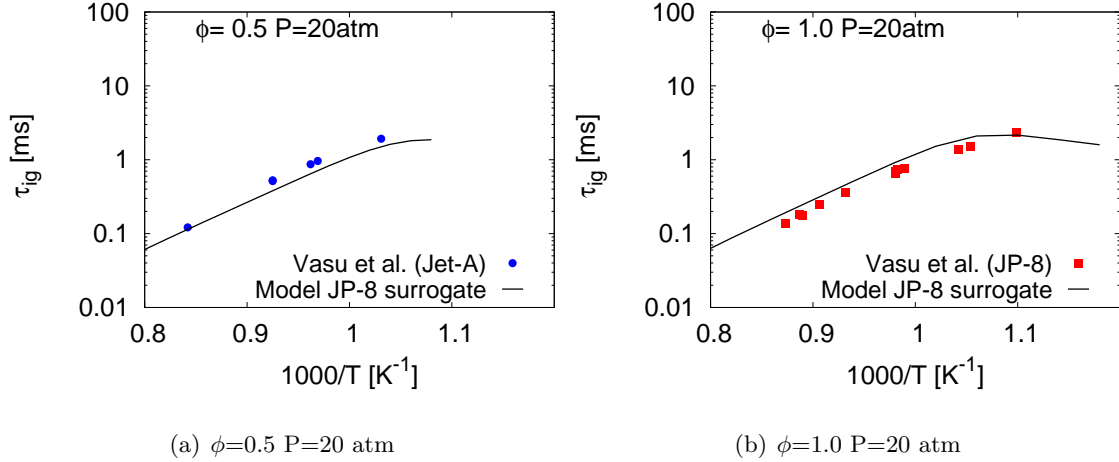


Figure 55: Ignition delay times: Symbols - experimental data from Vasu *et al.* [125]; Solid lines - predictions using the present reaction scheme with the model surrogate proposed in Table 2 as the fuel.

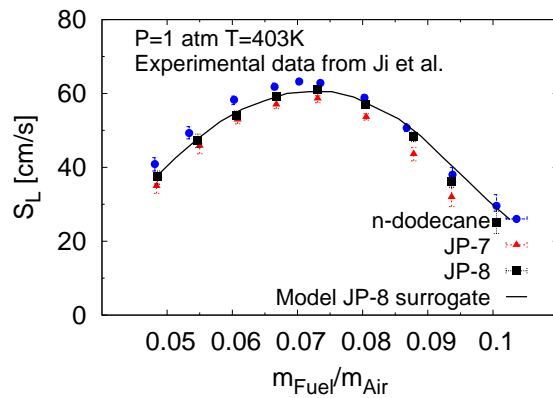


Figure 56: Laminar flame speeds: Symbols - experimental data from Ji *et al.* [126], Solid lines - flame speed predictions using the present reaction scheme with the model surrogate proposed in Table 2 as the fuel.

## 4 Conclusions

This project has addressed physical modeling needs in the areas of both sub-filter LES model development and chemical mechanism formulation and validation. The resulting models are expected to directly influence and improve the next generation of high fidelity reactive flow simulations. Additionally, the two project components naturally interface within a comprehensive flow modeling framework. For example, chemical mechanisms can be specifically tailored for individual modeling studies using the surrogate framework. A highly detailed *n*-dodecane mechanism might be reduced and combined with a particular aromatic mechanism for use in a DNS study of soot that relies on finite rate chemistry. Conversely, the same mechanism might be left in an unreduced form and combined with several aromatic mechanisms for use in an LES based on the flamelet approach. The surrogate framework enables this level of tailoring of the chemistry, so that the modeling approach can be matched to the application.

Progress in the area of sub-filter LES modeling similarly sets the stage for combustion model adaptation. The individual advances in non-premixed and premixed combustion modeling might be applied directly in simulations of engines characterized by a single combustion regime. Conversely, in more complex settings where multiple combustion regimes are expected, the multi-regime flamelet approach can be employed. The advantages of the new single regime developments can then be leveraged where needed, using a chemical mechanism that is tailored to describe either flame extinction or burning velocities.

In future work these newly developed models will continue to be advanced and integrated into Stanford's computational infrastructure. Furthermore, they will be made available to the Air Force Office of Scientific Research upon request. The next step in the process of fully leveraging their potential is to integrate their capabilities in the simulation of complex geometry engines. This is the planned topic of future studies.

## References

- [1] N. Peters. *Turbulent Combustion*. Cambridge Univ. Press, Cambridge, UK, 2000.
- [2] T. Poinsot and D. Veynante. *Theoretical and Numerical Combustion*. R. T. Edwards, Inc., Flourtown, PA, USA, 2001.
- [3] H. Pitsch. Large-eddy simulation of turbulent combustion. *Ann. Rev. Fluid Mech.*, 38:453–483, 2006.
- [4] E. Knudsen and H. Pitsch. Capabilities and limitations of multi-regime flamelet models. *Combust. Flame*, 159(1):242–264, 2012.
- [5] R. S. Barlow, A. N. Karpetis, J. H. Frank, and J.-Y. Chen. Scalar profiles and NO formation in laminar opposed-flow partially premixed methane/air flames. *Combust. Flame*, 127:2102–2118, 2001.
- [6] W. J. Pitz, N. P. Cernansky, F. L. Dryer, F. N. Egolfopoulos, J. T. Farrell, D. G. Friend, and H. Pitsch. Development of an experimental database and chemical kinetic models for surrogate gasoline fuels. *SAE 2007-01-0175*, 2007.
- [7] J. T. Farrell, N. P. Cernansky, F. L. Dryer, D. G. Friend, C. A. Hergart, C. K. Law, R. M. McDavid, C. J. Mueller, A. K. Patel, and H. Pitsch. Development of an experimental database and kinetic models for surrogate diesel fuels. *SAE 2007-01-0201*, 2007.
- [8] M. Colket, T. Edwards, S. Williams, N. P. Cernansky, D. L. Miller, F. Egolfopoulos, P. Lindstedt, K. Seshadri, F. L. Dryer, C. K. Law, D. Friend, D. B. Lenhart, H. Pitsch, A. F. Sarofim, M. Smooke, and W. Tsang. Development of an experimental database and kinetic models for surrogate jet fuels. *AIAA 2007-770*, 2007.
- [9] N. Peters. Laminar diffusion flamelet models in non-premixed turbulent combustion. *Prog. Energy Combust. Sci.*, 10:319–339, 1984.
- [10] C. D. Pierce and P. Moin. Progress-variable approach for large-eddy simulation of non-premixed turbulent combustion. *J. Fluid Mech.*, 504:73–97, 2004.
- [11] M. Ihme, C. M. Cha, and H. Pitsch. Prediction of local extinction and re-ignition effects in non-premixed turbulent combustion using a flamelet / progress variable approach. *Proc. Comb. Inst.*, 30:793–800, 2005.
- [12] H. Pitsch and N. Peters. A consistent flamelet formulation for non-premixed combustion considering differential diffusion effects. *Combust. Flame*, 114:26–40, 1998.
- [13] E. Knudsen and H. Pitsch. A validation study of the flamelet approach’s ability to predict flame structure when fluid mechanics are fully resolved. In *CTR Ann. Research Briefs*. Stanford University, 2009.

- [14] E. Knudsen, S. H. Kim, and H. Pitsch. An analysis of premixed flamelet models for large eddy simulation of turbulent combustion. *Phys. Fluids*, 22(115109):1–24, 2010.
- [15] A. W. Vreman, B. A. Albrecht, J. A. van Oijen, L. P. H. de Goey, and R. J. M. Bastiaans. Premixed and nonpremixed generated manifolds in large-eddy simulation of sandia flame D and F. *Combust. Flame*, 153(3):394–416, 2008.
- [16] H. Pitsch. FlameMaster: A C++ computer program for 0D combustion and 1D laminar flame calculations. Available from <http://www.stanford.edu/~hpitsch/>, 1998.
- [17] V. Moureau, B. Fiorina, and H. Pitsch. A level set formulation for premixed combustion LES considering the turbulent flame structure. *Combust. Flame*, 156(4):801–812, 2009.
- [18] O. Colin, F. Ducros, D. Veynante, and T. Poinsot. A thickened flame model for large eddy simulations of turbulent premixed combustion. *Phys. Fluids*, 12(7):1843–1862, 2000.
- [19] E. Knudsen and H. Pitsch. A general flamelet transformation useful for distinguishing between premixed and non-premixed modes of combustion. *Combust. Flame*, 156(3):678–696, 2009.
- [20] V. Favier and L. Vervisch. Edge flames and partially premixed combustion in diffusion flame quenching. *Combust. Flame*, 125:788–803, 2001.
- [21] G. R. Ruetsch, L. Vervisch, and A. Liñán. Effects of heat release on triple flames. *Phys. Fluids*, 7(6):1447–1454, 2005.
- [22] J. A. van Oijen, R. J. M. Bastiaans, and L. P. H. de Goey. Low-dimensional manifolds in direct numerical simulations of premixed turbulent flames. *Proc. Comb. Inst.*, 31:1377–1384, 2007.
- [23] C. D. Pierce and P. Moin. A dynamic model for subgrid-scale variance and dissipation rate of a conserved scalar. *Phys. Fluids*, 10(12):3041–3044, 1998.
- [24] A. W. Cook and J. J. Riley. A subgrid model for equilibrium chemistry in turbulent flows. *Phys. Fluids*, 6(8):2868–2870, 1994.
- [25] D. Veynante and R. Knikker. Comparison between LES results and experimental data in reacting flows. *J. Turbulence*, 7(35):1–20, 2006.
- [26] G. Balarac, H. Pitsch, and V. Raman. Development of a dynamic model for the subfilter scalar variance using the concept of optimal estimators. *Phys. Fluids*, 20(3):1–9, 2008.
- [27] C. M. Kaul, V. Raman, G. Balarac, and H. Pitsch. Numerical errors in the computation of sub-filter scalar variance in large eddy simulations. *Phys. Fluids*, 21(5):1–11, 2009.

- [28] S. S. Girimaji and Y. Zhou. Analysis and modeling of subgrid scalar mixing using numerical data. *Phys. Fluids*, 8(5):1224–1236, 1996.
- [29] G. Balarac, H. Pitsch, and V. Raman. Modeling of the sublter scalar dissipation rate using the concept of optimal estimators. *Phys. Fluids*, 20(091701):1–4, 2008.
- [30] C. M. Kaul and V. Raman. A posteriori analysis of numerical errors in sublter scalar variance modeling for large eddy simulations. *Phys. Fluids*, 23(035102):1–14, 2011.
- [31] P. Domingo, L. Vervisch, and D. Veynante. Large-eddy simulation of a lifted methane jet flame in a vitiated coflow. *Combust. Flame*, 152(3):415–432, 2008.
- [32] G. R. Newman, B. E. Launder, and J. L. Lumley. Modelling the behaviour of homogeneous scalar turbulence. *J. Fluid Mech.*, 111:217–232, 1981.
- [33] W. P. Jones and P. Musonge. Closure of the Reynolds stress and scalar flux equations. *Phys. Fluids*, 31(12):3589–3604, 1988.
- [34] J. P. H. Sanders and I. Gökalp. Scalar dissipation rate modelling in variable density turbulent axisymmetric jets and diffusion ames. *Phys. Fluids*, 10(4):938–948, 1998.
- [35] C. Wall, B. J. Boersma, and P. Moin. Evaluation of the assumed beta probability density function subgrid-scale model for large eddy simulation of nonpremixed, turbulent combustion with heat release. *Phys. Fluids*, 12(10):2522–2529, 2000.
- [36] C. S. Yoo, R. Sankaran, and J. H. Chen. A DNS study on the stabilization mechanism of a turbulent lifted ethylene jet flame in highly-heated coflow. *Proc. Comb. Inst.*, 33:1619–1627, 2011.
- [37] M. Ihme and Y. C. See. Prediction of autoignition in a lifted methane/air flame using an unsteady flamelet/progress variable model. *Combust. Flame*, 157:1850–1862, 2010.
- [38] H. Pitsch. Unsteady flamelet modeling of differential diffusion in turbulent jet diffusion flames. *Combust. Flame*, 123:358–374, 2000.
- [39] P. Vedula, P. K. Yeung, and R. O. Fox. Dynamics of scalar dissipation in isotropic turbulence: a numerical and modelling study. *J. Fluid Mech.*, 433(35):29–60, 2001.
- [40] C. Meneveau, T. S. Lund, and W. H. Cabot. A Lagrangian dynamic subgrid-scale model of turbulence. *J. Fluid Mech.*, 319:353–385, 1996.
- [41] J. W. Deardorff. Stratocumulus-capped mixed layers derived from a 3-dimensional model. *Boundary-Layer Meteorology*, 18(4):495–527, 1980.
- [42] E. Knudsen, E. S. Richardson, E. M. Doran, H. Pitsch, and J. H. Chen. Modeling scalar dissipation and scalar variance in LES: Algebraic and transport equation closures. *Phys. Fluids*, (Submitted), 2012.

- [43] E. M. Doran. *A multi-dimensional flamelet model for ignition in multi-feed combustion systems*. PhD thesis, Stanford University, 2011.
- [44] E. M. Doran and H. Pitsch. A bivariate beta distribution as a presumed PDF for multiple scalar mixing. *In Press In Phys. Fluids*, 2011.
- [45] C. Rosales and C. Meneveau. Linear forcing in numerical simulations of isotropic turbulence: physical space implementations and convergence properties. *Phys. Fluids*, 17(9):1–8, 2005.
- [46] V. Eswaran and S. B. Pope. Direct numerical simulations of the turbulent mixing of a passive scalar. *Phys. Fluids*, 31(3):506–520, 1988.
- [47] R. Sankaran, E. R. Hawkes, J. H. Chen, T. Lu, and C. K. Law. Structure of a spatially developing turbulent lean methane-air Bunsen flame. *Proc. Comb. Inst.*, 31:1291–1298, 2007.
- [48] J.-H. Chen, A. Choudhary, B. De Supinski, M. DeVries, E. R. Hawkes, S. Klasky, W. K. Liao, K. L. Ma, J. Mellor-Crummey, N. Podhorski, R. Sankaran, S. Shende, and C. S. Yoo. Terascale direct numerical simulations of turbulent combustion using S3D. *Computational Science and Discovery*, 2(015001), 2009.
- [49] H. Pitsch. A consistent level set formulation for large-eddy simulation of premixed turbulent combustion. *Combust. Flame*, 143:587–598, 2005.
- [50] J. A. van Oijen, F. A. Lammers, and L. P. H. de Goey. Modeling of complex premixed burner systems by using flamelet-generated manifolds. *Combust. Flame*, 127(3):2124–2134, 2001.
- [51] O. Gicquel, N. Darabiha, and D. Thévenin. Laminar premixed hydrogen/air counterflow flame simulations using flame prolongation of ILDM with differential diffusion. *Proc. Comb. Inst.*, 28:1901–1907, 2000.
- [52] A. W. Vreman, J. A. van Oijen, L. P. H. de Goey, and R. J. M. Bastiaans. Direct numerical simulation of hydrogen addition in turbulent premixed bunsen flames using flamelet-generated manifold reduction. *Int. J. of Hydrogen Energy*, 34:2778–2788, 2009.
- [53] K.-J. Nogenmyr, P. Petersson, X. S. Bai, A. Nauert, J. Olofsson, C. Brackman, H. Seyfried, J. Zetterberg, Z. S. Li, M. Richter, A. Dreizler, M. Linne, and M. Aldén. Large eddy simulation and experiments of stratified lean premixed methane/air turbulent flames. *Proc. Comb. Inst.*, 31:1467–1475, 2006.
- [54] G. Dixon-Lewis, T. David, P. H. Gaskell, S. Fukutani, H. Jinno, J. A. Miller, R. J. Kee, M. D. Smooke, N. Peters, E. Effelsberg, J. Warnatz, and F. Behrendt. Calculation of the structure and extinction limit of a methane-air counterflow diffusion flame in

the forward stagnation region of a porous cylinder. *Proc. Comb. Inst.*, 20:1893–1904, 1984.

[55] J. A. van Oijen and L. P. H. de Goey. Modelling of premixed counterflow flames using the flamelet-generated manifold method. *Combust. Theory and Modelling*, 6:463–478, 2002.

[56] O. Desjardins, G. Blanquart, G. Balarac, and H. Pitsch. High order conservative finite difference scheme for variable density low Mach number turbulent flows. *J. Comput. Phys.*, 227(15):7125–7159, 2008.

[57] M. Herrmann. A domain decomposition parallelization of the Fast Marching Method. In *CTR Ann. Research Briefs*, pages 213–225. Stanford University, 2003.

[58] B. Thornber, R. W. Bilger, A. R. Masri, and E. R. Hawkes. An algorithm for LES of premixed compressible flows using the Conditional Moment Closure model. *J. Comp. Physics*, 230(20):7687–7705, 2011.

[59] G. Blanquart, P. Pepiot-Desjardins, and H. Pitsch. Assessing uncertainties in numerical simulations of simple reacting flows using the flamemaster code. *Combust. Theory Model.*, 2009.

[60] P. Pepiot-Desjardins and H. Pitsch. An efficient error propagation based reduction method for large chemical kinetic mechanisms. *Combust. Flame*, 154:67–81, 2008.

[61] P. Pepiot-Desjardins and H. Pitsch. An automatic chemical lumping method for the reduction of large chemical kinetic mechanisms. *Combust. Theory. Mod.*, 12 (6):1089–1108, 2008.

[62] H. Pitsch and M. Bollig. Flamemaster, a computer code for homogeneous and one-dimensional laminar flame calculations. *Institut fur Technische Mechanik, RWTH Aachen*, 1993.

[63] T. Edwards and L. Q. Maurice. Surrogate mixtures to represent complex aviation and rocket fuels. *J. Prop. Power*, 17:461–466, 2000.

[64] S. S. Vasu, D. F. Davidson, Z. Hong, V. Vasudevan, and R. K. Hanson. *n*-Dodecane oxidation at high-pressure: Measurements of ignition delay times and OH concentration time-histories. *Proc. Combust. Inst.*, 32 (1):173–180, 2009.

[65] ChevronTexaco Employees and Contractors, Motor Gasoline Technical Review. *Technical Report, Chevron Corporation*, 2004.

[66] J. Bacha, J. Freel, A. Gibbs, L. Gibbs, G. Hemigaus, N. Hogue, D. Lesnini, J. Lind, J. Maybury, and J. Morris. ChevronTexaco Employees and Contractors, Aviation Fuels Technical Review. *Technical Report, Chevron Corporation*, 2005.

[67] J. Bacha, J. Freel, A. Gibbs, L. Gibbs, G. Hemigaus, K. Hoekman, J. Horn, M. Ingham, L. Jossens, D. Kohler, D. Lesnini, J. McGeehan, N. Nikanjam, E. Olsen, R. Organ, B. Scott, M. Sztenderowicz, A. Tiedemann, C. Walker, J. Lind, J. Jones, D. Scott, and J. Mills. ChevronTexaco Employees and Contractors, Diesel Fuels Technical Review. *Technical Report, Chevron Corporation*, 2007.

[68] G. Blanquart, P. Pepiot-Desjardins, and H. Pitsch. Chemical mechanism for high temperature combustion of engine relevant fuels with emphasis on soot precursors. *Combust. Flame*, 156:588–607, 2009.

[69] Northrop Grumman. Northrop Grumman Petroleum Product survey reports, updated annually. <http://pps.ms.northropgrumman.com/>, 2005.

[70] K. Brezinsky. The high-temperature oxidation of aromatic hydrocarbons. *Prog. Energy. Combus. Sci.*, 12:1–24, 1986.

[71] J. L. Emdee, K. Brezinsky, and I. Glassman. A kinetic model for the oxidation of toluene near 1200 K. *J. Phys. Chem.*, 96 (5):2151–2161, 1992.

[72] R. P. Lindstedt and L. Q. Maurice. Detailed kinetic modelling of toluene combustion. *Comb. Sci. and Tech.*, 120:119–167, 1996.

[73] F. Battin-Leclerc, R. Bounaceur, N. Belmekki, and P. A. Glaude. Experimental and modeling study of the oxidation of xylenes. *Int. J. Chem. Kinet.*, 38:284–302, 2006.

[74] S. Gail and P. Dagaut. Experimental kinetic study of the oxidation of p-xylene in a JSR and comprehensive detailed chemical modeling. *Combust. Flame*, 141:281–297, 2005.

[75] S. Gail, P. Dagaut, G. Black, and J. M. Simmie. Kinetics of 1,2-dimethylbenzene oxidation and ignition: Experimental and detailed kinetic modeling. *Comb. Sci. Tech.*, 180:1748–1771, 2008.

[76] S. Gail and P. Dagaut. Oxidation of m-xylene in a JSR: experimental study and detailed chemical kinetic modeling. *Comb. Sci. Technol.*, 179:813–844, 2007.

[77] C. B. Shaddix, K. Brezinsky, and I. Glassman. Oxidation of 1-methylnaphthalene. *Proc. Combust. Inst.*, 24:683–690, 1992.

[78] H. Pitsch. Detailed kinetic reaction mechanism for ignition and oxidation of  $\alpha$ -methyl naphthalene. *Proc. Combust. Inst.*, 26:721–728, 1996.

[79] M. Karim, R. Alain, G. Pengloan, and P. Dagaut. Oxidation of 1-methylnaphthalene at 1–13 atm: experimental study in a JSR and detailed chemical kinetic modeling. *Comb. Sci. Tech.*, 179 (7):1261–1285, 2007.

[80] K. Narayanaswamy, G. Blanquart, and H. Pitsch. A consistent chemical mechanism for the oxidation of substituted aromatic species. *Combust. Flame*, 157 (10):1879–1898, 2010.

[81] M. Frenklach, D.W. Clary, T. Yuan, W.C. Gardiner, and S.E. Stein. Mechanism of soot formation in acetylene-oxygen mixtures. *Combust. Sci. Technol.*, 50:79–115, 1986.

[82] J.L. Emdee, K. Brezinsky, and I. Glassman. High-temperature oxidation mechanisms of *m*- and *p*-xylene. *J. Phys. Chem.*, 95(4):1626–1635, 1991.

[83] M. A. Oehlschlaeger, D. F. Davidson, and R. K. Hanson. High-temperature thermal decomposition of benzyl radicals. *J. Phys. Chem. A.*, 110 (21):6649–6653, 2006.

[84] S. Canneaux, F. Louis, M. Ribaucour, A. E. Bakali, and J.-F. Pauwels. A CASPT2 theoretical study of the kinetics of the 2-, 3-, and 4-methylbenzylperoxy radical isomerization. *J. Phys. Chem. A.*, 113:2995–3005, 2009.

[85] Y. Murakami, T. Oguchi, K. Hashimoto, and Y. Nosaka. Density functional study of the high-temperature oxidation of *o*-, *m*-, and *p*-xylyl radicals. *J. Phys. Chem. A.*, 113 (40):10562–10666, 2009.

[86] S. Gail. Thesis, Orleans, 2003.

[87] Hsi-Ping S. Shen and M. A. Oehlschlaeger. The autoignition of C<sub>8</sub>H<sub>10</sub> aromatics at moderate temperatures and elevated pressures. *Combust. Flame*, 156:1053–1062, 2009.

[88] R.J. Johnston and J.T. Farrell. Laminar burning velocities and markstein lengths of aromatics at elevated temperature and pressure. *Proc. Combust. Inst.*, 30:217–224, 2005.

[89] C. Ji, A. Moheet, Y. L. Wang, M. Colket, H. Wang, and F. N. Egolfopoulos. *An experimental study of premixed *m*-Xylene/Air and *n*-Dodecane/*m*-Xylene/Air flames*. Proceedings of the 6th U.S. National combustion meet, University of Michigan, 2009.

[90] K. D. Dahm, P. S. Virk, R. Bounaceur, F. Battin-Leclerc, P. M. Marquaire, R. Fournet, E. Daniau, and M. Bouchez. Experimental and modelling investigation of the thermal decomposition of *n*-dodecane. *J. Anal. Appl. Pyrolysis*, 71:865–881, 2004.

[91] O. Herbinet, P. Marquaire, F. Battin-Leclerc, and R. Fournet. Thermal decomposition of *n*-dodecane: Experiments and kinetic modeling. *J. Anal. Appl. Pyrolysis*, 78:419–429, 2007.

[92] E. Ranzi, A. Frassoldati, S. Granata, and T. Faravelli. Wide-range kinetic modeling study of the pyrolysis, partial oxidation and combustion of heavy *n*-alkanes. *Int. Eng. Chem. Res.*, 44:5170–5183, 2005.

[93] X. You, F. N. Egolfopoulos, and H. Wang. Detailed and simplified kinetic models of *n*-dodecane oxidation: The role of fuel cracking in aliphatic hydrocarbon combustion. *Proc. Combust. Inst.*, 32 (1):403–410, 2009.

[94] H. Wang, E. Dames, B. Sirjean, D. A. Sheen, R. Tangko, A. Violi, J. Y. W. Lai, F. N. Egolfopoulos, D. F. Davidson, R. K. Hanson, C. T. Bowman, C. K. Law, W. Tsang, N. P. Cernansky, D. L. Miller, and R. P. Lindstedt. A high-temperature chemical kinetic model of *n*-alkane (up to *n*-dodecane), cyclohexane, and methyl-, ethyl-, *n*-propyl and *n*-butyl-cyclohexane oxidation at high temperatures, JetSurF version 2.0, (<http://melchior.usc.edu/jetsurf/jetsurf2.0>). September 19, 2010.

[95] C. K. Westbrook, W. J. Pitz, O. Herbinet, H. J. Curran, and E. J. Silke. A detailed chemical kinetic reaction mechanism for *n*-alkane hydrocarbons from *n*-octane to *n*-hexadecane. *Combust. Flame*, 156 (1):181–199, 2009.

[96] P. Pepiot-Desjardins. *PhD. thesis, Department of Mechanical Engineering, Stanford University*. 2008.

[97] D. F. Davidson, D. R. Haylett, and R. K. Hanson. Development of an aerosol shock tube for kinetic studies of low-vapor-pressure fuels. *Combust. Flame*, 155 (1-2):108–117, 2008.

[98] H. S. Shen, J. Steinberg, J. Vanderover, and M. A. Oehlschlaeger. A shock tube study of the ignition of *n*-heptane, *n*-decane, *n*-dodecane, and *n*-tetradecane at elevated pressures. *Energy Fuels*, 23 (5):2482–2489, 2009.

[99] D. F. Davidson, Z. Hong, G. L. Pilla, A. Farooq, R. D. Cook, and R. K. Hanson. Multi-species time history measurements during *n*-dodecane oxidation behind reflected shock waves. *Proc. Combust. Inst.*, 33:151–157, 2011.

[100] K. Kumar and C.-J. Sung. Laminar flame speeds and extinction limits of preheated *n*-decane/O<sub>2</sub>/N<sub>2</sub> and *n*-dodecane/O<sub>2</sub>/N<sub>2</sub> mixtures. *Combust. Flame*, 151 (1):209–224, 2007.

[101] C. Ji, E. Dames, Y. L. Wang, H. Wang, and F. N. Egolfopoulos. Propagation and extinction of premixed C<sub>5</sub> to C<sub>12</sub> *n*-alkane flames. *Combust. Flame*, 157:277–287, 2010.

[102] A. P. Kelley, A. J. Smallbone, D. L. Zhu, and C. K. Law. Laminar flame speeds of C<sub>5</sub> to C<sub>8</sub> *n*-alkanes at elevated pressures: Experimental determination, fuel similarity, and stretch sensitivity. *Proc. Combust. Inst.*, 33:963–970, 2011.

[103] H.-H. Carstensen, A. M. Dean, and O. Deutschmann. Rate constants for the H abstraction from alkanes (RH) by radicals: A systematic study on the impact of R and R'. *Proc. Combust. Inst.*, 31 (1):149–157, 2007.

[104] J. Aguilera-Iparraguirre, H. J. Curran, W. Klopper, and J. M. Simmie. Accurate benchmark calculation of the reaction barrier height for hydrogen abstraction by the hydroperoxyl radical from methane. Implications for  $C_nH_{2n+2}$  where  $n=2$  to 4. *J. Phys. Chem. A*, 112 (30):7047–7054, 2008.

[105] H. K. Ciezki and G. Adomeit. Shock-tube investigation of self-ignition of *n*-heptane-air mixtures under engine relevant conditions. *Combust. Flame*, 93 (4):421–433, 1993.

[106] D. C. Horning, D. F. Davidson, and R. K. Hanson. Study of the high temperature autoignition of *n*-alkane/ $O_2$ /Ar mixtures. *J. Prop. Power*, 18 (2):363–371, 2002.

[107] A. Burcat, R. F. Farmer, and R. A. Matula. Shock initiated ignition in heptane/ $O_2$ /argon mixtures. *Proc. 13<sup>th</sup> Int. Symp. on Shocks and Waves*, pages 826–833, 1981.

[108] M. B. Colket and L. J. Spadaccini. Scramjets fuels autoignition study. *J. Prop. Power*, 17:315–323, 2001.

[109] S. Granata, T. Faravelli, and E. Ranzi. A wide range kinetic modeling study of the pyrolysis and combustion of naphthenes. *Combust. Flame.*, 132(3):533–544, 2003.

[110] J. P. Orme, H. J. Curran, and J. M. Simmie. Experimental and modeling study of methyl cyclohexane pyrolysis and oxidation. *J. Phys. Chem. A.*, 110:114–131, 2006.

[111] W. J. Pitz, C. V. Naik, T. N. Mhaolduin, C. K. Westbrook, H. J. Curran, J. P. Orme, and J. M. Simmie. Modeling and experimental investigation of methylcyclohexane ignition in a rapid compression machine. *Proc. Combust. Inst.*, 31 (1):267–275, 2007.

[112] J. Vanderover and M. A. Oehlschlaeger. Ignition time measurements for methylcyclohexane-and ethylcyclohexane-air mixtures at elevated pressures. *Int. J. Chem. Kinet.*, 41(2):82–91, 2009.

[113] S. S. Vasu, D. F. Davidson, Z. Hong, V. Vasudevan, and R. K. Hanson. Shock tube study of methylcyclohexane ignition over a wide range of pressure and temperature. *Energy & Fuels*, 23:175–185, 2009.

[114] Z. Hong, K. Y. Lam, D. F. Davidson, and R. K. Hanson. A comparative study of the oxidation characteristics of cyclohexane, methylcyclohexane, and *n*-butylcyclohexane at high temperatures. *Combust. Flame.*, 2011.

[115] R. D. Hawthorn and A. C. Nixon. *AIAA J.*, 4:513–520, 1966.

[116] S. S. Vasu, D. F. Davidson, and R. K. Hanson. OH time-histories during oxidation of *n*-Heptane and Methylcyclohexane at high pressures and temperatures. *Combust. Flame*, 156:736–749, 2009.

[117] S. Zeppieri, K. Brezinsky, and I. Glassman. Pyrolysis studies of Methylcyclohexane and Oxidation studies of Methylcyclohexane and Methylcyclohexane/Toluene blends. *Combust. Flame*, 108:266–286, 2009.

[118] K. Kumar and C.J. Sung. Flame propagation and extinction characteristics of neat surrogate fuel components. *Energy & Fuels*, 24(7):3840–3849, 2010.

[119] D. Singh, T. Nishie, and L. Qiao. Laminar flame speeds and markstein lengths of *n*-Decane/Air, *n*-Decane/O<sub>2</sub>/He and MCH/Air flames. *Central States Technical Meeting*, 2010.

[120] C. Ji, E. Dames, B. Sirjean, H. Wang, and F. N. Egolfopoulos. An experimental and modeling study of the propagation of cyclohexane and mono-alkylated cyclohexane flames. *Proc. Combust. Inst.*, 33:971–978, 2011.

[121] F. Wu, A. P. Kelley, and C. K. Law. Laminar flame speeds of cyclohexane and mono-alkylated cyclohexanes at elevated pressures. *Combust. Flame.*, 2011.

[122] E. J. Silke, W. J. Pitz, C. K. Westbrook, and M. Ribaucour. Detailed chemical kinetic modeling of cyclohexane oxidation. *J. Phys. Chem. A.*, 111(19):3761–3775, 2007.

[123] B. Sirjean, P. A. Glaude, M. F. Ruiz-Lopez, and R. Fournet. Theoretical kinetic study of thermal unimolecular decomposition of cyclic alkyl radicals. *J. Phys. Chem. A.*, 112(46):11598–11610, 2008.

[124] B. Sirjean, P. A. Glaude, M. F. Ruiz-Lopez, and R. Fournet. Theoretical kinetic study of the reactions of cycloalkylperoxy radicals. *J. Phys. Chem. A.*, 113(25):6924–6935, 2009.

[125] S. S. Vasu, D. F. Davidson, and R. K. Hanson. Jet fuel ignition delay times: Shock tube experiments over wide conditions and surrogate model predictions. *Combust. Flame*, 152:125–143, 2008.

[126] C. Ji, X. You, A. T. Holley, Y. L. Wang, F. N. Egolfopoulos, and H. Wang. Propagation and extinction of mixtures of air with *n*-dodecane, JP-7, and JP-8 jet fuels. AIAA 2008-974. *46th AIAA Aerospace Sciences Meeting and Exhibit, Reno, Nevada*, 7(10), 2008.